Efficient and Stable Halide Perovskite Device

by

Seongha Lee

B. S in Mechanical and Automotive Engineering, Keimyung University, 2015

M.S in Mechanical Engineering and Material Science, University of Pittsburgh, 2017

Submitted to the Graduate Faculty of the

Swanson School of Engineering in partial fulfillment

of the requirements for the degree of

Doctor of Philosophy

University of Pittsburgh

2021

UNIVERSITY OF PITTSBURGH

SWANSON SCHOOL OF ENGINEERING

This dissertation was presented

by

Seongha Lee

It was defended on

October 28, 2021

and approved by

Sangyeop Lee, PhD, Associate Professor, Mechanical Engineering and Material Science

Katherine Hornbostel, PhD, Assistant Professor, Mechanical Engineering and Material Science

Feng Xiong, PhD, Assistant Professor, Electrical and Computer Engineering

Jung-Kun Lee: Professor, Mechanical Engineering and Material Science

Copyright © by Seongha Lee

2021

Efficient and Stable Halide Perovskite Device

Seongha Lee, PhD

University of Pittsburgh, 2021

Photovoltaics (PVs), which convert absorbed solar energy into electricity, is one of the promising energy devices. They can reduce carbon footprint, providing sustainable energy resources to society. Recently, organo-lead-halide perovskite, $APbX_3$ (A= $CH_3NH_3^+$, $CH_2(NH_2)_2^+$, X=I^-, Cl^-, Br^-) has attracted a huge amount of interest due to its excellent light absorption and carrier transport behavior. These unique properties provide new promises for the perovskite solar cells (PSCs) and resistive random-access memory (ReRAM) which is a key device in the area of renewable energy and neuromorphic computing, respectively. However, this material has a few obstacles such as large I-V hysteresis, interface carrier trapping, and long-term instabilities over humidity and UV light. This study addresses these fundamental problems through comprehensive research on the inorganic carrier transport layer and the passivation coating.

First, NiO is chosen as a hole transport layer to reduce a hysteresis problem of PSCs. Experimental and simulation results show that the reduction in the residual stress improves the electrical quality of the oxidized Ni film and improves the hole transport.

Second, the effect of the $CH_3NH_3PbI_3$-TiO_2 interface on the carrier transport and bipolar switching is studied. While the realignment of defects in the perovskite layer results in an undesired hysteresis issue in PSCs, this behavior can help to design the ReRAM device. The interface controls the conductive chain formation and causes the asymmetric bipolar resistive switching.

Third, polymer-oxide nanoparticle composites are studied to elongate the lifetime of the perovskite layer. Interpenetrating polymer networks (IPNs) exhibit better passivation behavior than individual polymer. In addition, the addition of oxide nanoparticles to the IPNs changes the surface wettability and makes a twisted path for permeating water molecules. As a result, the encapsulation dramatically suppresses the degradation process in a standardized damp heat aging condition (85/85 ℃/RH condition).

Last, the phosphors embedded anti-reflective coating (ARC) layer is explored to improve the stability of PSCs under UV light. This new ARC layer converts UV light to visible light, resulting in the better UV resistance and higher photocurrent generation rate of the PSCs.

Table of Contents

List of Tables

List of Figures

Acknowledgement

It is a pleasure to express my deep sense of thanks and gratitude to many people who support and help me to complete my study.

I profusely thank to my advisor, Prof. Jung-Kun Lee, who inspired and encouraged me with his passion, patience, and support throughout my study and research. He provided critical advice and suggested many importance additions and improvements. It has been an enriching experience to me to study under his authoritative guidance.

I would greatly and truly thank my committee members: Dr. Sangyeop Lee, Dr. Katherine Hornbostel, and Dr. Feng Xiong for their time to make this thesis successful completion. Their thoughtful comments and reviews on my dissertation always helped and guided me to improve my thesis.

I have my thanks to my lab colleagues: Dr. Gill-Sang Han, Dr. Hyun-Woo Shim, Dr. Hee-Suk Roh, Dr. Matthew Duff, Dr. Qin Fen, Yulin Liu, Sumin Bae, Anqi Wang, and Marc Migliozzi who are intelligent, diligent, and very friendly. With their nice help and sharing priceless experience on experiments, I could conduct my research in a productive laboratory environment.

Finally, it is my privilege to thank my wife, Kahee who endured this journey with me, for her constant encouragement and endless support. Without her unwavering belief in me, I could not have completed my thesis. I am forever thankful for the unconditional love and strength you gave me. My child, Jia who is my sunshine, has continuously provided the motivation and pleasure for me. I would especially like to thank my parents and my brother who have made

countless sacrifices to help me to finish my degree with expediency and settle down in this country.

1.0 Introduction

1.1 Research Background

1.1.1 Solar Energy

One of the most important global issues is supply of sustainable energy because of increased energy consumption on the earth. A greater portion of today's energy demand over 85% is fulfilled by fossil fuels but this resource addresses consequent severe impacts on climate changes and pollutions by producing exhaust gases such as CO_2, NOx, and SO_2. In addition, energy demand in the world is expected to increase 2 times by 2050. Although current reserves of fossil fuels can provide for several hundred years, there are still concerns about running out of fossil fuels and the large contribution of greenhouse gas emissions. An additional energy resources, which are clean, are required to provide satisfied energy consumption and security in the world.

Nuclear energy has been gained attention due to the carbon-free electricity and levelized costs of electricity generation. However, nuclear power plant has negative effects on the environment by producing final waste disposal and radioactive particles, which are dangerous to human health for thousands of years. Moreover, nuclear power presents unique threat to the public security because it is powered by nuclear energy. Despite generating massive amounts of carbon-free electricity, unclear power energy has complex safety and security features. Thus, a lot of researchers and scientists have paid attention to renewable energy resources such as solar, wind, geothermal, hydro, biomass, etc.

These renewable or sustainable resources, which are cost effective and abundant in nature are fairly distributed over the world, have the highest potential to be satisfied with energy consumption in a safe manner. They can also eliminate the environmental issue associated with the use of fossil fuels such as carbon emission. Among the renewable and finite energy resources, solar energy has the largest supply capacity to meet the world's primary energy demand as shown in Figure 1. The year supply of solar energy is 25 times larger than the total planetary reserves of coal and 1400 times larger than the current planetary energy consumption.

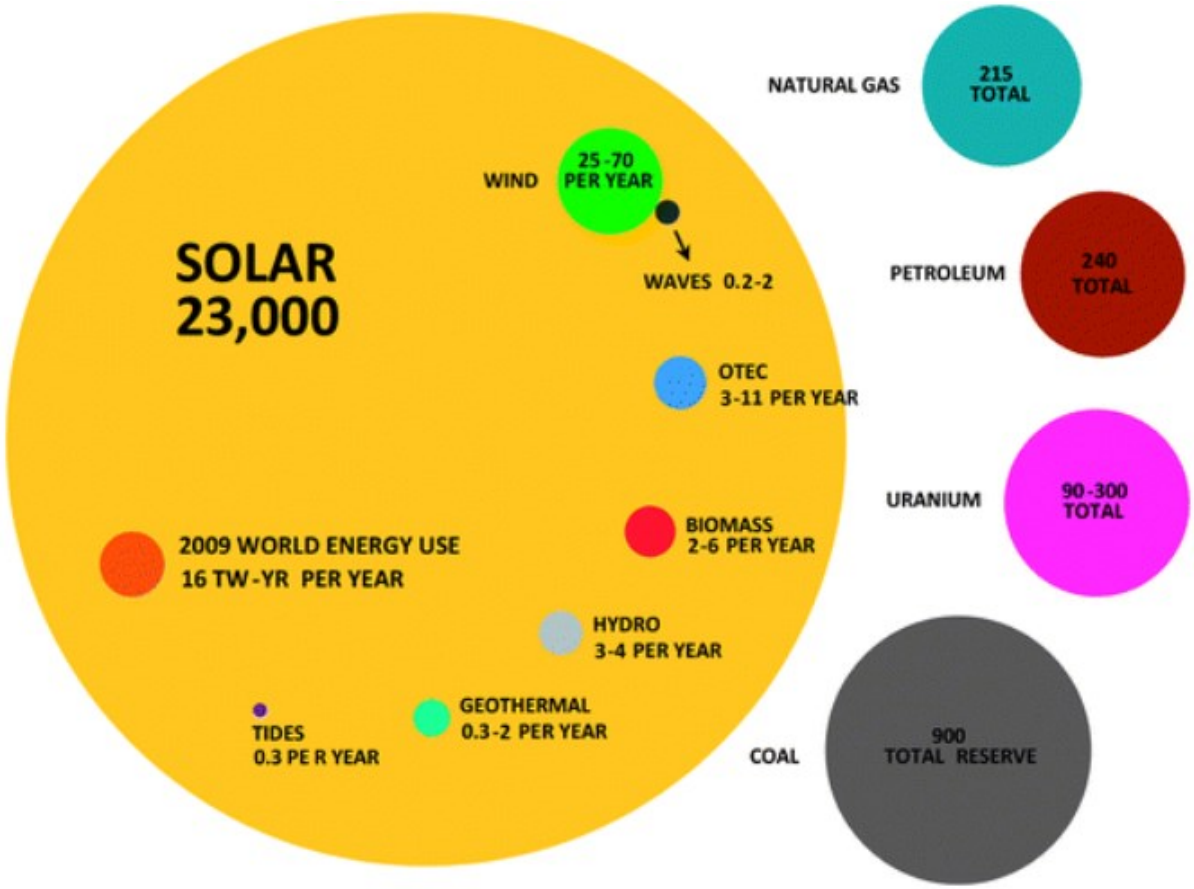

Figure 1 Comparison of finite and renewable planetary energy reserves (Terawatt-years). Total recoverable reserves are shown for the finite resources. Yearly potential is shown for the renewables[1]

Since the sun has provided with plenty of energy, several techniques have been utilized to convert solar radiation into useful heat and electricity such as photovoltaic, solar heating, and solar thermal energy. Global power generation by using solar energy is expected to increase because global average cost of generated electricity by solar energy has been continuously declined by improving the conversion technique.[2] Solar thermal system uses the concentrated solar energy to make steam, which turns a turbine to generate electricity. On the other hand, the photovoltaics (PVs) can be used as electrical devices that directly convert the sun's light to another form of usable energy, electricity. For this reason, the PV system is the object of steadily growing interest in both academic and industrial areas nowadays due to its simplicity.

1.1.2 Photovoltaic (PV)

PV solar cell is composed of semiconductor material such as crystal and amorphous silicon, gallium arsenide, cadmium telluride, etc. that can directly convert sun energy into electricity. Semiconductor has two functions in solar cell, which are light absorption and charge transport. When the photon energy is absorbed in a semiconductor material, free charge carriers, which are electrons in conduction band (CB) and holes in valence band (VB), are created as shown in Figure 2(a). This extra energy allows the excited electrons and holes to flow through an external circuit from a solar cell as an electrical current. This current is extracted by conductive metal contacts on the solar cell and can then be used to power in Figure 2(b).

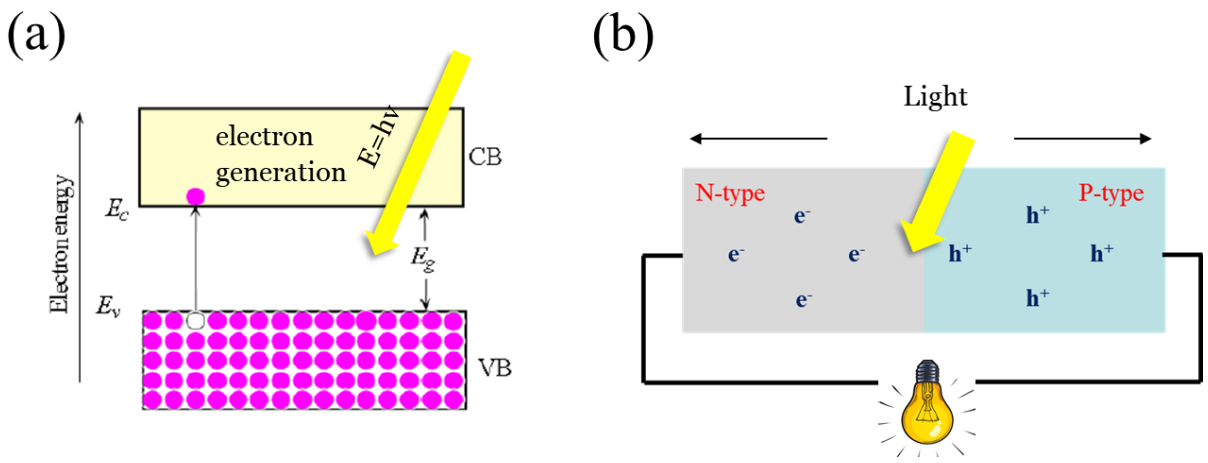

Figure 2 (a) Schematic of the creation of electrons and holes in semiconductor material by photon energy and (b) flow of excited free charge carriers in a colar cell[3]

An important criterion of material selection for the PV solar cells is the bandgap (Eg), which is defined by the energy difference between CB and VB in an intrinsic semiconductor material. Figure 3 shows the maximum theoretical efficiency as a function of bandgap of semiconductor materials. This that can be obtained from a single junction solar cell was calculated by Shockely and Queisser (SQ). In the calculation, radiative recombination in the solar cell is only considered as a loss mechanism.

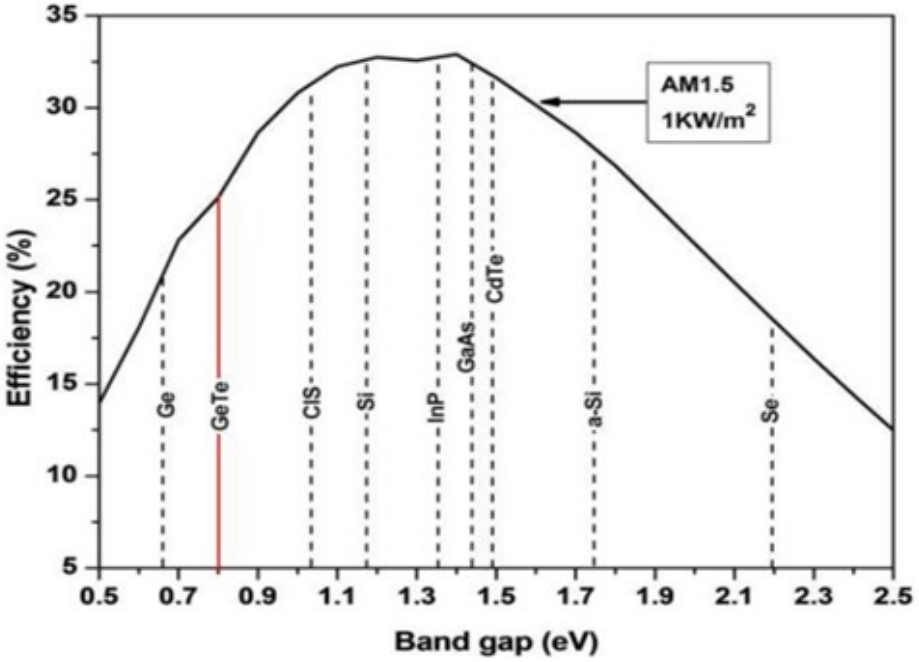

Figure 3 Maximum efficiency vs bandgap for single junction solar cell[3]

When the bandgap is higher than 1.5 eV, most of the energy loss originates from less light absorption. On the other hand, lower bandgap than 1.1 eV has the relaxation process. Both effects for the PV solar cells can decrease the power conversion efficiency (PCE) of the PV solar cells. Another important requirement for the PV solar cell is long carrier diffusion length. A schematic of the p-n junction-type semiconductor solar cells as shown in Figure 4. Charge carrier diffusion length should be larger than light absorption length. If the photogenerated electrons and holes are produced with low diffusion length in the junction, they are mainly recombined, and their energy is dissipated as heat. The PCE of the PV solar cell will be dramatically decreased. Based on optimal bandgap, silicon and GaAs has high potential for PV solar cell, but GaAs is more expansive than silicon. Thus, most common semiconductor material for the PV solar cell is silicon, representing approximately 95% of the modules sold today with efficient and longer lasting than non-silicon based solar cells.

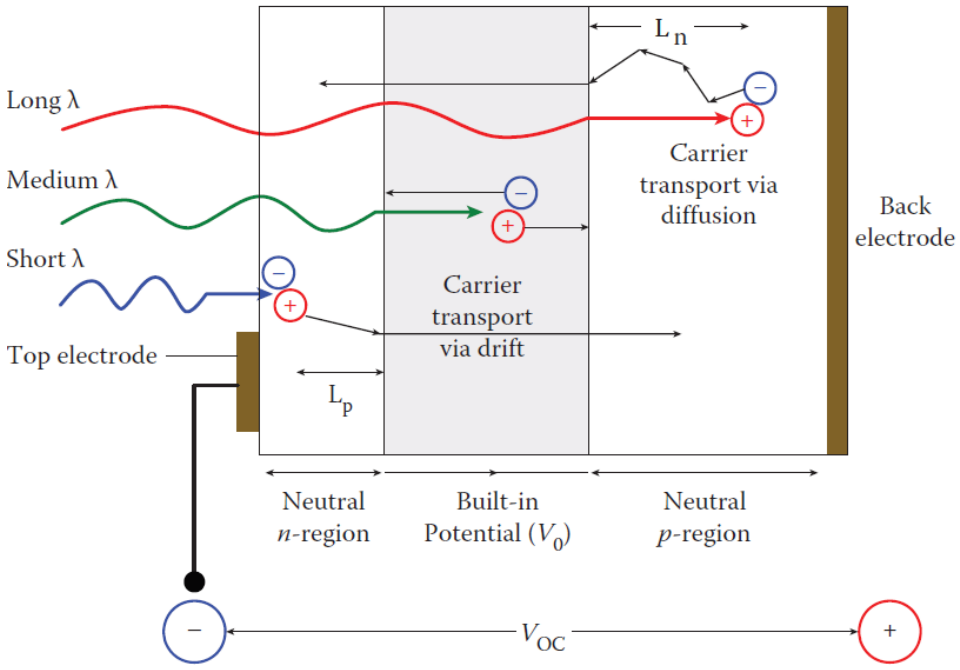

Figure 4 Operating principle of p-n junction-type semiconductor solar cells[4]

There are three types of solar cells which are divided from solar technology. The first generation is the traditional solar cell, which are made from silicon. Since silicon based solar cells have wide bandgap and outstanding optical properties, they have the highest reported single solar cell efficiencies with a good long-term stability. Due to the high cost of silicon solar cell fabrication, the second-generation solar cells, which are usually called thin-film solar cells, were introduced. Copper indium gallium selenide (CIGS) and cadmium telluride (CdTe) are representative thin film solar cells. These solar cells based thin film utilize less materials than the first-generation solar cells, resulting in lower cost of mass production. However, they have lower efficiency and environmental issues due to toxic materials. The third generation is the solar cells, which made from variety of new materials such as polymer solar cells, dye-sensitized solar cells (DSCs), and perovskite solar cells (PSCs). Recently, emerging solar cells, which are the third-generation solar cells, have been rapidly developed due to low-cost production and simple

fabrication. Among them, organometal halide perovskite solar cells (PSCs) have attracted intensive attention as alternate candidates to energy devices due to the fast improvement in power conversion efficiency (PCE). Over the past years, the certified PCE has achieved up from 3.8% to 25.2%, which is higher than that of the other emerging solar cells as shown in Figure 5. Since the perovskite based solar cell can achieve high efficiency and low production costs, the PSCs have become commercially attractive.

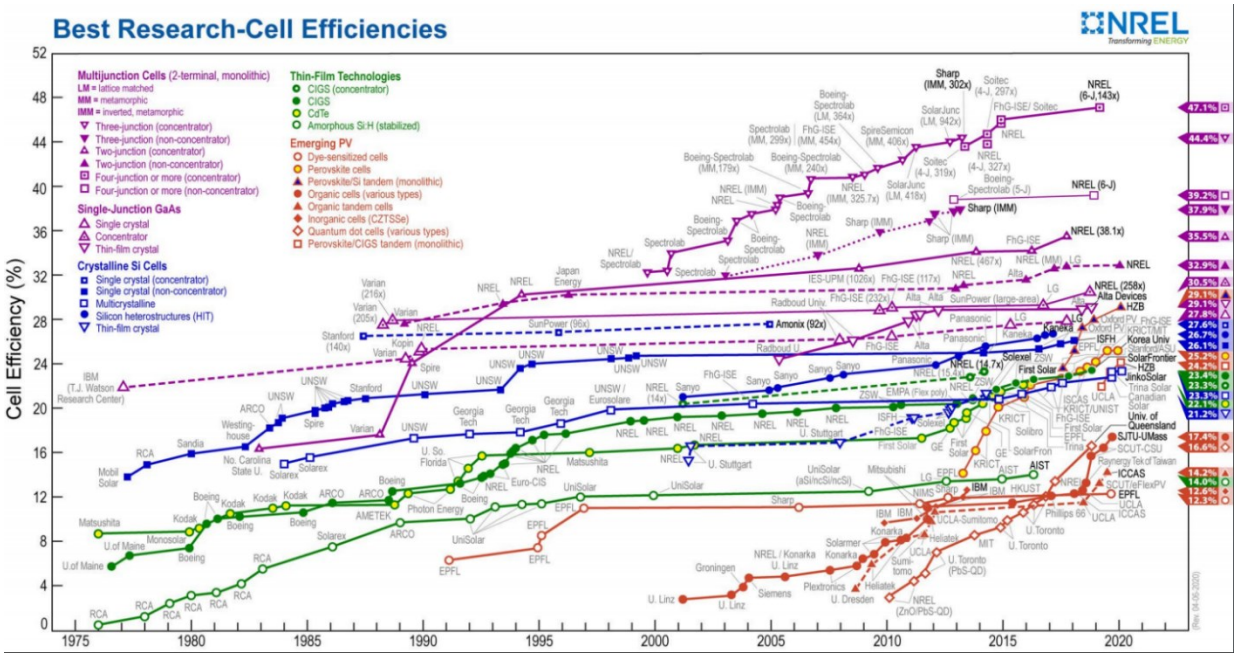

Figure 5 Certified best research-cell efficiency chart[5]

1.1.3 Perovskite Solar Cell (PSC)

A perovskite solar cell is a type of solar cell that includes a perovskite structured compound with hybrid organic-inorganic based material such as methylammonium lead halide in

Figure 6. The use of the perovskite material in solar cell application has been developed over the last few years because the bandgap of this material is 1.55 eV, which is nearly ideal for single-junction solar cell exposed to the solar irradiance spectrum. In addition, this hybrid perovskite shows good absorption coefficient, long charge carrier diffusion length, and ambipolar charge transport, leading to suitable for photovoltaic application. Moreover, the bandgap of the material can be easily tuned in the range of 1.3 eV to 2.3 eV by exchanging the organic and halide ions. Recombination can be suppressed by long carrier lifetime (~100 ns) and the high charge mobility in the range of 10 to 60 $cm^2\ V^{-1}s^{-1}$ which can allow open-circuit voltage over 1 V to be achieved.

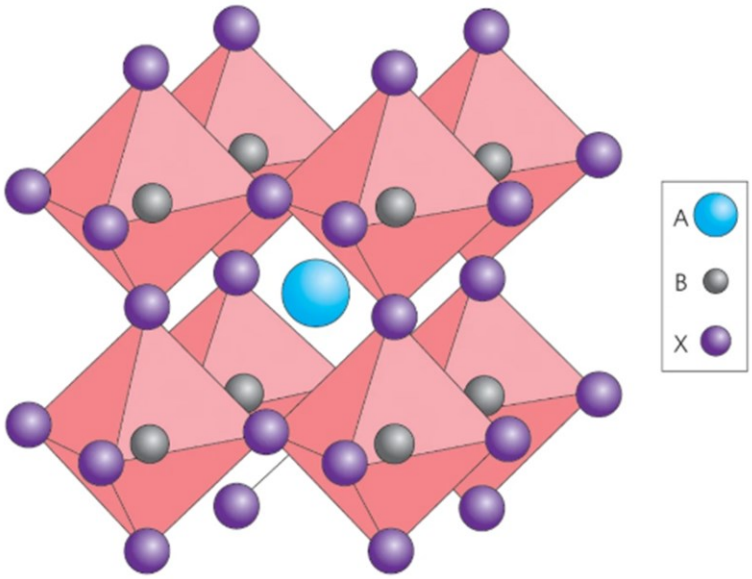

Figure 6 Crystal structure of $CH_3NH_3PbI_3$ perovskite (A = $CH_3NH_3^+$, B = Pb^{2+}, X = I^-)[6]

There are generally three requirements for working process of the solar cells such as light absorption, excited charge separation, and charge collection. In order to construct them, semiconductor material should be selected for the solar cell as a light absorber. For the p-n

junction solar cell, two different types of the light harvesters such as n type semiconductor and p type semiconductor are needed. The exited electrons can flow in n-type semiconductor and holes flow in the p-type semiconductor. For n-i-p junction (i is intrinsic semiconductor), selective electron transport layer (ETL) such as TiO_2, ZnO, phenyl-C61-butyric acid methyl ester (PCBM), and SnO_2 and hole transport layer (HTL) such as NiO, Poly[bis(4-phenyl)(2,4,6-trimethylphenyl)amine (PTAA), and poly(3,4-ethylenedioxythiophene) polystyrene sulfonate (PEDOT:PSS) are required. Depending on charge carrier transport direction, the device structures of PSCs are classified as normal(n-i-p) or inverted(p-i-n) solar cells. The A commonly used normal PSCs consisting of a TiO_2 ETL and Sprio-OMeTAD hole HTL exhibit a higher PCE. These ETL and HTL layers can facilitate charge transport and suppress charge recombination in the perovskite device as shown in Figure 7.

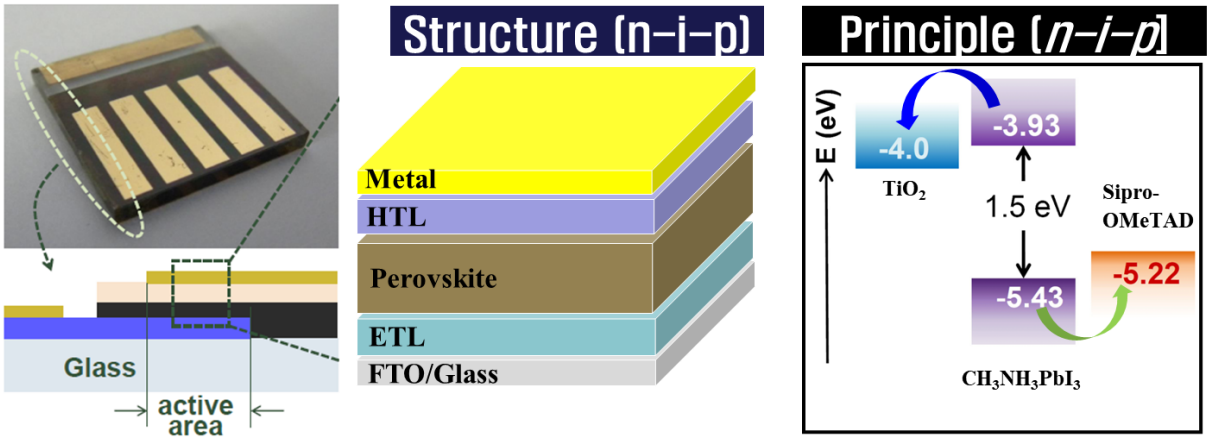

Figure 7 The device structure and the principle of n-i-p junction-based perovskite solar cell

1.2 Device Characterization

1.2.1 Power Conversion Efficiency (PCE)

When a solar cell is exposed to the sun light, the electrical power can be obtained according to this relation:

$$P = Current\ (I)\ \times voltage\ (V) \tag{1.1}$$

and to describe the performance of the solar cell, the current-density (Jsc) - voltage (V) curve is used in Figure 8.

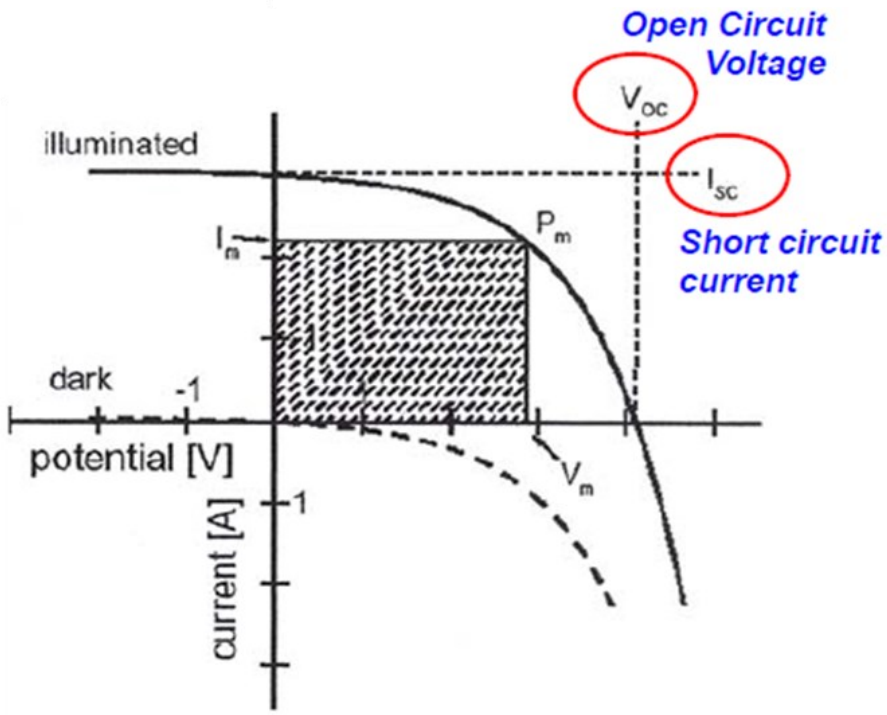

Figure 8 The common I-V curves before (dash line) and after (line) the light illumination on the solar cell[4]

The PCE, which also called the efficiency of a solar cell, is defined by the ratio of maximum output electrical energy to input energy (the incident light) on the solar cell. The current, voltage, and fill factor (FF) are the most important parameters to understand the performance of a solar cell. Short-circuit current (I_{SC}), which is also known as photocurrent, exhibits the generated current of a solar cell without any external circuit. Open circuit voltage (V_{OC}) is a maximum potential energy difference at zero current. Two parameters in the graph show square box in Figure 8 represent theoretical efficiency. The FF, which is a geometric factor of I-V curve, is the ratio of the maximum power to the theoretical power and is defined as a quality of solar cell. Thus, PCE can be given by:

$$\eta = \frac{P_{max}(I_{sc} \times V_{oc} \times FF)}{P_{in}} \tag{1.2}$$

Where η is PCE, P_{in} is power input, and P_{max} is maximum power output. The solar cell performance is measured under 1 sun illumination, where corresponds to standard at AM1.5 for light spectrum or 1 kW/m^2.

The simplified equivalent circuit of a solar cell under illumination shows an applied voltage to extract the excited photocurrent as shown in Figure 9. I_L is the photo-generated current, I_0 is the reverse saturation current of the diode, R_S and R_{SH} are series and shunt resistance respectively, V is the applied voltage across the solar cell. Both factors have negative effects on the performance of solar cell by dissipating power in the resistance. As the parasitic series resistance in a solar cell device increase, it reduces the fill factor of the device but has no impact on the short-circuit current and open circuit voltage. On the other hand, low shunt resistance causes substantial losses of power in a solar cell by an alternate current path for the

photo-generated current. This diversion of current flow reduces the amount of current flowing through the solar cell junction and drops the voltage from the solar cell.

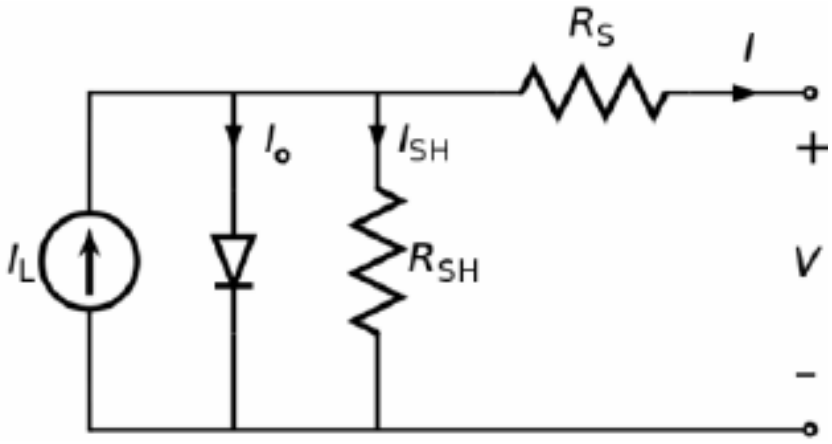

Figure 9 Equivalent electrical circuit of a solar cell under illumination

1.2.2 Incident Photon to Current Efficiency (IPCE)

IPCE or External Quantum Efficiency (EQE) is an important concept in describing the process of absorbed incident photons conversion to the charge carriers. It indicates the ratio of the number of generated charge carriers to the number of incident photons on a solar cell as a function of wavelength. IPCE is simply calculated by the following equation:

$$IPCE\ (\%) = \frac{I_{ph}(mA/cm^2)\times 1239.8(V\times nm)}{P_{incident\ photons}(mW/cm^2)\times \lambda(nm)} \times 100 \qquad (1.3)$$

This shows how efficiently a solar cell absorb incident photon as well as collect the photo-generated carriers as a function of wavelength in order to optimize the solar cell device.

Ideally, the EQE should be 100% but, absorption loss and recombination loss in the device causes drop of EQE. Figure 10 shows the typical EQE results of the perovskite solar cells structured with TiO_2 as ETL and Spiro-OMeTAD as HTL. A significant reduction of the EQE in short wavelength region under 350 nm is attributed to parasitic absorption or front recombination in the front layers. The EQE in long wavelength over 800 nm is decreased due to the inadequate absorption. That region can be utilized to determine the bandgap of the absorber layer in the solar cell device. The overall reduction in EQE can be caused by the reflection loss from the front layer. The layers have different refractive index that can cause the reflected incident light in the range of 300 to 800 nm wavelength, which the perovskite normally absorbs. In addition, EQE results can be used to calculate the integrated current density, which can compare to current density from J-V curve for reliability of the solar cell.

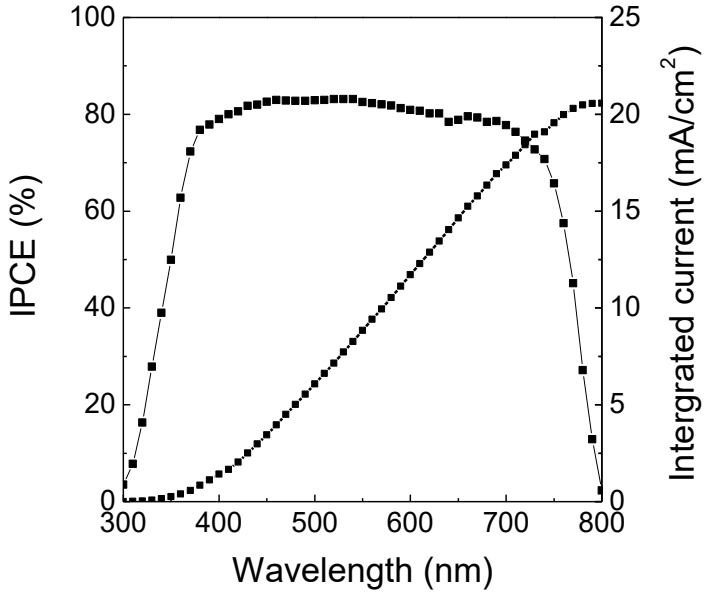

Figure 10 Inset of IPCE and integrated current density of a perovskite solar cellas as a function of incident photon's wavelength

1.3 Challenges of Perovskite Solar Cell

Recently, the PSCs have exceeded 25.5% for a single junction and 28 % for multi junction solar cells with cost-effective fabrication. This new technology has great potential candidate to replace other solar cells in the solar cell market. However, there are still several associated issues for the commercialization such as environmental challenges, stability in hot and humid environment,[7] photocatalytic dissociates,[8] and large hysteresis.[9] The perovskite structure for a solar cell application contains lead (Pb), which is an environmentally hazardous material. On the most serious problems is that it is not stable in hot and humid environment. The material can be degraded at temperature above 150 °C and it can also be decomposed when the device is exposed to moisture. These factors can significantly affect the instability or lifetime of PSCs. Another big challenge is that J-V curve can be changed under different illumination, bias direction, and speed. This is the J-V hysteresis phenomenon, which can be caused by the interface between perovskite and oxide transport layer. This behavior complicates the reliable evaluation of cell performance for practical applications. In this section, I will discuss about the two main challenges for the perovskite solar cell applications.

1.3.1 Perovskite - Oxide Interface Effect on Charge Carrier Transport

Current-voltage (J-V) hysteresis is one of the major issues that limit development of perovskite solar cells. This is observed by varying the direction and the rate of the voltage sweeps. Figure 11(a) shows hysteresis behavior of the PSC structured with TiO_2 ETL and the PSC with PCBM ETL depending on voltage scan directions. The same HTL, Spiro-

OMeTAD, was used to compare between two different interface, perovskite-TiO_2 and perovskite-PCBM. TiO_2 and PCBM have a similar function to passivate the surface of the perovskite layer. In case of TiO_2, which is dielectric material, it can hold charged defect on the surface under external bias while PCBM does not provide any additional charge storage function.

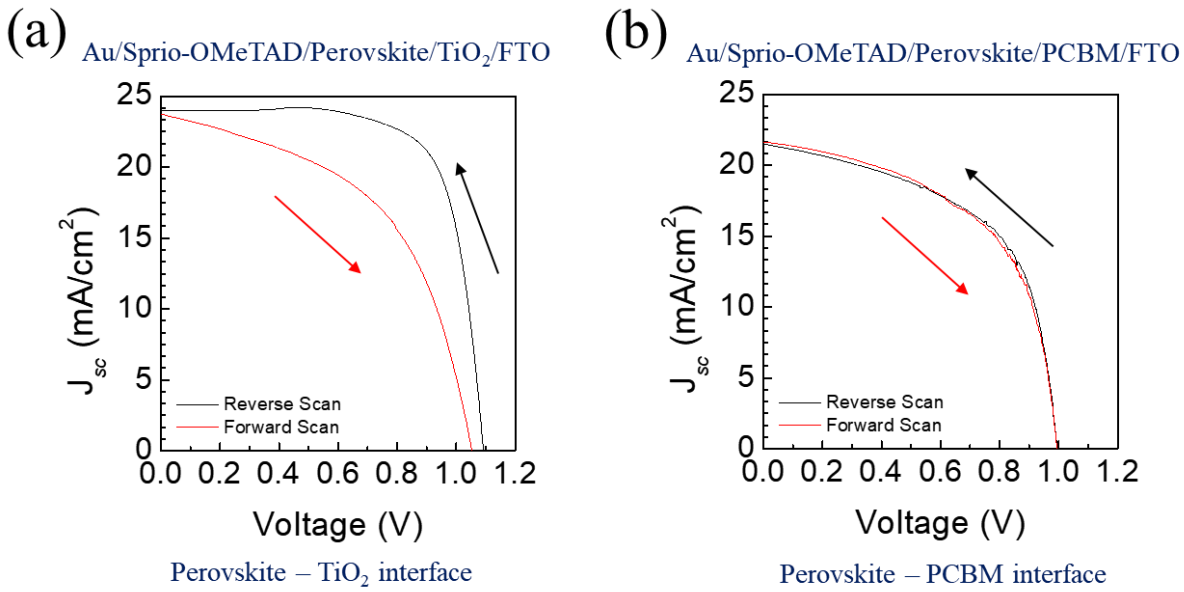

Figure 11 J-V hysteresis of (a) Au/Spiro-OMeTAD/Perovskite/TiO_2/FTO and (b) Au/Spiro-OMeTAD/Perovskite/TiO_2/FTO depending on bias direction

Defects migration and charge trapping in a perovskite film layer can possibly be responsible for the hysteresis by applying a small electric field. When movable defects such as iodide ions migrate to the end of the perovskite and accumulated at the interface between TiO_2 and perovskite, the energy barrier height of the interface is increased. This is because TiO_2 has charge storage function to hold can accumulate movable defects at the perovskite-TiO_2 interface. As a result, the transport of photogenerated electrons from perovskite to the TiO_2 layer is much

more suppressed due to the increased energy barrier at the interface. The hysteresis significantly causes negative effects on the cell stability of the PSCs by aggravating degraded perovskite. On the other hand, Figure 11(b) shows no hysteresis depending on different voltage scan direction when PCBM as ETL is used for the PSC. This is because PCBM can passivate the charge trap state at the perovskite-PCBM interface. It has also high electron mobility and solubility in non-polar solvents. Due to limited solubility, it is still difficult to form defect-free uniform layer. Moreover, aggregated PCBM induces uncovered are of FTO substrate, resulting in bypath for photo-generated electrons. The voltage drops across the device.

1.3.2 Stability of Perovskite ($CH_3NH_3PbI_3$) in Hot and Humid Environment

The long-term stability of PSCs is quite challenging for commercialization. Particularly, the perovskite phase is gradually dissociated when it is exposed to moisture, which is one of the major factors of degradation. Lead halide perovskite material ($CH_3NH_3PbI_3$) is decomposed into PbI_2 and other byproducts by contacting with water molecules, which can be expressed by a series of the following chemical equitation previously reported:[7]

$$CH_3NH_3PbI_3 \text{ (solid)} + H_2O \leftrightarrow CH_3NH_3PbI \text{ (aqueous)} + PbI_2$$

$$CH_3NH_3PbI \text{ (aqueous)} \leftrightarrow CH_3NH_2 \text{ (aqueous)} + HI \text{ (aqueous)}$$

$$4HI \text{ (aqueous)} \leftrightarrow 2I_2\text{(solid)} + 2H_2O \text{ (liquid)}$$

These equations can easily and generally explain that the perovskite (bandgap: ~1.5 eV) phase is decomposed into PbI_2 (bandgap: ~2.3 eV) by observing the color change of perovskite from dark to yellow as shown in Figure 12.

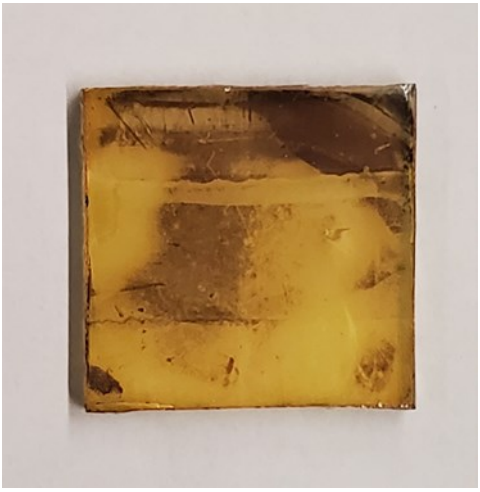

Figure 12 $CH_3NH_3PbI_3$ before and after contacting with water droplet

1.3.3 Stability of Perovskite ($CH_3NH_3PbI_3$) under UV light

Metal oxide such as TiO_2 as ETL is the most common material for the mesoporous perovskite solar cell. This mesoporous TiO_2 extends into photo-active perovskite layer. It plays key roles in collecting selectively electrons and blocking holes, resulting in low recombination rate for charges in photo active perovskite layer. However, performance of PSCs under UV light irradiation will be decreased due to the decomposition of halide perovskite in Figure 13. The degradation of perovskite ($CH_3NH_3PbI_3$) is attributed to the oxidation of the iodide ion. When supraband gap energy is observed, TiO_2 particle can extract electrons from iodide ions through

photocatalytic reaction. Oxidation of the iodide ions subsequently decomposition of $CH_3NH_3^+$. A series of the following chemical equation previously reported can be expressed:[5]

$$2I^- \leftrightarrow I_2 + 2e^- \text{ (at the interface between } TiO_2 \text{ and } CH_3NH_3PbI_3)$$

$$CH_3NH_3^+ \leftrightarrow 3CH_3NH_2 + 3H^+$$

$$I^- + I_2 + 3H+ + 2e^- \leftrightarrow 3HI \uparrow$$

Consequently, $CH_3NH_3PbI_3$ is decomposed into PbI_2 and gas byproduct such as CH_3NH_3 and HI, causing negative effect on photovoltaic performance.

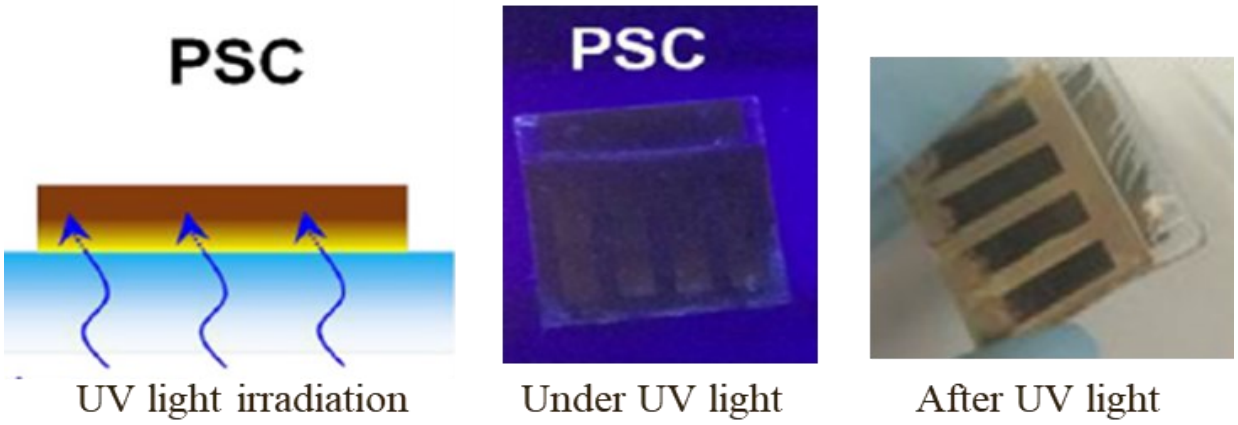

Figure 13 A schematic and photos of the PSC under and after UV light irradiation[8]

1.4 Hypothesis and Objectives

1.4.1 The Perovskite ($CH_3NH_3PbI_3$) – Oxide Interface Effect on Charge Carrier Transport

Depending on the perovskite interface, charge carrier transport behavior can be varied. Charge extraction efficiency can be different due to the perovskite-TiO_2 interface depending on an external bias. This leads hysteresis in the PSC device structured with TiO_2 as ETL. When the forward bias is applied to the PSC, the positively charged ions, which are existed in the perovskite layer as defects, can be accumulated at the perovskite-TiO_2 interface.[9] This can increase the energy barrier height of the perovskite-TiO_2 interface, and the extraction of the photo-generated electrons can be decreased. On the other hand, the perovskite-PCBM interface shows no different charge carrier transport behavior as a function of voltage scan direction. PCBM as ETL in the PSC can passivate the trap states on the surface of the perovskite layer and inhibit defects migration, resulting in less recombination of photo-generated charges. No hysteresis is observed at the perovskite-PCBM interface.

Spiro-OMeTAD HTL in normal PSCs (n-i-p structure) shows a severe morphological deformation over 85 ℃. PSCs will be degraded before perovskite is decomposed into PbI_2 and byproducts by absorption of moisture. NiOx is potentially considered one of the most suitable candidates to replace Spiro-OMeTAD HTL to improve thermal stability of the PSCs. It has a high transparency (Eg: 3.6–4.0 eV), good hole mobility, suitable work function, excellent stability, and effective electron blocking ability in PSCs. In addition, NiO has good interface contact to the perovskite layer.[10-11]

In this study, we aim to solve the hysteresis problem by using the thermal oxidation of e-beam deposited Ni films as HTL, which can form highly crystalline NiO film. For high

temperature oxidation, Ni film must be deposited before fabrication of perovskite layer, which can be dissociated at high temperature (>200 ℃). Thus, the n-i-p structure of PSC is changed to the inverted p-i-n of structure PSC with PCBM ETL. During oxidation of Ni, thermal stress may occur due to the volume expansion from Ni to NiO and form extended defects in the oxidized NiO film. This will have negative effects on the perovskite-NiO interface, resulting in suppressed charge transport behavior. Thermal stress should be released during oxidation to have improved photovoltaic performance.

1.4.2 The Perovskite ($CH_3NH_3PbI_3$) – Oxide Interface Effect under Different Polarity

The field of Resistive switching Random-Access Memory (ReRAM) has become one of the most interesting and active research areas in non-volatile memory technologies, enabling high information storage, low power consumption, and short time for writing and erasing. ReRAM structured with metal-insulator-metal (MIM) is based on redox reactions and ions movement within an insulator layer.[12] This leads to an abrupt resistance change in the ReRAM due to formation and rupture of a conductive filament under an external bias. High resistance state (HRS) is defined as OFF state and los resistance state (LRS) is defined as ON state. The state change from HRS to LRS is termed as SET process and RESET process as LRS returns to HRS as shown in Figure 14. There are a lot of different material, including groups IV and III-V semiconductor, organic compounds, and inorganic material.

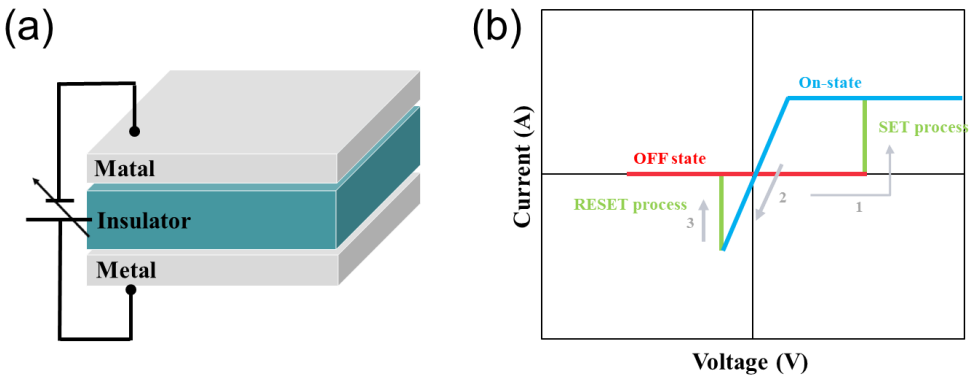

Figure 14 (a) schematic of MIM structure and (b) Bi-polar I-V characteristic of ReRAM device

Hysteresis in the PSCs is caused by movable defects such as vacancies (V_i, V_{MA}, V_{Pb}), interstitials (Pb_i, MA_i, I_i), and antisites (Pb_i, I_{Pb}) depending on scan direction of voltage sweep.[12] The defect migration in the perovskite ($CH_3NH_3PbI_3$) layer under different polarity can be potentially applied to the ReRAM device by the formation of filament. Currently, ReRAM device based on the perovskite material has been developed and proved.

In this project, the perovskite-TiO_2 interface will be used to see the charge transport behavior under different polarity. The hysteresis seen in the PSC due to the perovskite-TiO_2 interface will give different resistive switching behavior in ReRAM device compared to the ReRAM device based on only perovskite layer.

1.4.3 Encapsulated Perovskite ($CH_3NH_3PbI_3$) Solar Cell

The stability of PSCs under damp heat (85/85 °C/RH) is one of most important factors for commercialization. The damp heat test is an accelerated aging test to evaluate the stability of PVs in hot and humid environment. Perovskite ($CH_3NH_3PbI_3$) itself can be decomposed into PbI_2

and byproducts when the PSC device is exposed to humid environment.[13-14] The degradation mechanism for unstable PSCs should be discussed and stability of the device should be enhanced. Various methods are reported to improve stability of PSCs such as tuning structure of perovskite, addition of additives into the perovskite material, change of the device structure, and encapsulation of PSC device. Encapsulation is the one of the most common ways to improve stability of the commercial solar cells such as silicon solar cells and CIGS.[15]

Polymer encapsulation has been used in various fiends such as biomedical, packing for food storage, agriculture, coatings, and adhesives. This technique can also apply to protection layer of the perovskite, which can reduce water contact and penetration due to simplicity and effective passivation. Polymethyl methacrylate (PMMA) is a good candidate for encapsulation. PMMA is synthesized by the polymerization of methyl methacrylate with initiator such as 2,2'-azobisisobutyronitrile (AIBN).[16-17] PMMA, which has a transparent and rigid plastic, is often used to alternate to glass in products such as aircraft windows panes, window shield, canopies. Moreover, it also provides sealing technique to effectively lower the water permeation. However, water molecules can cause hydrolysis of the ester groups in PMMA structure, which can break the PMMA structure.

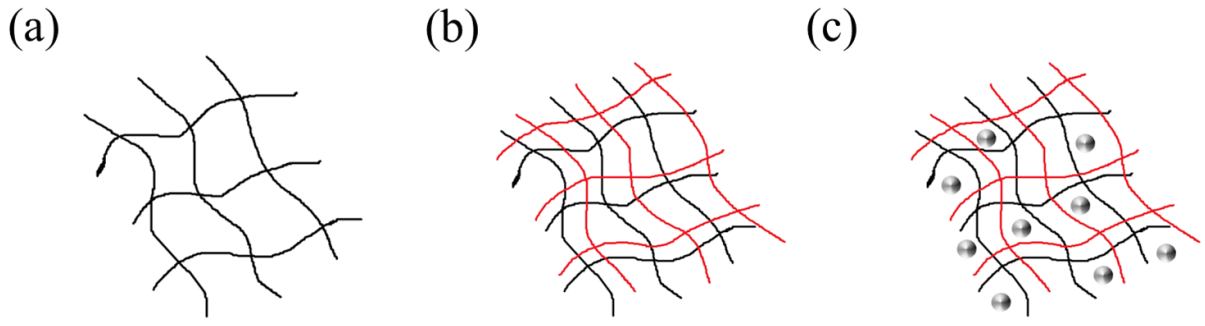

Figure 15 Schematics of (a) singple polymer, (b) interpenerated polymer networks (IPNs) and (c) IPN mixed with nano particles

Interpenetrated polymer networks can be formed by using two different polymers in Figure 15(b). These cross-linked polymers have higher stiffness than that of individual single polymer and the free volume between polymer chains for water penetration can be decreased. PU is good candidate for the IPN because it has good hardness, tensile strength, impact resistance and abrasion resistance. In addition, it can be formed at low temperature.

The goal of this project is to prolonged life of PSCs with the IPN (PMMA-PU) encapsulation layer. Moreover, by addition of nanoparticles such as SiO_2 and CeO_2, nanocomposite IPN can further decrease water permeation rate by decreased volume fraction between polymer chains in Figure 15(c). The nanoparticles can also change wettability of the polymer due to reorientation of the polymer chains. The passivation compared to the individual polymer such as PMMA and PU will effectively suppress the degradation of perovskite under high temperature and humidity (85/85 ℃/RH).

1.4.4 UV-Down Conversion

Another major problem related to UV light is that high-energy UV photons can accelerate solar cell degradation. There are several methods, which have been reported, to address the UV degradation of the perovskite ($CH_3NH_3PbI_3$) by replacing TiO_2 with Al_2O_3, adding Sb_2S_3 interlayer between TiO_2 and perovskite interface, and using UV filter. Although UV filter can improve the stability of the PSC device under UV light, the UV filter reduces the photo excited charges from UV light where the perovskite ($CH_3NH_3PbI_3$) usually absorbs.[8] This leads to lower the PCE of the PSC device. Thus, it is desired to convert the harmful UV photons to usable

visible light that allows to boost PCE of the device and to enhance the device stability under UV light.

In this study, the fluorescent phosphors were selected as luminophore given its commercial availability and added into textured PDMS (Polydimethylsiloxane) as anti-reflective coating (ARC) layer. The textured PMDS layer can produce higher anti reflective properties with more transmitted light improvement by the light scattering on the front surface. Based on the calculation, reflection loss (mA/cm^2) will be decreased from 2.52 to 1.40 if the reflection of ARC film is reduced about 4 % in the range from 400 to 800 wavelength. In addition, phosphors will provide more photon energy by converting the UV light to visible light. The phosphor embedded ARC film will improve the UV stability of the PSC device with the enhanced light absorption of perovskite.

1.5 Thesis Outline

In chapter 2, the thermally oxidized-perovskite interface was studied. NiO from the oxidation of Ni film has high crystalline quality. During oxidation process, thermal stress is developed. In this chapter, the thermal stress in oxidized Ni film and its effect on the carrier transport are discussed.

In chapter 3, the effect of the halide perovskite – oxide interfaces on the carrier transport under an external bias is studied. Unipolar switching behavior of the halide perovskite - oxide interfaces without flipping polarity is measured to see an effect on charge transport. Space charge polarity of the halide perovskite – oxide interface under DC bias is investigated.

In chapter 4, long-term stability test of the encapsulated PSCs was mainly studied. The effect of IPNs as the encapsulation layers on mechanical property and water penetration property depending on the mixing ratio of PMMA/PU was examined. By addition of nanoparticles such as SiO_2 and CeO_2 in IPN structure, surface property of each layer was also analyzed.

In chapter 5, phosphors embedded in ARC layer was mainly studied to boost the PCE of PSCs. The optical property of fluorescent phosphor and ARC layer was investigated respectively. After the film applied to the PSC device, the photovoltaic and IPCE were analyzed.

2.0 Controlled Oxidation of Ni for Stress-Free Hole Transport Layer

This Chapter includes the following published contents:
Lee, S.; Roh, H. -S.; Han, G. S.; Lee, J. -K., Controlled oxidation of Ni for stress-free hole transport large-scale perovskite solar cells. *Nano Research* **2019,** 12, 3089–3094.
DOI: https://doi.org/10.1007/s12274-019-2556-8.
Reprinted by permission from [**Springer Nature**]: [**Springer**] [**Nano Research**] [**18**] (Controlled oxidation of Ni for stress-free hole transport large-scale perovskite solar cells, Seongha Lee et al.) [**COPYRIGHT**] (2019)

2.1 Background and Motivation

Developments in organometal halide PSCs over the last 5 years have provided very fast improvements in the photovoltaic performance. In addition to the PCE improvements, one of the important research subjects in PSCs is to fabricate more stable and reliable devices. To meet this need, extensive research on the device structure, material processing, and physical and electrical properties are currently underway. Depending on the carrier transport direction, the device structures of PSCs are classified as normal or inverted.[19-22] While planar normal PSCs consisting of a TiO_2 ETL and Sprio-OMeTAD HTL exhibit a higher PCE, there are several associated issues, such as large hysteresis, photocatalytic dissociations, and instabilities of additives in HTL.[23-25] The inverted PSCs with NiO HTLs and PCBM ETLs can be used to address these problems by the removal of TiO_2 ETLs and the employment of a stable oxide hole conductor.[26-28]

Compared to polymer p-type semiconductors poly(3,4-ethylenedioxythiophene)-poly(styrene sulfonate) (PEDOT:PSS), NiOx (NiO) is potential candidate material due to a high transparency (Eg: 3.6–4.0 eV), good hole mobility, suitable work function, excellent stability,

and effective electron blocking ability in PSCs.[11] To date, the solution process is widely used for inverted PSCs due to its simple process and compatibility with flexible devices. However, NiO films obtained from the solution process are composed of tiny NiO nanoparticles, which can cause inefficient electron blocking and poor hole transport.[29-31] In addition, it is difficult to deposit uniform NiO films on large substrates by the solution process.[32] Therefore, several techniques, such as e-beam deposition, sputtering, atomic layer deposition, and pulsed laser deposition, have been tested for high quality NiO film depositions.[33-38]

In this study, we investigated the thermal oxidation of e-beam deposited Ni films for stress-free highly crystalline NiO films, which can be applied to the fabrication of large-scale inverted PSCs. The volume expansion during the conversion of Ni to NiO induces compressive residual stress, producing extended defects and the deterioration of the performance of NiO as the HTL.[39] To mitigate the occurrence of NiO residual stress, the surface roughness effect of fluorine doped SnO_2 (FTO) underlying a Ni film was studied. Experimental and simulation results showed that an increase in the surface roughness of the FTO reduced the residual stress of NiO. Inverted PSCs with a thermally oxidized NiO film exhibited a PCE of 16.37%, with a short-circuit current (J_{SC}) of 21.5 mA/cm^2, open circuit voltage (V_{OC}) of 1.04 V, and fill factor (FF) of 0.73 without hysteresis. Moreover, the oxidized NiO film was deposited uniformly on a large-scale substrate, which is applicable to the future large-scale manufacture of PSCs.

2.2 Experimental Section

2.2.1 Preparation of NiO Films

Ni films of thickness 20, 30, and 50 nm were deposited on two different FTO coated glasses (TEC8 and TEC15 from Pilkington) by e-beam evaporation. The surface roughness of the FTO layers were 24.8 and 4.98 nm for the TEC8 and TEC15, respectively. The samples were labelled to represent the thickness of the Ni film (20Ni or 30Ni) and the type of FTO coated glass (T8 or T15), i.e., 20Ni/T8 and 20Ni/T15 refer to 20 nm thick Ni films on TEC8 and TEC15, respectively, and 30Ni/T8 and 30Ni/T15 refer to 30 nm thick Ni films on TEC8 and TEC15, respectively. The FTO coated glasses were cut into square pieces, 20 mm × 20 mm × 0.025 mm, and partially etched using zinc powder and hydrochloric acid (2 M) before the Ni deposition. The substrates were then sequentially cleaned by acetone, deionized (DI) water, and ethanol for 30 min. After Ni film deposition, the Ni/FTO samples were annealed at 550 °C for 6 h in air to form an NiO layer at the top of the FTO.

2.2.2 Fabrication of the PSCs

Inverted PSCs with FTO/NiO/$CH_3NH_3PbI_3$/PCBM/BCP/Ag structures were fabricated by the following sequence. After the Ni film was deposited and oxidized on the FTO/glass substrates, a perovskite ($CH_3NH_3PbI_3$) layer was deposited by the adduct method, as reported previously.[22] The $CH_3NH_3PbI_3$ solution was prepared by dissolving lead iodide (PbI_2), methyl ammonium iodide (MAI, CH_3NH_3I), and dimethyl sulfoxide (DMSO) with a molar ratio of 1:1:1 in N,N-dimethylformamide (DMF). This solution was spin-coated on top of the NiO/FTO at

4,000 rpm for 25 s, while slowly dropping 0.5 mL of diethyl ether. The spin-coated samples were annealed at 60 °C, and then at 100 °C for 1 and 5 min, respectively. The PCBM layer was deposited on the perovskite layer by the spin-coating of PCBM (20 mg) dissolved in dichlorobenzene (1 mL) at 2,000 rpm for 60 s. Subsequently, 5 mg of BCP in ethanol (10 mL) was spin-coated on the PCBM layer at 4,000 rpm for 40 s. Finally, an 80-nm-thick Ag electrode was deposited by thermal evaporation at ~10^{-6} bar through a shadow mask. A deposition rate of Ag electrode is 0.5 Å/s.

2.2.3 Characterization

The crystal structure of the NiO film was obtained by X-ray diffraction (XRD; X'Pert, PANalytical). The surface morphology and cross-sectional view of the samples were examined using a field-emission scanning electron microscope (FESEM; XL-30F, Phillps FEI) and atomic force microscope (AFM, MV-1000, Nanonics). The ultraviolet–visible (UV–vis) transmittance spectra of the NiO films were recorded with a UV–vis spectrometer equipped with an integrating sphere (Lambda35, PerkinElmer). The indentation analysis (Hysitron TriboLab®, Nanomechanical Test Instrument) was conducted with a Berkovich diamond indenter at room temperature. An electrochemical workstation (CHI660, CHI Instrument) system was utilized to obtain the photovoltaic performances of the PSCs. A solar simulator (Oriel Sol 3A class AAA, Newport) was used as a light source, calibrated for the AM 1.5 G condition for a reference Si solar cell (PVM 95). The effective area of the PSCs was defined as 0.14 cm^2 using a non-reflective metal mask.

2.3 Results and Discussion

2.3.1 Crystal Structure, Microstructure and Optical Properties of Oxidized Ni films

The Ni films were deposited on the FTO substrates with different surface roughness (TEC15 and TEC8) by e-beam evaporation. TEC8 was chosen as the rough surface FTO substrate (surface roughness: 24.8 nm), while the TEC15 had a relatively flat surface (surface roughness: 4.98 nm) as shown in Figure 16.

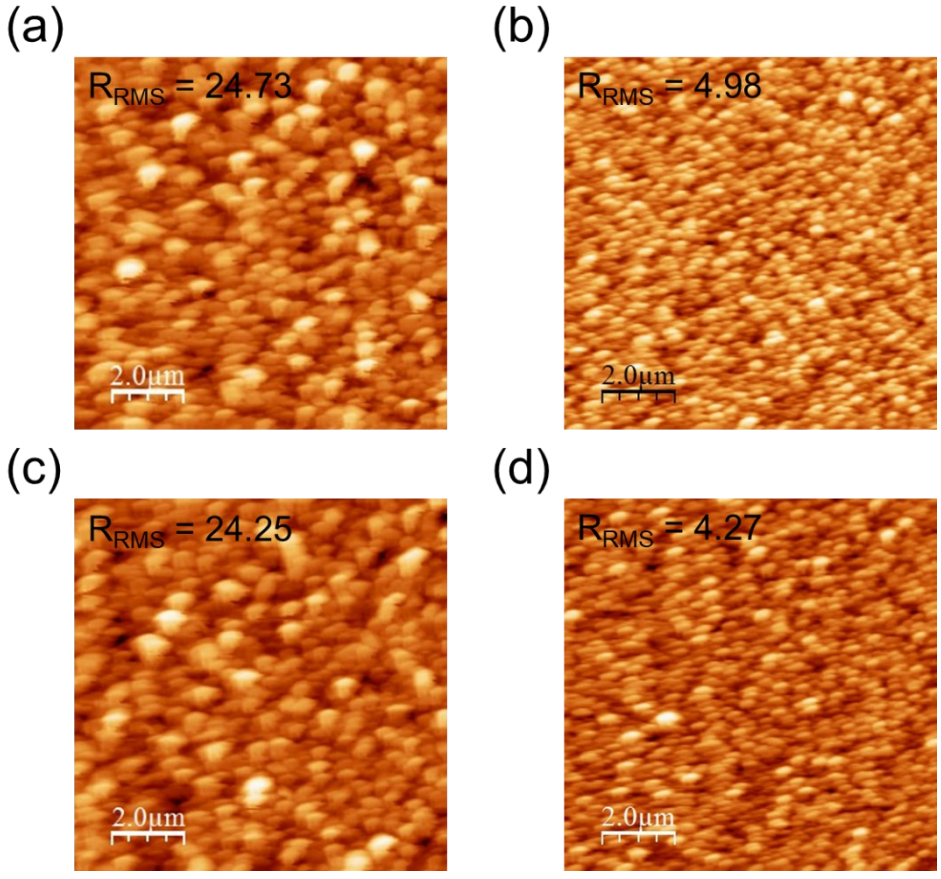

Figure 16 Representative atomic force microscopy images of (a) TEC8 and (b) TEC5, after oxidation of 20 nm thick Ni films on TEC8 and TEC15 at 550 °C for 6 h in air. Formation of 40 nm thick NiO films on (c) TEC8 and (d) TEC 15[18]

The Ni films were thermally oxidized at 550 °C for 6 h in air to form the NiO films. Since the oxygen diffusion coefficient of Ni film is 9.4×10^{-14} cm^2/s at 550 °C, 6 h is long enough to fully oxidize 30 nm thick Ni film as well as 20 nm thick Ni film.[40]

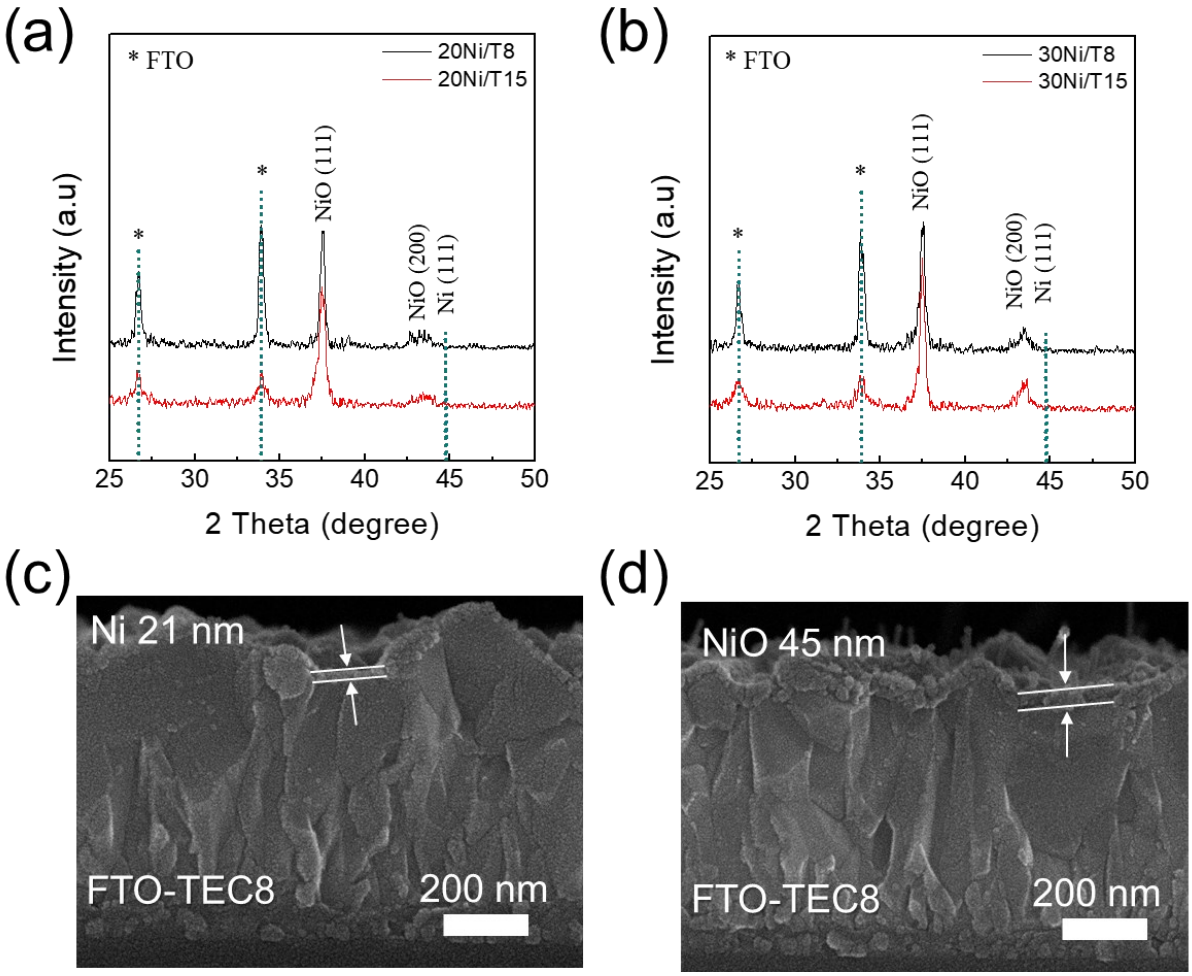

Figure 17 (a) GIXRD patterns of (a) 20 nm and (b) 30 nm thick Ni film on an FTO substrate before and after thermal oxidation. The Ni film was oxidized at 550 °C for 6 h in air. The cross-sectional SEM images of (c) as-deposited 20 nm thick Ni film on a TEC8 FTO substrate and (d) after the oxidization of 20 nm thick Ni film at 550 °C for 6 h in air[18]

Figure 17(a) shows the grazing incidence X-ray diffraction (GIXRD) patterns of Ni on the FTO substrate, before and after oxidation. A peak at 44.7° was indexed as the (111) planes of Ni with a face centered cubic structure. After the oxidation, the two main peaks at 2θ of 37.2° and 43.2° are indexed as the (111) and (200) planes of cubic NiO. Disappearance of Ni phase peak in the oxidized film indicates that Ni was completely oxidized into NiO by the thermal treatment at 550 °C for 6 h in air. Figure 17(c) shows the cross-sectional SEM image of the Ni film on the TEC8 FTO substrate. The thickness of Ni was approximately 20 nm. Figure 17(d) shows the thickness of the NiO film was expanded to ~ 43 nm after the oxidation. Since the weight of the film increases by 127% during the transition from Ni to NiO and the theoretical densities of Ni and NiO are 8.91 and 6.67 g/cm^3, the volume of the oxidized NiO is approximately 1.70 times greater than that of the initial Ni film at room temperature. In addition, the mechanical constraint of the substrate restricts the expansion along the plane direction and the NiO film has additional expansion in parallel to the film thickness direction. By considering Poisson's ratio of NiO, which is 0.3,[41-42] the total thickness of the NiO film is calculated to be 2.21 times greater than that of Ni. The experimental NiO thickness from the oxidation of 20 and 30 nm thick Ni films was 2.05 and 2.14 times than that of Ni, which agrees well with the theoretical value. Figure 18 shows the optical transmittance spectra of the NiO films on different FTO glass substrates. The average transmittances (Tave) of NiO in the wavelength range 400 to 800 nm were 79.0 and 83.8 for the oxidized 20Ni/T8 (20 nm thick Ni film on TEC8) and the oxidized 20Ni/T15(20 nm thick Ni film on TEC15), respectively. Figure 18 shows less light scattering of 20Ni/T15 for the shorter wavelength light and exhibits a slightly higher transmittance at the wavelength of 400–600 nm than 20Ni/T8. This is attributed to a smaller roughness of 20Ni/T15 which is found in Figure 16.[43-44]

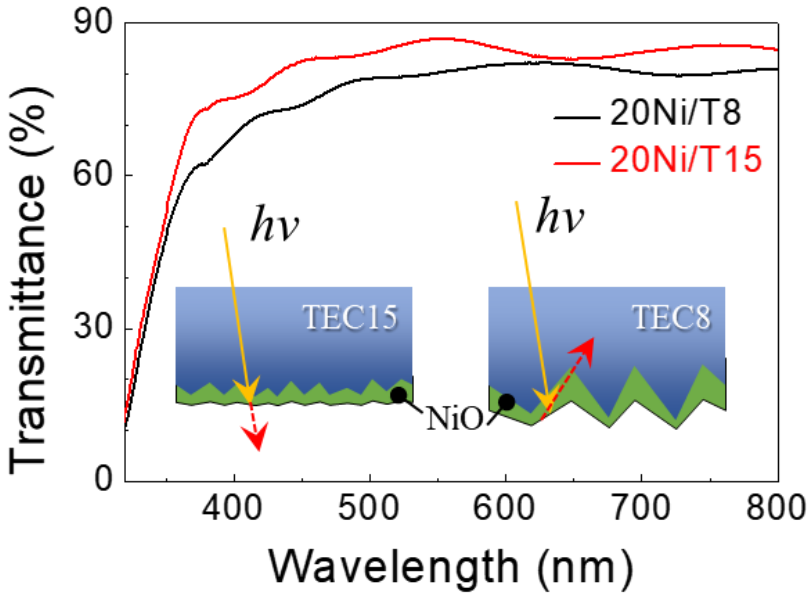

Figure 18 UV–vis transmittance spectra of NiOx films formed by oxidizing the 20 nm Ni films on the TEC8 and TEC15 FTO substrates[18]

2.3.2 Surface Roughness Effect on the Photovoltaic, Electric, and Structural Properties

Figure 19(a) shows representative J–V curves of inverted PSCs using NiO films which were converted from 20 nm thick Ni films on TEC8 and TEC15 (20Ni/T8 and 20Ni/T15). Table 1 shows the device performance parameters of the PSCs. The 20Ni/T8 based PSCs exhibited the best performance; J_{SC} = 21.5 mA/cm^2, Voc = 1.04 V, FF = 0.73, and PCE = 16.37%. Interestingly, although the 20Ni/T15 film had a higher transmittance than that of the 20Ni/T8 film, the device performance of 20Ni/T15 was worse than that of 20Ni/T8. In addition, Figure 19(b) shows that the PSCs using thermally grown NiO film (20Ni/T8) were very reliable. The deviation of the PCEs was much less in the PSCs of the thermally grown NiO film, compared to that in the previously reported PSCs of the spin coated NiO nanoparticle film.[29–31, 37] This

indicates that the NiO film formed by the oxidation of the Ni film was more uniform and reproducible than the NiO film formed by the spin-coating of NiO nanoparticles. Figure 19(a) also shows that both 20Ni/T8 and 20Ni/T15 samples did not exhibit any hysteresis in the J–V curve.

Table 1 Device properties of the PSCs fabricated on different FTO substrate with different Ni thickness[18]

	J_{sc} (mA/cm^2)	V_{oc} (V)	*ff*	*Efficiency* (%)
20Ni/T8	19.9	1.02	0.73	14.82
20Ni/T15	17.9	1.00	0.59	10.56
30Ni/T8	15.7	0.97	0.52	7.92
30Ni/T15	11.3	0.67	0.27	2.04

Since the fabrication process for the samples (20Ni/T8 and 20Ni/T15) was the same, except for surface roughness of the FTO, the electrical properties of the NiO films were investigated to determine the origins of the differences of the PCEs of the inverted PSCs. Figure 19(c) shows that the NiO films on the rough surface have the higher resistance than that of NiO films on smooth surface. To further investigate the mechanisms underlying the effect of the surface roughness of the substrates on the electric resistance of the NiO films, we examined the microstructures of the NiO films on TEC8 and TEC15. Scanning electron microscopy (SEM) images in Figure 19(d) show that the microstructure of the NiO film on TEC8 is dense and uniform. On the other hand, Figure 19(e) shows that blisters with a hemispherical morphology (indicated by a yellow arrow in the SEM images) are formed in the NiO film on TEC15. This blistering produces extended defects in NiO film and increases the leakage current. Therefore,

the NiO film on TEC 15 does not work well as the HTL and deteriorates the performance of inverted PSCs. The formation of blisters and its effect on the electric property of NiO film are explained in detail in a next section.

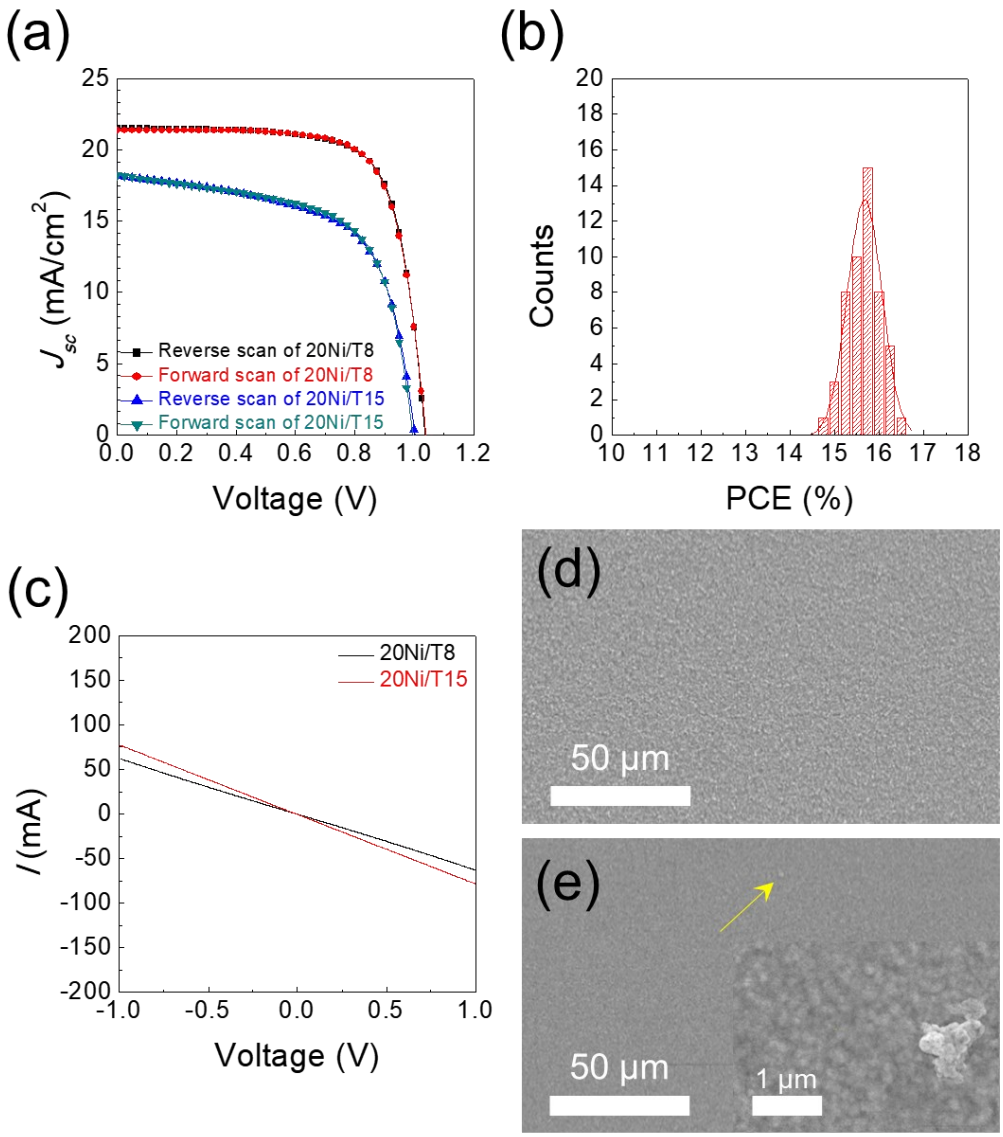

Figure 19 (a) J–V curves of the FTO/NiO/$CH_3NH_3PbI_3$/PCBM/BCP/Ag based PSCs obtained by reverse and forward scans for illumination with the AM 1.5 G condition, and 20 nm thickness Ni films on different FTO substrates after oxidizing. (b) Histogram of the 20Ni/T8 based PSCs. (c) Corresponding resistances of

20Ni/T8 and 20Ni/T15 in air. The measured device structure was FTO/NiO/Au. Plan-view SEM images of the oxidized NiO films on TEC8 and TEC15: (d) 20Ni/T8, (e) 20Ni/T15 after oxidation in air[18]

2.3.3 Further Examination of Surface Roughness Effect Using Thicker NiO Film

In section 2.3.3, the type of FTO substrate has a significant impact on the resistance and I–V characteristics of the oxidized NiO film. To further examine the effect of the surface roughness, another set of experiment was performed using thicker NiO films.

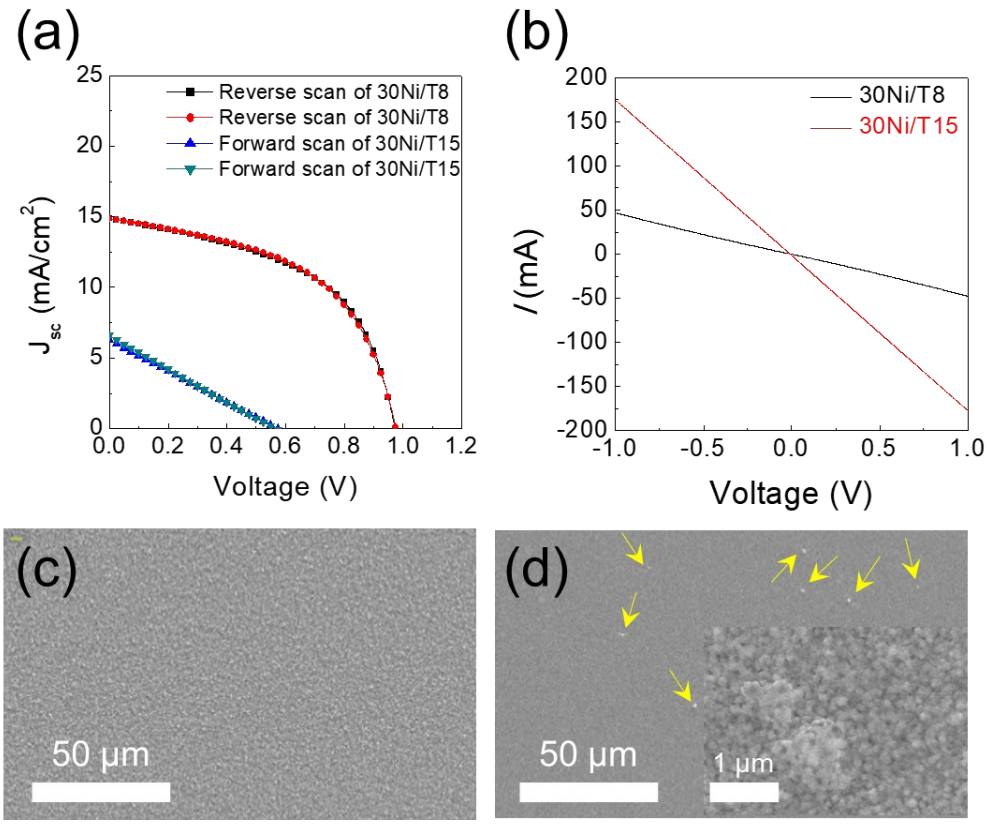

Figure 20 (a) J–V curves of the FTO/NiO/$CH_3NH_3PbI_3$/PCBM/BCP/Ag based PSCs obtained by reverse and forward scans for illumination with the AM 1.5 G condition, and 30 nm thickness Ni films on different FTO substrates after oxidizing. (b) Corresponding resistances of 30Ni/T8 and 30Ni/T15 in air. The measured

device structure was FTO/NiO/Au. Plan-view SEM images of the oxidized NiO films on TEC8 and TEC15: (c) 30Ni/T8, (d) 30Ni/T15 after oxidation in air[18]

Figure 20(a) shows representative J–V curves of inverted PSCs using different NiO films (30Ni/T8 and 30Ni/T15) which were converted from 30 nm thick Ni film. Compared with J–V curves of Figure 19(a), the effect of the surface roughness is more clearly observed in J–V curves of 30Ni/T8 and 30Ni/T15. As shown in Table 1, PSCs of 30Ni/T8 have 4 times larger PCE than PSCs of 30Ni/T15. Overall incident photon-to-electron conversion efficiency (IPCE) spectra of PSCs are shown in Figure 21. Electric resistance in Figure 20(b) indicates that a large difference in PCE of PSCs is due to a dependence of the electric resistance on the surface roughness. 30Ni/T8 is much more resistive than 30Ni/T15.

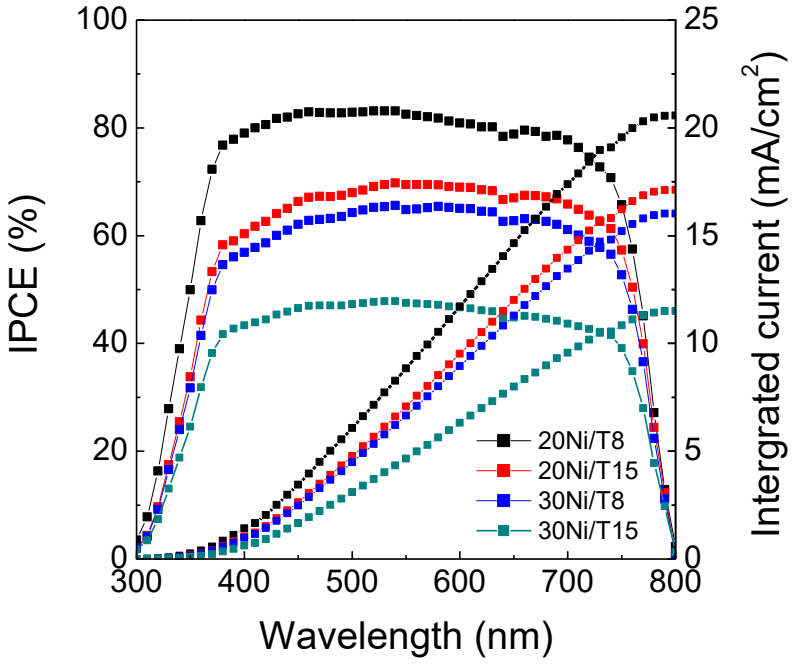

Figure 21 IPCE spectra of the FTO/NiO/$CH_3NH_3PbI_3$/PCBM/BCP/Ag based 20 nm and 30 nm thickness Ni films on different FTO substrates after oxidizing[18]

When Figure 20(b) is compared with Figure 19(c), it is noted that the thicker NiO film from 30Ni/T15 has lower resistance than the thinner NiO film from 20Ni/T15. Given that an increase in the oxide thickness generally increases the electric resistance, an inverse relation between the thickness and the resistance of NiO films on TEC15 needs to be explained. While no blisters are found in NiO film on TEC8 (Figure 20(c)), an increase in the thickness of NiO film on TEC15 increases a density of blisters and their radii. To understand the thickness effect on TEC15, 50 nm thick Ni film was oxidized, and the microstructure of 100 nm thick NiO film was examined. Figure 22 shows the plan-view and cross-section SEM images of 100 nm thick NiO film from TEC 15. It clearly confirms that an increase in the film thickness increases the size of the blisters and even induces partial delamination of NiO film on TEC 15.

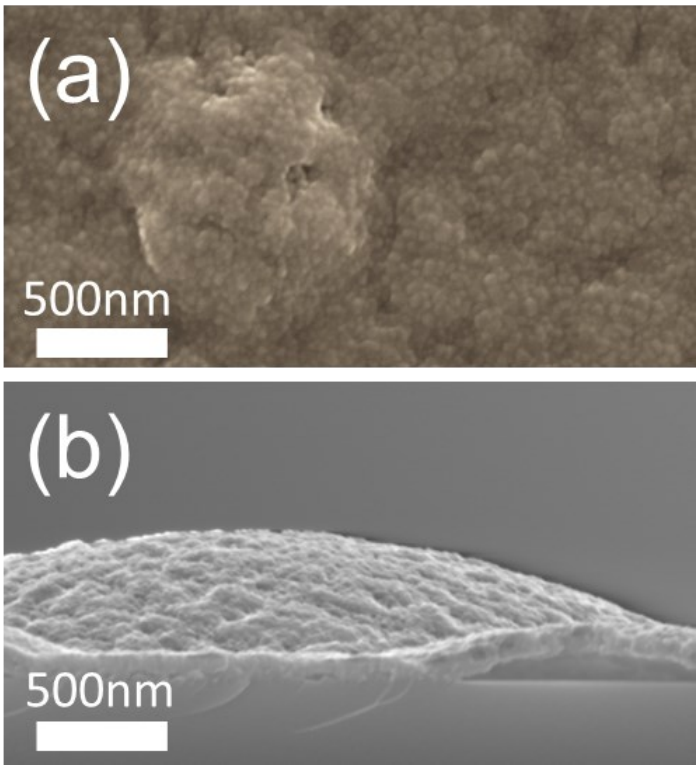

Figure 22 (a) Plan-view SEM images of 100 nm thick NiO film on a TEC15 substrate with high magnifications and (b) Cross-sectional view SEM image of 100 nm thick NiO film on TEC15 by oxidation of 50 nm thick Ni film[18]

It is well-known that the volume expansion during the oxidation of metal thin films on rigid substrates leaves compressive residual stress in the metal oxide films.[39] If an increase in the metal film thickness increases the magnitude of the compressive residual stress beyond a certain limit, the buckling of the oxide films on the rigid substrates occurs and the blistering is promoted.[45] Experimental observations in Figures 19(d), 19(e), 20(c), and 20(d) suggest that the smoother surface of TEC15 increases compressive residual stress in NiO film and an increase in the film thickness increases the magnitude of the residual stress. Extended defects such as dislocations and blisters appear more frequently in such films of higher residual stress, because the residual stress accelerates the diffusion of point defects and promotes the agglomeration of

defects.[46-47] These extended defects tend to increase the leakage current of semiconductors,[48-49] which explains why NiO films from 30Ni/T15 have the lower resistance than NiO films from 20Ni/T15. An increase in the leakage current, in turn, decreases the fill factor and PCE of solar cells by decreasing shunt resistance.[50]

As shown in Figure 19 (a) and 20 (a), the devices based on NiO films shows negligible hysteresis behavior and hysteresis index (HI) of four PSC devices was calculated as shown in Table 2 as defined by following equation:

$$Hystresis\ Index = \frac{J_{RS}\,(0.8\,V) - J_{FS}\,(0.8\,V)}{J_{RS}\,(0.8\,V)} \tag{2.1}$$

Although thicker NiO films on both smooth and rough substrates have more defects in NiO films, charge carrier transport behavior under different scan directions exhibited the same behavior. The thicker NiO layer, which has higher concentration extended defects, influenced on lower charge extraction due to leakage current but it has no effect on hysteresis of the device. These results suggest that the hysteresis can correlate with the strong electrostatic attraction at the interface between the perovskite layer and TiO_2 layer, which is dielectric material while NiO and PCBM do not have high dielectric functions.

Table 2 Hysteresis index of the perovskite solar cells using NiO HTL films on FTO sustreates

HTL [Structure]	*Hysteresis index*
20Ni/T8	0.005
20Ni/T15	0.004
30Ni/T8	0.001
30Ni/T15	0.050

2.3.4 Characterization of Residual Stress

NiO film, the hardness of the NiO films was measured using the nanoindentation method. As the compressive stress prevents the propagation of cracks and increases the hardness,[51] the nanoindentation is a good tool to characterize the status of the residual stress in materials. The same load is applied for the NiO film of the same thickness and the penetration depth is controlled to be less than 1/3 of the film thickness.[52] The hardness of the NiO films was calculated by[53]

$$H = P_{max} / A \tag{2.2}$$

where H is the hardness, Pmax is the maximum applied load and A is the projected contact area of an indent. Figure 23 shows that the hardness of the Ni films before oxidation was almost same for 20Ni/T8 (1.11 GPa) and 20Ni/T15 (1.23 GPa).[54] Similar hardness values were observed for the Ni films from 30Ni/T8 and 30Ni/T15.

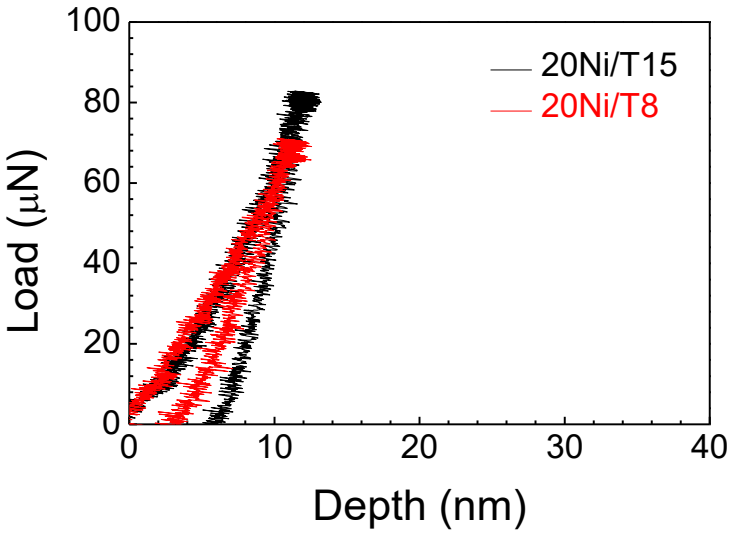

Figure 23 Load-displacement curves from the nanoindentation analysis for the as-deposited 20 nm thick Ni film (before the oxidation process) on FTO15 and FTO8 substrates[18]

However, after oxidation, the NiO films exhibit very different hardness from the load displacement curves of the 20 and 30 nm NiO films on different FTO substrates in Figure 24. Figures 24(a) and 24(b) show that even though a same load was applied, the penetration depth of the NiO film on the rough surface (TEC8) was larger than that on the smooth surface (TEC15). Equation (3) shows that the NiO film from the 20Ni/T15 has a greater hardness (2.88 Gpa) than that from the 20Ni/T8 substrate (2.37 Gpa). The effect of the surface roughness on the hardness of NiO films is more clearly observed in the thicker NiO film. The hardness of NiO films was increased to 4.01 GPa (30Ni/T15) and 2.60 Gpa (Ni30/T8). These hardness values in this study are comparable with that of nanoscale NiO films.[55] The larger hardness of the NiO film on TEC 15 is attributed to larger compressive stress which is developed when Ni film on the flat surface is oxidized.[45] An increase in the film thickness increases the compressive stress, which forms blisters in NiO films and causes delamination at NiO-FTO interface.

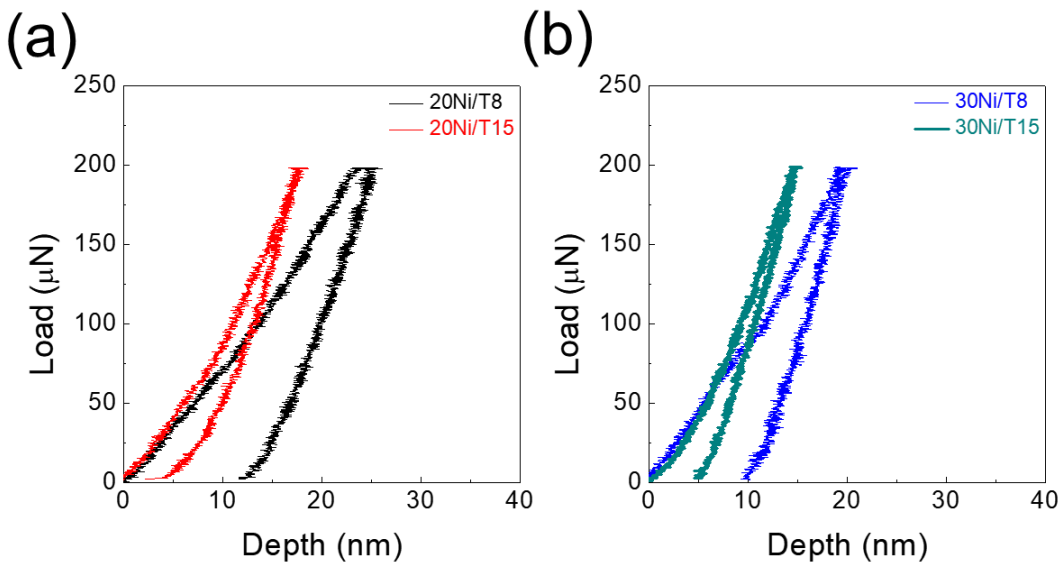

Figure 24 Load-displacement curves of the nanoindentation analysis for (a) 20 and (b) 30 nm Ni thick films on the TEC8 and TEC15 substrate, after oxidation at 550 °C for 6 h[18]

Figure 25 shows Raman spectrum of NiO films. Rougher surface of TEC8 increases the width and intensity of Raman peak at ~ 570 cm^{-1} which is assigned to the first-order one-phonon (1P) longitudinal optical (LO) mode of NiO.[56] The first order 1P LO Raman peak results from symmetry-breaking imperfections and an increase in the imperfection density increases its full width half maximum (FWHM). A peak at ~1,090 cm^{-1} corresponds to the second-order two-phonon (2P) 2LO mode and its FWHM is proportional to Bose-Einstein thermal factor. Since all measurements were done at room temperature, a negligible change is observed in 2P LO Raman peak that is sensitive to temperature. However, 1P peak of 20Ni/T15 is much broader than that of 20Ni/T8. This suggests that 20Ni/T15 has more compressive stress and resultant defects than 20Ni/T8. In 30Ni/T8 and 30Ni/T15, not only FWHM but also the peak position changes. An increase in Raman shift of 30Ni/T15 1P peak from ~550 to ~600 cm^{-1} indicates the development of high compressive stress in thicker NiO films.[57] Raman spectra confirm that the surface

roughness affects the compressive residual stress of the NiO films and thicker NiO film on smoother substrates (30Ni/T15) has the largest compressive stress.

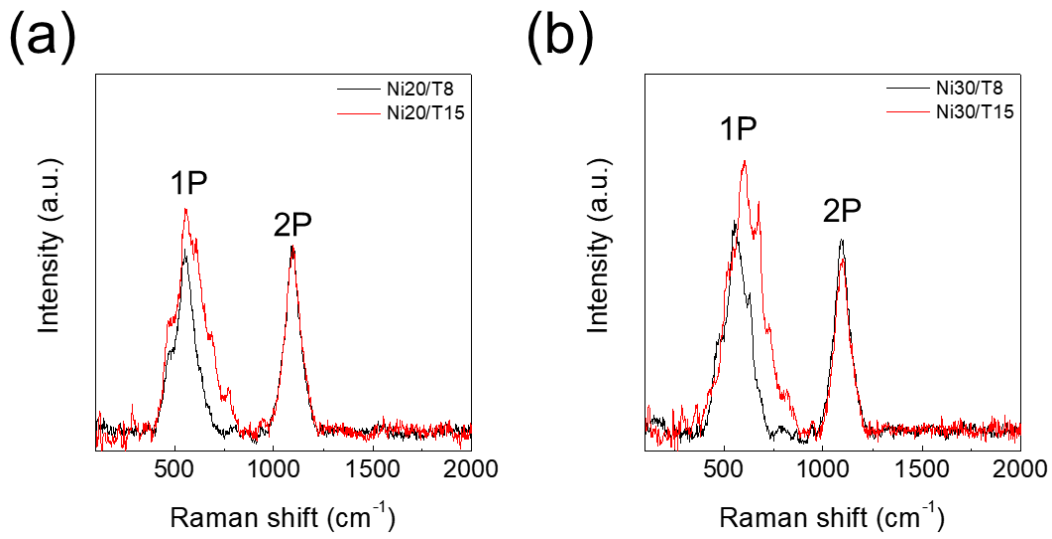

Figure 25 Representative Raman spectra and XRD spectra for (a) 20 nm and (b) 30 nm thickness Ni films on different FTO substrates after oxidizing at 550 °C for 6 h[18]

2.3.5 Computational Simulation of the Origin of Residual Stress

The experimentally measured differences in the compressive stress of the NiO films are theoretically verified using the finite element method. The evolution of the stress and strain of the NiO films on two different FTO substrates was simulated by ANSYS. The calculation is carried out on the assumption that the volume expansion during the oxidation of Ni is prohibited at the interface between the Ni layer and the FTO layer. The stiffness of the NiO films used in the calculation was 89.48 GPa (on TEC8) and 94.12 GPa (TEC15) which were obtained by the nanoindentation. Figures 26(a) and 26(b) show the calculation results of the compressive stress

distributions of the NiO films with smooth and rough surfaces. The addition of oxygen into the constrained Ni films resulted in the NiO films of in-plane compressive stress and out-of-plane tensile strain. The volume of the Ni layer was expected to increase during the oxidation, since oxygen was added to the Ni film and the density of NiO is less than that of Ni. While the NiO layer expanded freely along the normal direction of the substrate, the rigid FTO substrate constrained the expansion of NiO layer along the in-plane direction, causing compressive stress in the NiO layer. Figure 26 shows that the maximum in-plane compressive stress of 13.8 GPa is uniformly applied to the bottom part of the NiO film on the flat surface. On the rough surface, the in-plane compressive stress of NiO film decreased significantly. The maximum compressive stress of NiO film on the rough surface was only 9.8 GPa, which was locally concentrated in the apex region of the NiO-FTO interface. Figures 26(c) and 26(d) show that a larger out-of-plane strain was produced in the NiO layer on the rough surface. This larger strain in the NiO layer on the rough surface relieves the stress, leading to the smaller compressive stress.

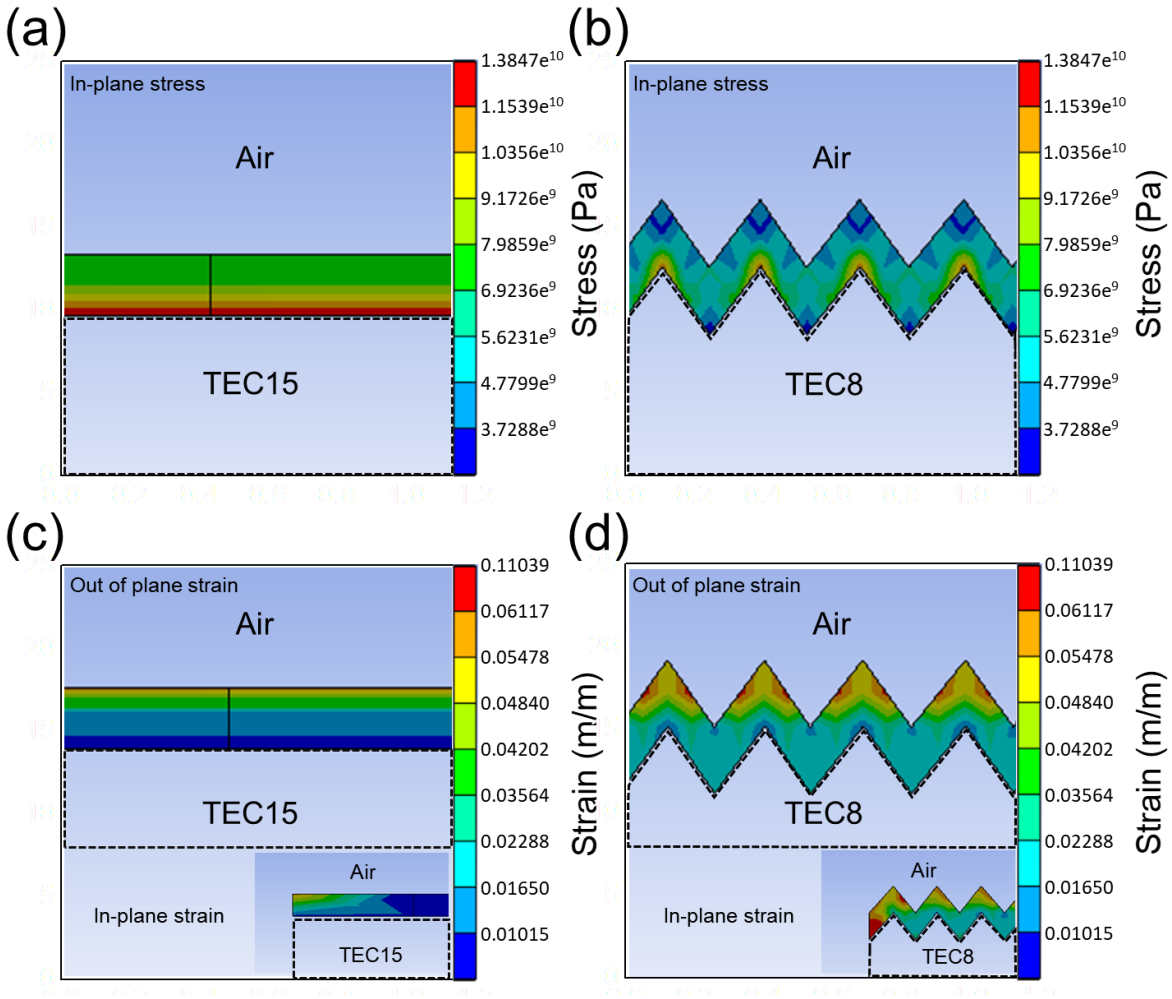

Figure 26 Calculated stress distributions of the NiO films after the oxidation process: on (a) flat and (b) rough surfaces. Calculated strain distributions of the NiO films after oxidation process: on (c) flat and (d) rough surface[18]

The simulation results demonstrate that the rough surface of FTO layer releases the compressive stress of the NiO film more effectively by allowing a higher volume expansion during the oxidation process. In contrast, the compressive stress is developed in NiO film on smoother substrate. As the film thickness increases, higher stress is built up near the NiO-FTO interface and a probability of forming extended defects increases. This suggests that the electron blocking ability of thermally oxidized NiO as a HTL of the PSCs depend on the surface

roughness of the FTO and initial thickness of the Ni film. In addition, Figure 27 shows large NiO/FTO/glass substrates (8 cm × 8 cm) and PCEs of solar cells (2 cm × 2 cm) using different parts of large NiO/FTO/glass substrate. A small variation of PCE suggests that thermally oxidized NiO film is suitable for fabricating large-scale PSCs.

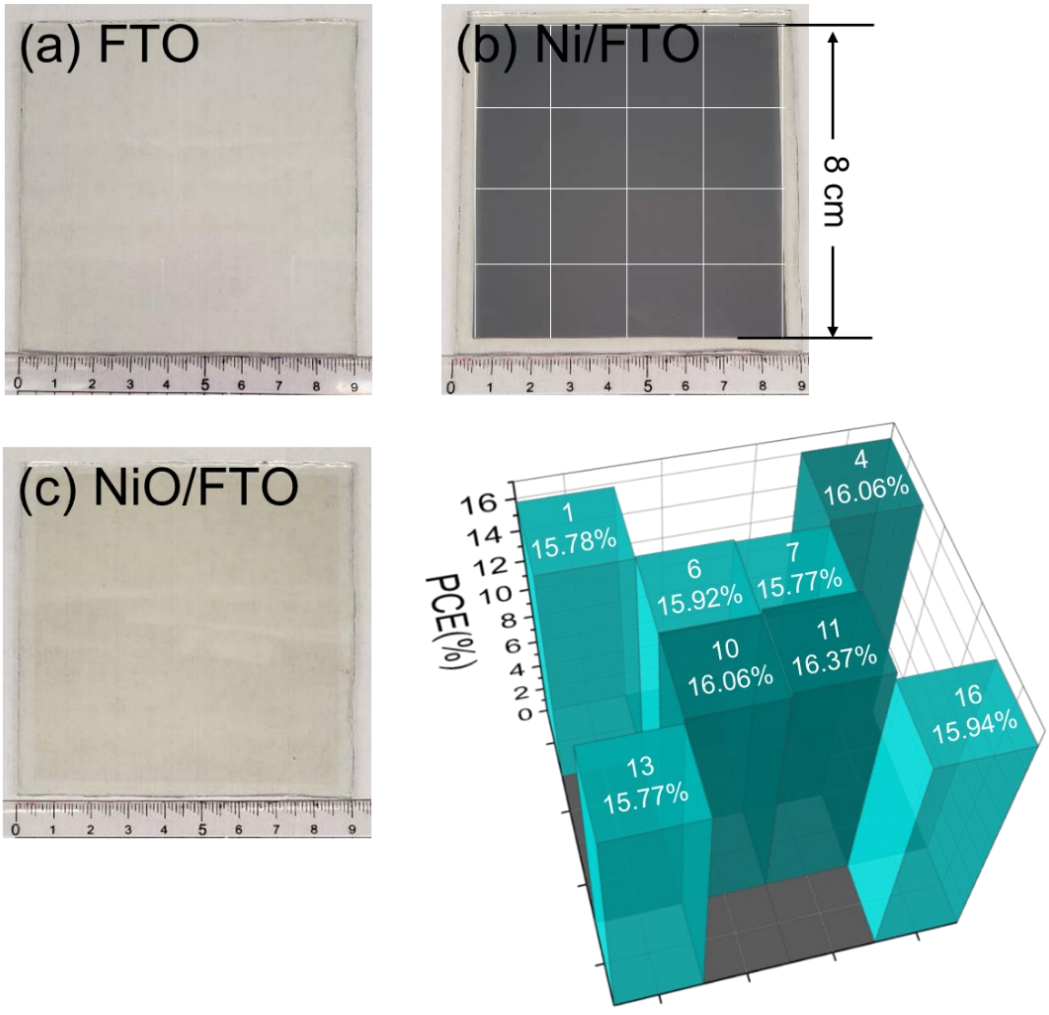

Figure 27 Optical images of (a) uncoated FTO/glass substrate, (b) Ni coated FTO/glass substrate (20Ni/T8, Ni coated area: 8 cm × 8 cm), (c) thermally oxidized NiO coated FTO/glass substrate (20Ni/T8, NiO coated area: 8 cm × 8 cm), (d) PCE of FTO/NiO/$CH_3NH_3PbI_3$/PCBM/BCP/Ag structure PSCs (size: 2 cm × 2 cm) using different parts of large NiO/FTO/glass substrate (20Ni/T8, NiO coated area: 8 cm × 8 cm) [18]

2.4 Conclusion

We systematically studied the electric and mechanical properties of NiO using thermal oxidation, and its effect on the selective hole transport behavior as HTLs of inverted PSCs. When the surface roughness of substrates underlying the Ni film was higher, the thermally oxidized NiO film was more electrically resistive, had less in-plane compressive stress, and provided a better HTL performance. This is due to the evolution of greater out-of-plane strain and the formation of less extended defects. The Ni film on the smooth surface substrate produced more in-plane compressive stress, leading to the formation of extended defects, local blistering, and delamination of the NiO film. As a result, the leakage current of the NiO film increased, and the NiO layer in the inverted PSCs did not effectively block electrons. Stress-free NiO film is an excellent hole transport layer that stops the photogenerated electrons of the perovskite layer from moving to FTO. The improvements in the structural and electrical qualities of the NiO film by engineering the residual stress reduce the carrier recombination and increase the power conversion efficiency of the perovskite solar cells to 16.37%. This result provides a guideline for designing uniform and high-quality NiO films on large substrates, which can be applied to the large-scale manufacturing of PSCs.

3.0 Asymmetric Bipolar Resistive Switching ReRAM based on the Perovskite-TiO_2 Interface

This Chapter includes the following published contents:
Lee, S.; Wolfe, S.; Torres, J.; Yun, M.; Lee, J. -K., Asymmetric bipolar resistive switching of halide perovskite film in contact with TiO_2 layer. *ACS Appl. Mater. Interfaces* **2021**, 13, 27209-27216.
DOI: https://doi.org/10.1021/acsami.1c06278
Reprinted by permission from {58}. Copyright {2021} American Chemical Society.

3.1 Background and Motivation

ReRAM devices have been developed as promising next-generation nonvolatile memory devices in future memory technology due to its simple device architecture, fast operation, and low power consumption.[58-59] To read, write and store data in a same device, ReRAMs use semiconductor or dielectric materials which show hysteresis in current – voltage relation. The resistive switching mechanism is explained by the conductive filament formation of ions and defects,[60-61] and the electrochemical reaction at the interface.[62-63] The ReRAM device is sandwiched structure which is composed of a dielectric layer and two neighbor conducting layers. The switching of resistance is observed in several types of materials including group IV and III-V semiconductor, organic compounds and inorganic materials, but the non-volatile behavior is found mainly in the binary metal oxide.[64-66]

Recently, organic-inorganic hybrid perovskite materials such as methylammonium lead iodide ($CH_3NH_3PbI_3$) have attracted intense interest from scientists and engineers due to the

intriguing properties such as high absorption coefficient, convenient bandgap tunability, and long diffusion length of charge carriers.[21, 67-68] These unique materials properties have a potential to build new photovoltaics (PVs)[69-71], light-emitting diodes (LEDs)[72-74], field effect transistor (FETs)[75], radiation detectors[76], and lasers[77]. Furthermore, certain defects of hybrid perovskite materials, which have a low formation energy, have been also explored. Defects migration and charge trapping in the hybrid perovskite film have a negative impact on the carrier extraction phenomenon and power conversion efficiency of PVs LEDs.[23, 78]

However, the defect drift or migration in the hybrid perovskite materials can be positively utilized to design a novel memory device.[79-82] Because of these mobile ions and defects, I-V curve of the hybrid perovskite film exhibits hysteresis which enables ReRAM devices. Mixed halide perovskites such as $CH_3NH_3PbI_{3-x}Br_x$ and $CH_3NH_3PbI_{3-x}Cl_x$ have been investigated to improve the properties of resistive switching memory.[79, 82] Due to the lower formation activation energy and migration activation energy of bromide vacancies ($V^{\bullet}_{Br}$), the increase in Br content of $CH_3NH_3PbI_{3-x}Br_x$ decreases the onset voltage of the device.[79] The precise resistive switching mechanism of the hybrid perovskite materials depends on their electrode materials. Inert electrode materials such as Au and Pt in contact with the perovskite layer only provide the transport path for charge carriers. Therefore, the intrinsic defects such as iodine interstitials and vacancies cause the resistive switching behavior.[79, 81] However, reactive metals such as Ag and Cu can form the second phase such as AgI and be doped into the perovskite near the electrode/perovskite junction.[29] These reactive ions transport under electric field and directly contribute to the resistive switching behavior of the hybrid perovskite.[80, 82]

An important factor that can influence the carrier transport and defect migration of the halide perovskite film is the $CH_3NH_3PbI_3$ – electrode interface. The TiO_2 - $CH_3NH_3PbI_3$

interface affects the power conversion efficiency of the perovskite solar cells due to the capacitive effect, charge trapping, and ion accumulation at the TiO_2 - $CH_3NH_3PbI_3$ interface.[23] Interface trap states cause the accumulation of electric and ionic charges. This space charge, in turn, inhibits electrons extraction from the perovskite to TiO_2.[33-35] However, the effect of the interface on the carrier transport of ReRAM devices has not been systematically studied.

Herein, we study how the interface between the hybrid perovskite and oxide layers affects the transport of charge carriers and point defects by comparing two different multilayer films (Au/$CH_3NH_3PbI_3$/TiO_2/F doped SnO_2 (FTO) and Au/$CH_3NH_3PbI_3$/ FTO). The inert Au was used as a top electrode to prevent electrochemical reaction with perovskite layer from the Au electrode. It is found that an addition of TiO_2 layer between CH_3NH_3PbI and FTO increased Schottky junction barrier height at the interface when the negative bias is applied to the Au electrode. Strong electrostatic attraction between I_i' and $V_O^{\cdot\cdot}$ caused the larger space charge polarization and higher on/off ration (10^3), and reliable retention time, over 10^4 seconds in the Au/$CH_3NH_3PbI_3$/TiO_2/FTO structure. The space charge of ions which are electrically bound to the TiO_2 – perovskite interface leads to a very asymmetric I-V curves.

3.2 Experimental Section

3.2.1 Preparation of TiO_2 Film on FTO substrate

Before depositing the hybrid perovskite layer, a half of FTO coated glasses (TEC15 from Pilkington) were coated with dense 20 nm thick TiO_2 film using an atomic layer deposition (ALD) system. FTO coated glasses were cut and then sequentially cleaned by acetone, deionized (DI) water, and ethanol for 15 min, respectively. Tetrakis(dimethylamido)titanium (TDMAT) as a precursor was heated at 75 °C for a sufficient vapor pressure. The temperature in the reaction chamber was kept at 60 °C for the deposition with the processing pressure ~ 0.2 Torr. High-purity N2 (flow rate, 20 sccm) was used as the carrier and purging gas. The set-up program was as follows: 150 ms pulse of TDMAT, 10 s purge of N_2, 500 ms pulse of H_2O, and 15 s purge of N_2 for every full cycle. TiO_2 layer was grown with a deposition rate of 0.05 nm/cycle.

3.2.2 Fabrication of the ReRAM Device

$Au/CH_3NH_3PbI_3/TiO_2/FTO$ or $Au/CH_3NH_3PbI_3/FTO$ structures were fabricated on TiO_2/FTO/glass or FTO/glass substrates. A perovskite ($CH_3NH_3PbI_3$) precursor was prepared by an adduct method, as reported previously.[22] Lead iodide (PbI_2), methyl ammonium iodide (MAI, CH_3NH_3I), and dimethyl sulfoxide (DMSO) with a molar ratio of 1:1:1 are dissolved in N,N-dimethylformamide (DMF) and then stirred for 45 min. This liquid solution was spin-coated on top of the TiO_2/FTO at 4000 rpm for 25 s, and after 10 s, 0.5 ml of diethyl ether was rapidly dropped onto the substrates. The spin-coated samples were annealed at 60 °C and 100 °C for 3

and 10 min, respectively. Finally, a 60 nm-thick Au electrode was deposited on the shadow-masked perovskite film by the e-beam evaporation.

3.2.3 Characterization

The crystallographic information of deposited films was obtained by X-ray diffraction (XRD; X'Pert, PANalytical). The surface morphology and cross-sectional view of the devices were examined using a field-emission scanning electron microscope (FESEM; XL-30F, FEI). Current-voltage characterization and retention performance were measured by a probe station at room temperature. An external bias was applied to the top Au electrode with the FTO bottom electrode grounded in a voltage sequence of 0 V → 2 V → 0 V → −2 V → 0 V.

3.3 Results and Discussion

3.3.1 ReRAM Device Schematic, and Crystal Structure and Microstructure of $CH_3NH_3PbI_3$

The device schematic of the Au/$CH_3NH_3PbI_3$/TiO_2/FTO structure are shown in Figure 28(a). A cross-sectional SEM image of 200 nm thick $CH_3NH_3PbI_3$ perovskite film deposited on TiO_2 (20 nm)/FTO substrate is also shown in Figure 28(b). The $CH_3NH_3PbI_3$ perovskite layer was uniformly crystallized on the TiO_2 layer without pin-holes. Figure 28(c) shows that the perovskite layer consists of grains with the size of 325 nm on average. XRD patterns of the $CH_3NH_3PbI_3$/TiO_2/FTO structure in Figure 28(d) exhibit strong peaks of the perovskite phase at 14.1°, 28.5°, and 31.9°, which are assigned to the tetragonal structure of (110), (220), and (312) planes. No impurity peaks were observed from the formation of the perovskite structure on the TiO_2/FTO substrate. Each main peak of anatase and rutile TiO_2 from the standard spectrum exhibits at 25.28° (JCPDS no.:21-1272 for anatase) and 27.45° (JCPDS no.: 21-1276 for rutile), respectively. However, diffraction peaks of TiO_2 were not observed from the TiO_2/FTO substrate, suggesting that low temperature ALD deposition of TiO_2 results in an amorphous structure.[88-90]

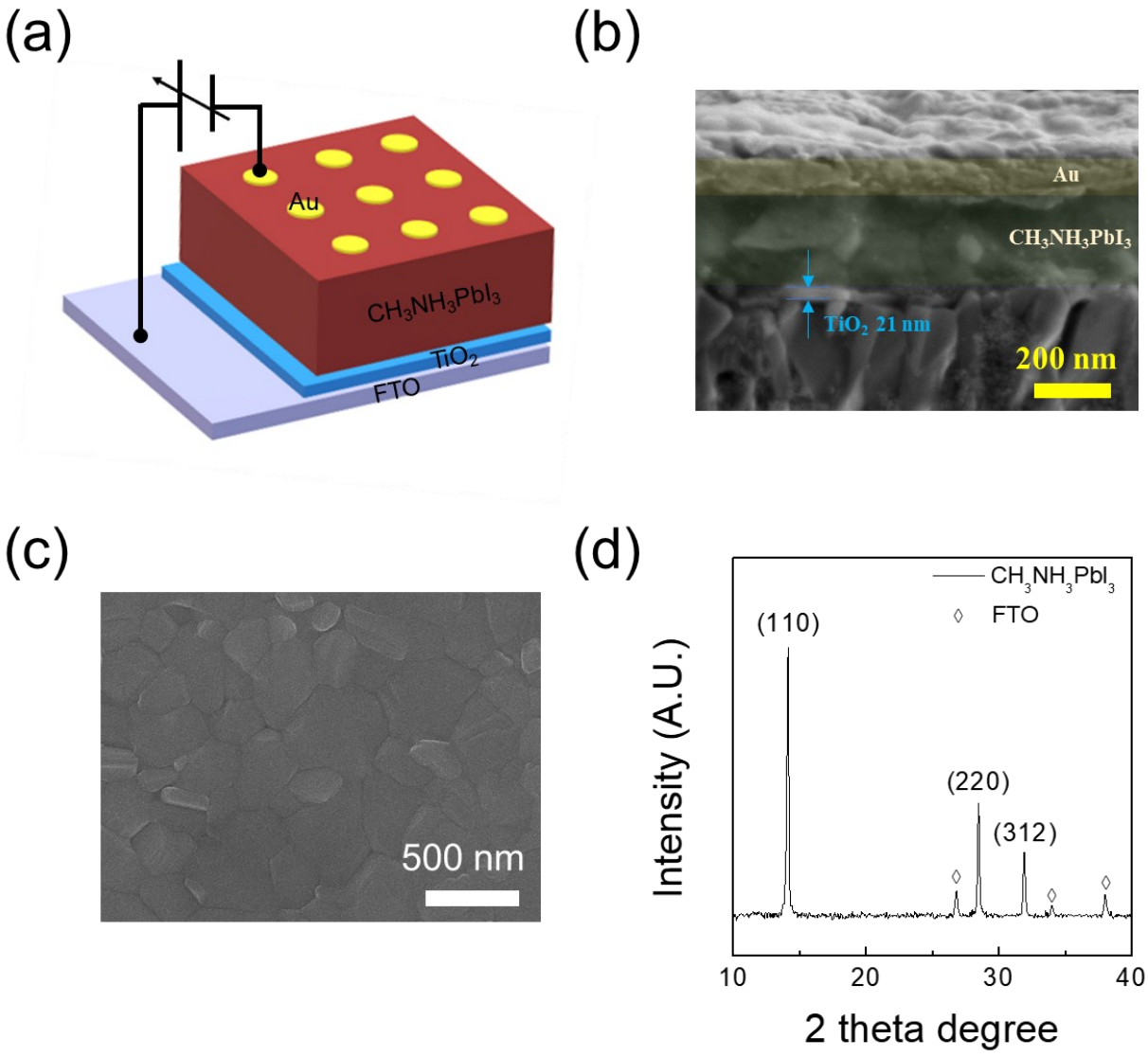

Figure 28 (a) A schematic of the device structure: Au (top electrode)/$CH_3NH_3PbI_3$/TiO_2/FTO (bottom electrode), (b) Cross-sectional and (c) plan SEM images of the device,(d) XRD patterns of the $CH_3NH_3PbI_3$ layer fabricated on the TiO_2/FTO substrate[58]

3.3.2 I-V Curves under Different Polarity of Au/$CH_3NH_3PbI_3$/FTO and Au/$CH_3NH_3PbI_3$/TiO_2/FTO Devices

Figures 29(a) and 29(b) show I-V curves of Au/$CH_3NH_3PbI_3$/FTO and Au/$CH_3NH_3PbI_3$/TiO_2/FTO. The insertion of TiO_2 layer results in a very asymmetric switching behavior. For I-V curve measurement, electric bias with a sequence of 0 V → 2 V → 0 V → −2 V → 0 V was applied to the Au electrode. During the I-V curve measurement, the FTO substrate was grounded. As the voltage sweeps from 0 V to 2 V, a sudden increase in current is found at 0.85 V. This process is called a "SET" process, as the resistance state of the device changes from an initial high resistance state (HRS) to a low resistance state (LRS). After the device turned to LRS, electric current remains. At V = -1.4 V, the resistance state switches to a high resistance state (HRS), which is called "RESET" process. On the other hand, the Au/$CH_3NH_3PbI_3$/FTO device exhibits a more symmetric I-V curve with the set voltage at 1.4 V and the reset voltage at -1.1 V. Since the Au/$CH_3NH_3PbI_3$/FTO structure does not have a TiO_2 layer, it has lower resistance than the Au/$CH_3NH_3PbI_3$/TiO_2/FTO structure in HRS.

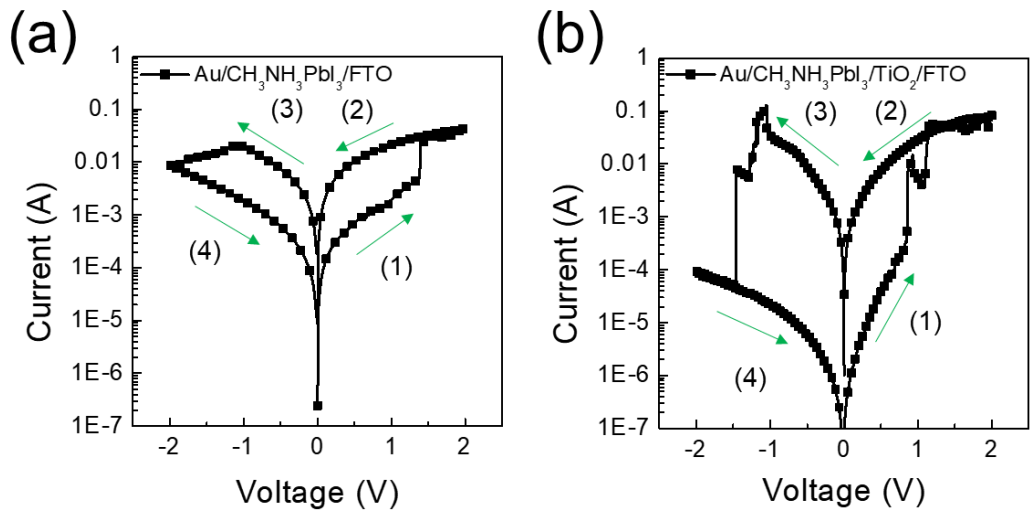

Figure 29 I–V curves of (a) Au/$CH_3NH_3PbI_3$/FTO and (b) Au/$CH_3NH_3PbI_3$/TiO_2/FTO devices[58]

Table 3 shows I(LRS)/ I(HRS) of Au/$CH_3NH_3PbI_3$/FTO and Au/$CH_3NH_3PbI_3$/TiO_2/FTO at 0.85V and -0.85V, which quantifies the asymmetry of the Au/$CH_3NH_3PbI_3$/TiO_2/FTO structure. It is noted that I(LRS)/I(HRS) is the largest when the negative bias is applied to Au/$CH_3NH_3PbI_3$/TiO_2/FTO.

Table 3 I(LRS)/I(HRS) values of both Au/$CH_3NH_3PbI_3$/FTO and Au/$CH_3NH_3PbI_3$/TiO_2/FTO ReRAM devices at 0.85 V and -0.85 V[58]

	I(LRS)/I(HRS) at 0.85 V	I(LRS)/I(HRS) at -0.85 V
Au/$CH_3NH_3PbI_3$/FTO	13.27	11.13
Au/$CH_3NH_3PbI_3$/TiO_2/FTO	31.43	1530.71

To emphasize the role of TiO_2 on this resistive switching device based on the hybrid perovskite material, non-reactive Au electrode was utilized. Thus, only the perovskite-TiO_2 interface effect on charge transport can be observed. On the other hand, reactive metals such as Ag and Cu can form the second phase such as AgI and be doped into the perovskite near the electrode/perovskite junction.[83] These reactive ions transport under electric field and dominantly contribute to the resistive switching behavior of the hybrid perovskite. Figure 30 shows I-V curves of Ag/$CH_3NH_3PbI_3$/FTO and Ag/$CH_3NH_3PbI_3$/TiO_2/FTO devices. The TiO_2 layer also promotes the switching behavior in the devices of Ag electrode. In addition, their overall performance as switching devices is not as good as Au/$CH_3NH_3PbI_3$/FTO and Au/$CH_3NH_3PbI_3$/TiO_2/FTO devices. It is due to the formation of the second phase such as AgI at the Ag/$CH_3NH_3PbI_3$ interface. AgI is doped into the perovskite near the electrode/perovskite junction and changes the electric properties of $CH_3NH_3PbI_3$. This shows that Au in contact with the perovskite layer is useful to examine the migration of intrinsic defects ($V_I^{\bullet}$ and I_i') of $CH_3NH_3PbI_3$ and their interaction with the TiO_2 interface.

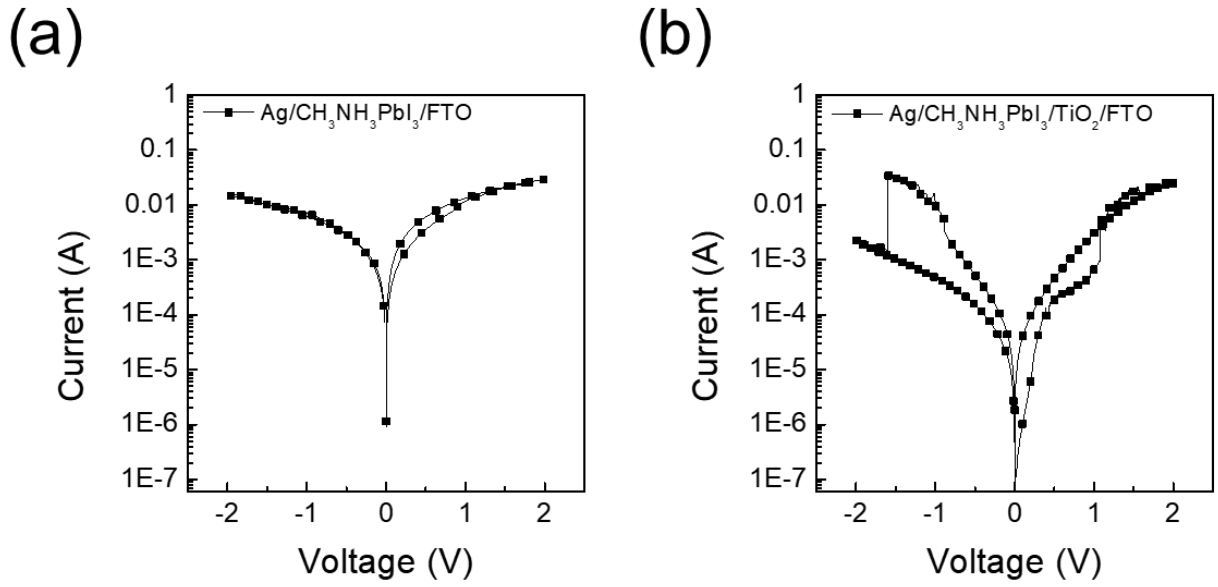

Figure 30 I–V curves of (a) Ag/$CH_3NH_3PbI_3$/FTO and (b) Ag/$CH_3NH_3PbI_3$/TiO_2/FTO devices

3.3.3 Resistive Switching Mechanism of both Au/$CH_3NH_3PbI_3$/FTO and Au/$CH_3NH_3PbI_3$/TiO_2/FTO Devices

The physical origin of the asymmetric I-V curve is related to how defects are accumulated at different interfaces. The switching mechanism of the halide perovskite is explained by the formation and rupture of the defect chains.[79-82] Out of several vacancies (V_i, V_{MA}, V_{Pb}), interstitials (Pb_i, MA_i, I_i), and antisites (Pb_i, I_{Pb}), V_I has the low formation energy and the highest defect concentration. In addition, the migration energy of I_i (0.15 eV) and V_I (0.25 eV) is much lower than that of Pb^{2+} (0.84 eV) and $CH_3NH_3^+$ (2.31 eV) in the $CH_3NH_3PbI_3$ layer.[42-44] Therefore, abundant and mobile $V_I^{\cdot}$ and I_i' defects set a conductive pathway under external bias and the perovskite layer turns from HRS to LRS. The conduction mechanism of the film has been described with hopping of injected electrons.[93] It is because $V_I^{\cdot}$ defects play a role of trap sites in the $CH_3NH_3PbI_3$ layer below the conduction band of $CH_3NH_3PbI_3$. Once the mobile $V_I^{\cdot}$ defects form a continuous chain, $V_I^{\cdot}$ provides a conductive path for the injected electrons. Trap-to-trap hopping of electrons at nearby $V_I^{\cdot}$ defect sites turn the perovskite layer to LRS. To reset the film from LRS to HRS, an opposite electric to rupture the conduction path. Figure 31 schematically explains the migration and alignment of defects and Figures 31(1) – (4) correspond to the stage (1) – (4) of I-V curve of Au/$CH_3NH_3PbI_3$/TiO_2/FTO in Figure 29(b).

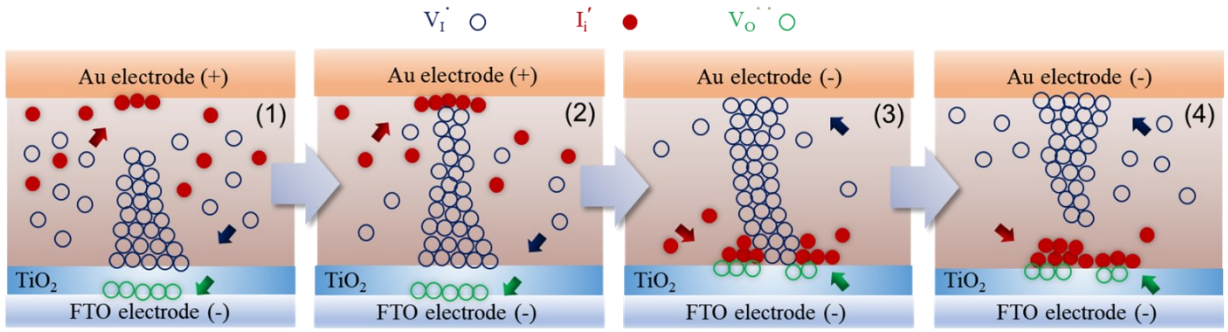

Figure 31 Schematic diagrams corresponding to stages (1) – (4) in Figure 30(b) are (1), (2), (3), and (4) [58]

A main difference between Figure 31(2) and 32(4) is that the interstitial defects in the perovskite layer can make a strong bond with TiO_2 in Figure 31(4), since positively charged oxygen vacancies in TiO_2 can drift under DC bias.[47] However, Au/$CH_3NH_3PbI_3$/FTO device shows similar interstitials defect alignment at the Au - $CH_3NH_3PbI_3$ interface and $CH_3NH_3PbI_3$ – FTO interface shown in Figure 32 (2) and (4). This is because interstitials defects have the same bond strength with Au and FTO under DC bias.

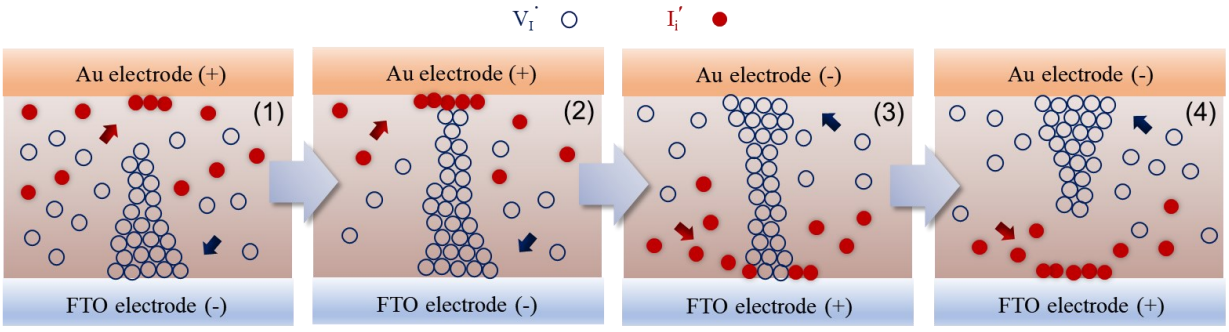

Figure 32 Each schematic diagram, (1) – (4) are corresponding to the stages (1) – (4) in Figure 29 (a) [58]

When the negative bias is applied to Au, the oxygen vacancies move toward the $CH_3NH_3PbI_3$ - TiO_2 interface and hold the negatively charged iodine interstitials. In comparison

to the $CH_3NH_3PbI_3$ - Au interface [Figure 31(2)], more I_i' are accumulated at the $CH_3NH_3PbI_3$ - TiO_2 interface [Figure 31(4)] due to the strong electric affinity between negatively charged I_i' and positively charge $V_O^{\cdot\cdot}$. This I_i' accumulation layer at the $CH_3NH_3PbI_3$ - TiO_2 interface can produce space charge and increase the barrier height at the $CH_3NH_3PbI_3$ - TiO_2 interface. In contrast, when the positive bias is applied to Au, the most abundant $V_I^{\cdot}$ mainly forms the chain and the most mobile I_i' moves toward the Au electrode. Since the perovskite - Au interface is Ohmic and there is no strong electrostatic attraction between I_i' and Au, a part of I_i' near Au does not have a large impact on the resistance. The space charge effect at the $CH_3NH_3PbI_3$-TiO_2 interface also explains why I-V curve of Au/$CH_3NH_3PbI_3$/FTO is much more symmetric than that of Au/$CH_3NH_3PbI_3$/TiO_2/FTO. In a case of Au/$CH_3NH_3PbI_3$/FTO, the high electron concentration of FTO shields $V_O^{\cdot\cdot}$ and the migration of $V_O^{\cdot\cdot}$ under the bias is not significant in FTO. Hence, I_i' may not be strongly bound to the $CH_3NH_3PbI_3$ - FTO and the space charge is not large enough to produce the very asymmetric I-V curve.

3.3.4 Reliability and Reproducibility of both Au/$CH_3NH_3PbI_3$/FTO and Au/$CH_3NH_3PbI_3$/TiO_2/FTO Devices

Figure 33(a) and Figure 33(b) show the retention performance of two devices, which is another good performance indicator of the ReRAM device.[91] The test for both devices were conducted at -0.85 V of LRS and HRS. They presented unchanged values of LRS and HRS over a period of 10^4 s. This is comparable to a recent result which reported an organic-inorganic perovskite memory device with a retention time over 10^4 s, which exhibits a good stability of the device.[79, 81-82, 89, 92]

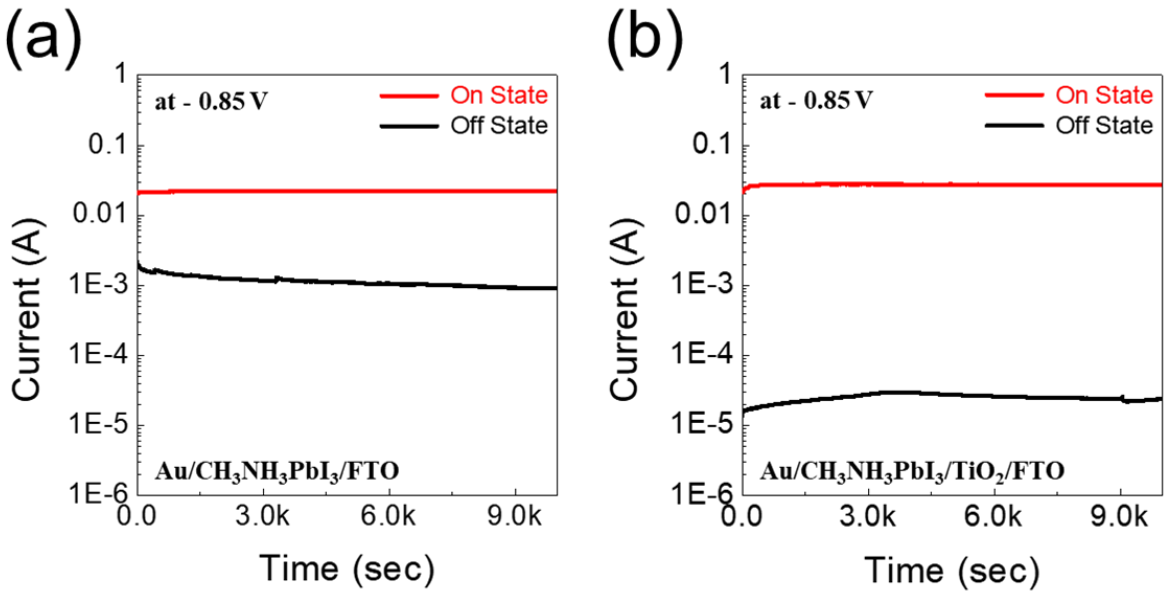

Figure 33 Retention characteristics at LRS and HRS of (a) $Au/CH_3NH_3PbI_3/FTO$ and (b) $Au/CH_3NH_3PbI_3/TiO_2/FTO$ devices[58]

I-V and retention characteristics in Figure 33 suggest that the interface between $CH_3NH_3PbI_3$ and TiO_2 influences on the resistive switching mechanism. As a result, the $Au/CH_3NH_3PbI_3/TiO_2/FTO$ structure exhibits a more asymmetric resistive behavior.

Additional cyclic measurements were performed in Figure 34(a) and 34(b) and both devices showed good endurance stability until 350 subsequent I-V sweeps. The first and the subsequent cycle showed the same V_{SET} and V_{RESET} in both devices without electroforming process as shown in Figure 35.[41] This is because high defects ($V_I^{\cdot}$) and (I_i') concentrations, which are ~5×10^{20} cm^{-3} ($V_I^{\cdot}$) and ~5×10^{16} cm^{-3} (I_i'),[12] in the $CH_3NH_3PbI_3$ layer can form a conductive path at low voltage.

Moreover, 50 devices of $Au/CH_3NH_3PbI_3/FTO$ and $Au/CH_3NH_3PbI_3/TiO_2/FTO$ structure were measured to examine the reproducibility of working cells. Set voltage (V_{SET}) and reset

voltage (V_{RESET}) of these 50 devices are shown in Figure 34(c) and 34(d). The variation of the performance is small. These results indicate that the devices can be potentially utilized in nonvolatile memory applications.

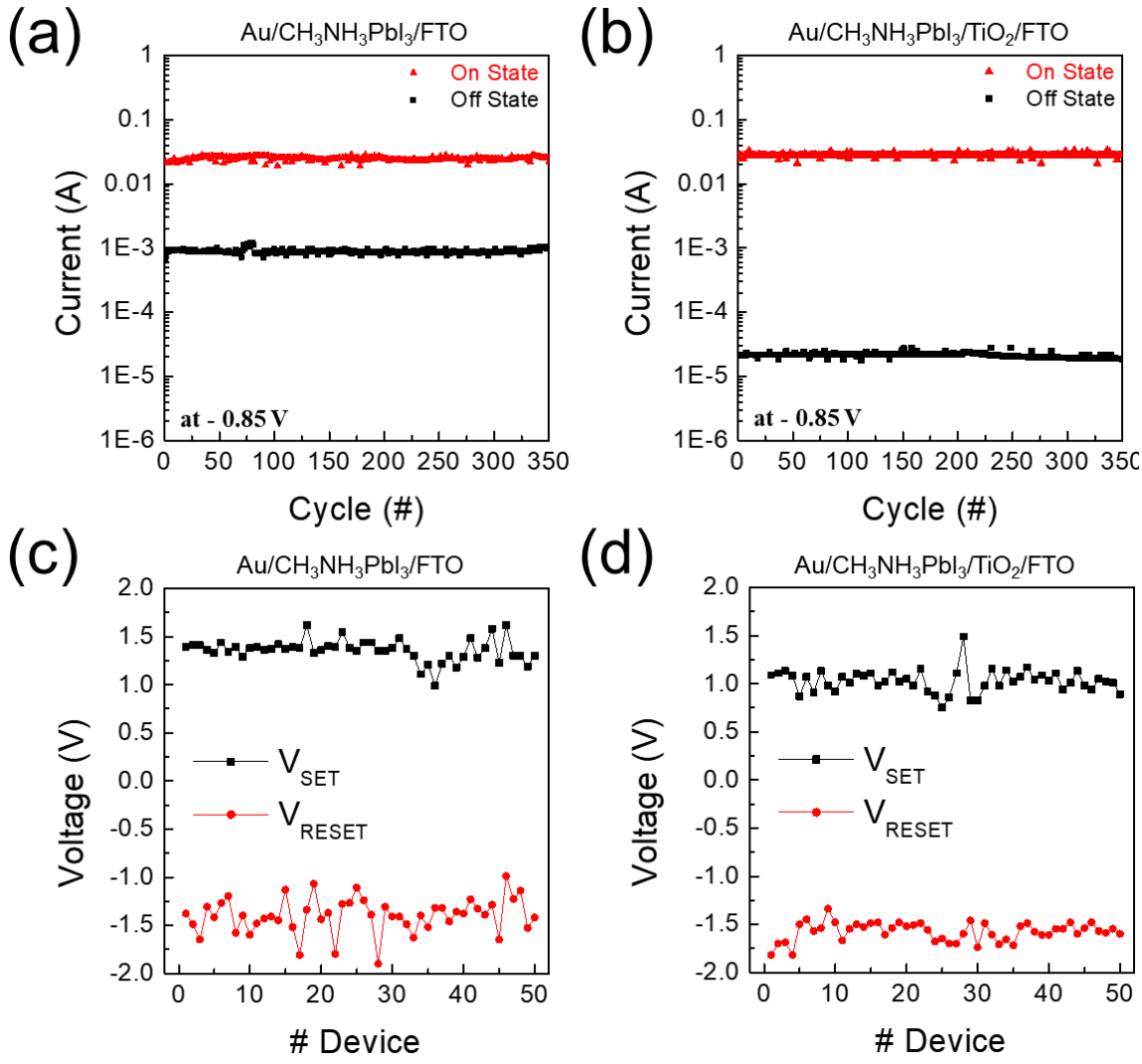

Figure 34 I–V curves of (a) Au/$CH_3NH_3PbI_3$/FTO and (b) Au/$CH_3NH_3PbI_3$/TiO_2/FTO devices through 350 successive cycles. (c) and (d) are their probability distribution for 50 different devices[58]

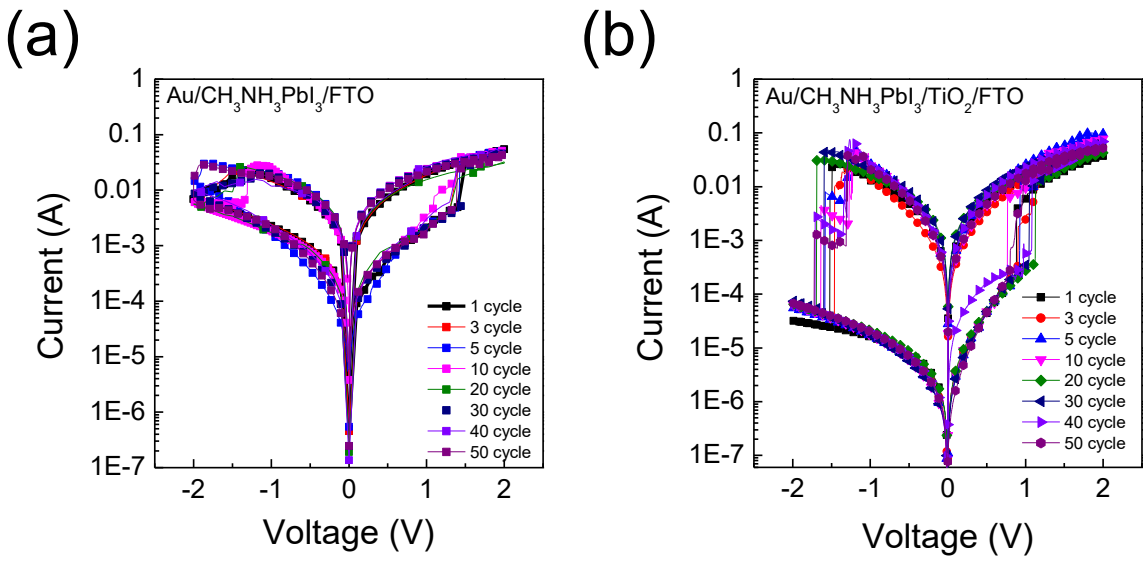

Figure 35 I-V curves of (a) Au/$CH_3NH_3PbI_3$/FTO and (b) Au/$CH_3NH_3PbI_3$/TiO_2/FTO devices through 50 subsequent cycles[58]

3.3.5 I-V Curves under the Same Polarity of both Au/$CH_3NH_3PbI_3$/FTO and Au/$CH_3NH_3PbI_3$/TiO_2/FTO Devices

To further verify the effect of the ion accumulation on the energy barrier at the $CH_3NH_3PbI_3$-TiO_2, $CH_3NH_3PbI_3$-FTO, and $CH_3NH_3PbI_3$-Au interfaces on the electron transport, the unipolar resistive switching behavior is also measured at the compliance current of 100 mA. Figures 36(a) – 36(d) show I-V curves of Au/$CH_3NH_3PbI_3$/FTO and Au/$CH_3NH_3PbI_3$/TiO_2/FTO without flipping the polarity of external bias. Samples were not exposed to electric field before this measurement. When the Au electrode is positively biased, characteristics of I-V curves of Au/$CH_3NH_3PbI_3$/FTO and Au/$CH_3NH_3PbI_3$/TiO_2/FTO are similar, as shown in Figure 36(a) and 36(c). The switching from HRS to LRS occurs only for the first sweep. Once the samples reach the LRS, subsequent unipolar sweep does not make samples return to the HRS. When the Au is

negatively biased, different switching behaviors are observed in Figure 36(b) and 36(d). Au/$CH_3NH_3PbI_3$/FTO switches from the HRS to the LRS during the first voltage sweep and stays in the LRS during subsequent sweeps (Figure 36(b)). However, the application of the negative bias does not change Au/$CH_3NH_3PbI_3$/TiO_2/FTO from the HRS to the LRS (Figure 36(d)). The Au/$CH_3NH_3PbI_3$/TiO_2/FTO maintains the HRS, though it is exposed to multiple unipolar sweeps of the negative bias. In Figure 36(d), it is also noted that the resistance of Au/$CH_3NH_3PbI_3$/TiO_2/FTO in the HRS is much larger than that of Au/$CH_3NH_3PbI_3$/FTO in the HRS. This suggests that the mobile ions (mainly $I_i^{'}$) interact with $CH_3NH_3PbI_3$/TiO_2 and $CH_3NH_3PbI_3$/FTO very differently when the negative bias is applied to the Au electrode. Due to the migration of $V_O^{\cdot\cdot}$ in TiO_2 under electric field, Schottky junction barrier of $I_i^{'}$ can be formed at $CH_3NH_3PbI_3$/ TiO_2 interface, as schematically explained in Figure 36(e).[48] The accumulated charge layer suppresses the electron transport from $CH_3NH_3PbI_3$ to TiO_2 charges transport and prevents the formation of the conductive V_I channels.

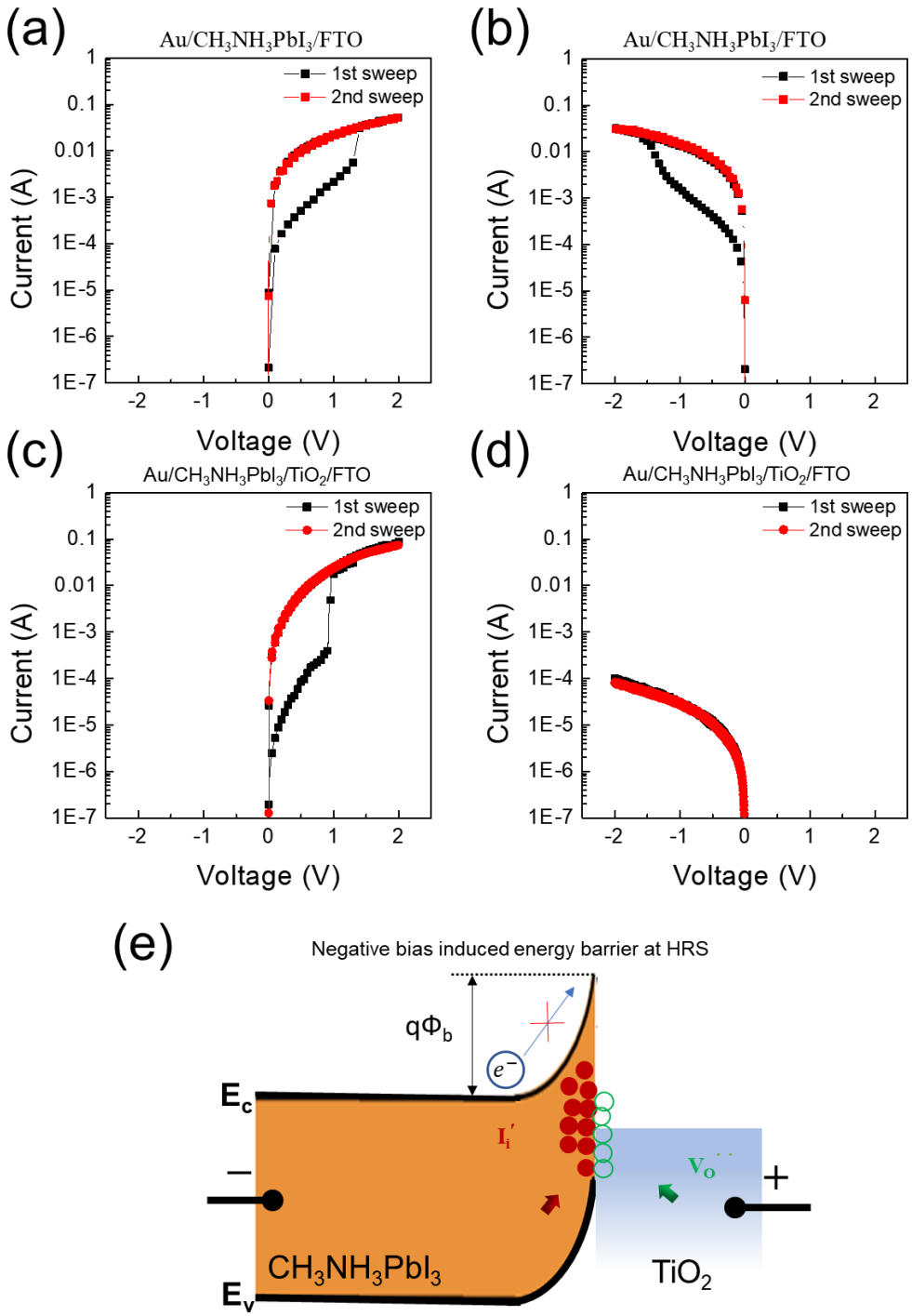

Figure 36 (a), (b) unipolar I–V curves of Au/$CH_3NH_3PbI_3$/FTO ((a) positive bias is applied to Au, (b) negative bias is applied to Au); (c), (d) unipolar I–V curves of Au/$CH_3NH_3PbI_3$/TiO_2/FTO ((c) positive bias is applied to Au, (d) negative bias is applied to Au); (e) a schematic on the band bending at the $CH_3NH_3PbI_3$/TiO_2 interface under negative bias applied to Au[58]

Additional evidence to support that Schottky junction at the interface is modified by addition of TiO_2 is provided by inserting the phenly-61C-butyric acid methyl ester (PCBM) layer between the perovskite and FTO layers. TiO_2 and PCBM have a similar function to passivate the surface of the perovskite layer. However, while the dielectric TiO_2 layer holds charged defects on the surface under E-field, the conductive PCBM layer does not provide any additional charge storage function. Figure 37 shows no resistive switching behavior of the Au/ $CH_3NH_3PbI_3$/PCBM/FTO device. This result indicates that a strong electrostatic attraction between negatively charged I_i' and positively charge $V_O^{\cdot\cdot}$ under DC bias at the $CH_3NH_3PbI_3/TiO_2$ interface contributes to a unique switching behavior of Au/perovskite/TiO_2/FTO device.

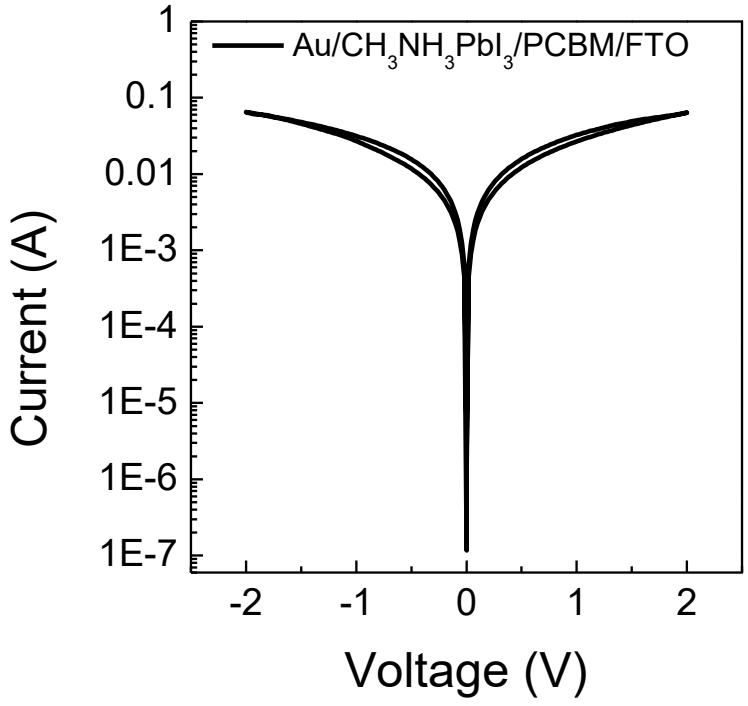

Figure 37 I-V curve of Au/$CH_3NH_3PbI_3$/PCBM/FTO[58]

3.3.6 Space Charge Polarization of both Au/$CH_3NH_3PbI_3$/FTO and Au/$CH_3NH_3PbI_3$/TiO_2/FTO Devices

The space charge at the $CH_3NH_3PbI_3$-TiO_2 interface was examined by measuring the capacitance of the films as a function of the frequency. During the measurement, the external DC bias ranging from -1.5V to 1.5V was also applied. Figure 38 shows the capacitance-frequency (C-f) curves of Au/$CH_3NH_3PbI_3$/FTO and Au/$CH_3NH_3PbI_3$/TiO_2/FTO. Large capacitance at the frequency below 10^3 Hz is due to space charge polarizations resulting from the charge imbalance at different interfaces, while the electronic and ionic polarization mechanism is responsible for the capacitance at high frequency.[84]

In Figures 38(a) and 38(b), C-f curves of Au/$CH_3NH_3PbI_3$/FTO under different positive and negative bias are similar. This suggests that Au - $CH_3NH_3PbI_3$ interface and $CH_3NH_3PbI_3$ - FTO interface contribute similarly to the space charge polarization. However, C-f curves of Au/$CH_3NH_3PbI_3$/TiO_2/FTO in Figures 38(c) and 38(d) exhibit the significant effect of external bias on the capacitance. This indicates that the TiO_2 layer increases the space charge polarization and the effect of TiO_2 on the capacitance has the polarity. When the negative bias is applied to Au, an increase in the absolute bias increases the capacitance. The accumulation of the negatively charged iodine interstitials at the $CH_3NH_3PbI_3$ - TiO_2 interface dramatically increases the space charge polarization. This is attributed to the migration of $V_O^{\cdot\cdot}$ in TiO_2 under DC bias.[49] Larger negative bias applied to Au increases more migration of $V_O^{\cdot\cdot}$ to the TiO_2-$CH_3NH_3PbI_3$ interface and hold more I_i' by the electrostatic attraction. The accumulated I_i' increases the space charge polarization of the film. The C-V curves support that the electrostatic force causes the accumulation of I_i' at the $CH_3NH_3PbI_3$ - TiO_2 interface if the negative bias (or positive bias) is

applied to Au (or FTO) rather than forming the defect chain. These accumulated defects which work as Schottky barrier shows why the resistance of the Au/$CH_3NH_3PbI_3$/TiO_2/FTO at HRS has the dependence on the direction of the external electric field.

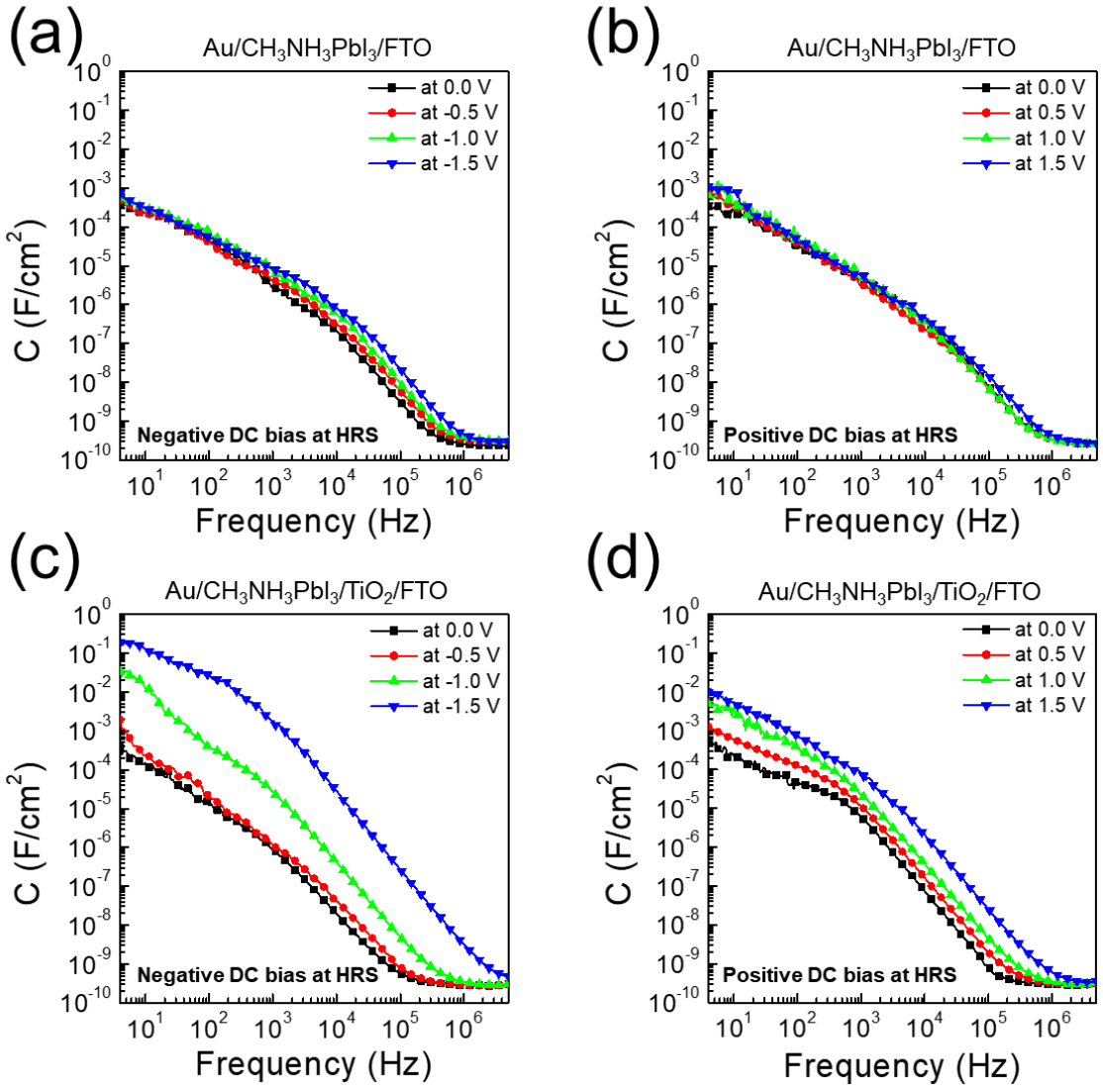

Figure 38 Capacitance-frequency (C-f) curves of Au/$CH_3NH_3PbI_3$/FTO [(a) the negative DC bias to Au, (b) the positive DC bias to Au] and Au/$CH_3NH_3PbI_3$/TiO_2/FTO [(c) the negative DC bias to Au, (d) the positive DC bias to Au] [58]

3.4 Conclusion

TiO_2 interface asymmetrically influences the resistive switching of the $Au/CH_3NH_3PbI_3/TiO_2/FTO$ device by changing the formation and rupture of defect chains. When a negative bias is applied to the Au electrode, iodine interstitials with the lowest migration energy move in $CH_3NH_3PbI_3$ toward TiO_2 and pile up at the $CH_3NH_3PbI_3{-}TiO_2$ interface. Under the same condition, oxygen vacancies in TiO_2 layer also travel to the $CH_3NH_3PbI_3{-}TiO_2$ interface, strongly attract iodine interstitials, and form a Schottky barrier at the $CH_3NH_3PbI_3{-}TiO_2$ interface. Consequently, the modified Schottky junction barrier of the $Au/CH_3NH_3PbI_3/TiO_2/FTO$ device reduces the electric current at HRS when a negative electric bias is applied to Au. This leads to the higher on/off ratio, 10^3, and good retention time, greater than 10^4 seconds during the resistive switching. Our study shows that the interface in contact with the halide perovskite layer can control the appearance of the conductive chains and the bipolar resistive switching behavior in the halide perovskite film.

4.0 Improved Long-term Stability of PSCs by Polymer Nanocomposites

4.1 Background and Motivation

Organic-inorganic halide perovskite solar cells (PSCs) have attracted intensive attention as an alternate candidate to energy devices due to the fast improvement in power conversion efficiency (PCE). Over the past years, the certified PCE has achieved up from 3.8% to 25.2%, which is higher than that of the other emerging solar cells.[6, 69] Although PSCs have additional strengths such as high efficiency, simple fabrication, and low material cost,[21, 67-68] there are still few obstacles to overcome current density-voltage hysteresis, instability of perovskite under solar radiation, and perovskite dissociation in humid environment for commercialization.[23, 96-98] Especially, planar normal PSCs consisting of TiO_2 as ETL and Spiro-OMeTAD as HTL exhibit large hysteresis, photocatalytic dissociation, and instability of additives.[23-25] Stable oxide electron and hole conductors such as ZnO as ETL and NiO as HTL are employed to address these problems by replacing TiO_2 and Spiro-OMeTAD due to photocatalytic effect of TiO_2 and thermal instability of Sipro.[24] Recently, as for the degradation of the perovskite under UV light, down-conversion of UV light with phosphors has been widely utilized to improve stability under solar irradiation and PCE of PSCs.[5] It has also provided an additional photon energy to the PSCs by converting UV light to visible light in UV region.[8]

The long-term stability of PSCs is quite challenging. Particularly, the PSCs are gradually degraded when they are exposed to extreme environment such as high humidity.[7] Lead halide perovskite material ($CH_3NH_3PbI_3$) is decomposed into PbI_2 and other byproducts by contacting

with water molecules. Various methods from the other groups are reported to improve stability of PSCs such as tuning structure of perovskite, adding additives, and coating encapsulation layer on PSC device.[99-101] New organic-inorganic compositions such as $FAPbI_3$, $MAPbI_{3-x}(SCN)_x$, $(PEA)_2(MA)_{n-1}Pb_nI_{3n+1}$, $RbPbI_3$, and so on showed the improved stability due to the more stable structure than pure $MAPbI_3$.[101-103]

By adding additives such as polymer, inorganic acid, organic materials etc., improvement in the stability of perovskite device was obtained. Additives enabled the improvement of perovskite film morphology with large grain boundaries.[99] Encapsulation is the one of the most common ways to improve stability of the commercial solar cells such as silicon solar cells and CIGS.[104-105] Epoxy resin and glass were used to encapsulate the PSC devices and protect from penetration of water molecules, resulting in improvement of the long-term stability.[105-106]

Polymer, which is interesting material to be used in many industrial and biomedical domains,[107] has also provided sealing technique to effectively lower or delay the water vapor permeation in the area of OLED.[108] Encapsulated PSCs with hydrophobic polymer, which is Teflon, showed prolonged lifetime of the PSCs.[109] Also, ultra-hydrophobic encapsulation polymer consisting of hydrophilic inorganic nanoparticles such as SiO_2 and hydrophobic polymer matrix reduced water contact at the surface, resulting in suppressed degradation of perovskite film.[7]

In this study, a simple and effective passivation method using polymers was introduced to encapsulate the PSCs. Interpenetrating polymer networks (IPNs) by mixing partial PMMA and partial PU were fabricated to suppress swelling of individual polymer and improve mechanical resistance to moisture due to physical interlocking and inter-network interaction.[110, 111] Moreover, by addition of nanoparticles such as SiO_2,[112] surface property of the IPNs was

changed to have hydrophobicity to decrease water molecule attachment and prevent degradation of the photovoltaic performance of the PSC. By addition of CeO_2,[113] hydrophilicity was formed in the IPNs to trap penetrated water molecules in the layer and procrastinate water molecule diffusion toward perovskite layer. The nanoparticles in the polymer matrix also made a twisted path for the permeating water molecule. The diffusion path and penetration time of water vapor are increased. As a result, the encapsulated inverted PSC dramatically exhibits suppressed degradation process under damp heat test (DH test, 85/85 ℃/RH(relative humidity).

4.2 Experimental Section

4.2.1 Preparation of PMMA-PU IPN Nanocomposites Film

IPNs were made by mixing pre-polymerized PU and pre-polymerized PMMA in weight percent % ratios of 25/75, 50/50, and 75/25 (PMMA/PU). The PU was synthesized by combining PTMG (Poly(tetramethylene ether)glycol), TRIOL (compounds: 2- ethyl-2-(hydroxymethyl)-1,3-propanediol), and DCH (Hexamethylene diisocyanate) in a ratio of PTMG:TRIOL (4.85:1 wt.%), and PTMG/TRIOL:DCH (1.8571:1 wt.%) at 70 ℃ for 45 mins with vigorous stirring (500 rpm). The PMMA was made by combining MMA (Methyl methacrylate) with a 1 wt.% of AIBN (Azobisisobutyronitrile) and TRIM (Trimethylolpropane trimethacrylate) as a cross linker was then added using ratio MMA:TRIM (95:5 wt.%). This mixture was stirred at 60 ℃ for 90 minutes with the same stirring. For the IPNs nanocomposite, nanoparticles such as SiO_2 and CeO_2 as a function of vol% were added into MMA solution with a 1 wt % of AIBN. After PMMA was pre-polymerized, the solution was mixed with pre-polymerized PU in Figure 39.

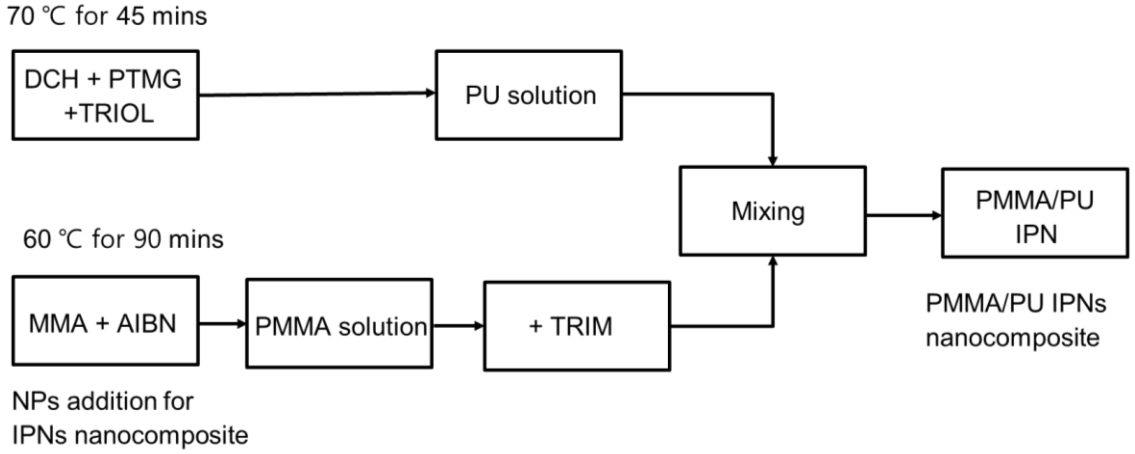

Figure 39 Synthesis of PMMA/PU IPN and PMMA/PU IPN nanocomposite

4.2.2 Fabrication of Encapsulated PSCs

Inverted PSCs with a structure of Ag/BCP/PCMB/$CH_3NH_3PbI_3$/NiO/FTO were fabricated by the following sequence. FTO coated glasses were partially etched by using zinc powder and hydrochloric acid (2 M) and then cleaned in acetone, de-ionized water, and ethanol. Ni film was deposited onto the FTO coated glasses by e-beam evaporator. And then, Ni/FTO was oxidized at 550 ℃ in air ambient to form NiO film as HTL. Methyl ammonium iodide (MAI, CH_3NH_3I), lead iodide (PbI_2), and dimethyl sulfoxide (DMSO) with a molar ratio of 1:1:1 was dissolved to make the $CH_3NH_3PbI_3$ solution. This $CH_3NH_3PbI_3$ solution was spin-coated on top of the NiO/FTO at 4000 rpm for 25 s. During the spin-coating, 0.5 mL of diethyl ether was slowly dropped. The samples were annealed at 60 °C, and then at 100 °C for 3 and 10 min, respectively. PCBM (20 mg) dissolved in dichlorobenzene (1 mL) solution was spin-coated at 2,000 rpm for 60 s and BCP (5 mg) in ethanol (10 mL) was deposited by spin-coating at 4,000 rpm for 40 s in sequence. Finally, an 80-nm-thick Ag was deposited by thermal evaporation with a shadow mask. Each encapsulation was coated on the PSCs.

4.2.3 Characterization

The photovoltaic performances of the PSCs were obtained by using an electrochemical workstation (CHI660, CHI Instrument). AM 1.5 G condition was calibrated with a reference Si solar cell (PVM 95). As a light source, A solar simulator (Oriel Sol 3A class AAA, Newport) was utilized. The effective area of the PSCs was defined as 0.14 cm^2 using a non-reflective metal mask.

4.3 Results and Discussion

Figure 40 shows the schematic of the encapsulation layers for the inverted PSC, which is composed with Ag/BCP/PCMB/$CH_3NH_3PbI_3$/NiO/FTO. Since the normal n-i-p PSC contains Li+ doped spiro-OMeTAD as HTL, the dopant can be evaporated at 85 ℃, resulting in thermal instability of the PSC due to the heat accumulation during DH test. Thus, the inverted p-i-n PSC, which is thermally stable at 85 °C, was selected for the long-term stability test. The encapsulation layers, which have two functions, was applied to the PSC device. The top layer, which is hydrophobic layer, can decrease water molecular attachment. The bottom hydrophilic layer can capture the penetrated water molecules. The combination of two layers can improve the stability of the PSC device under DH test by lowering a water permeation rate and making a twisted path for the permeating water molecule.

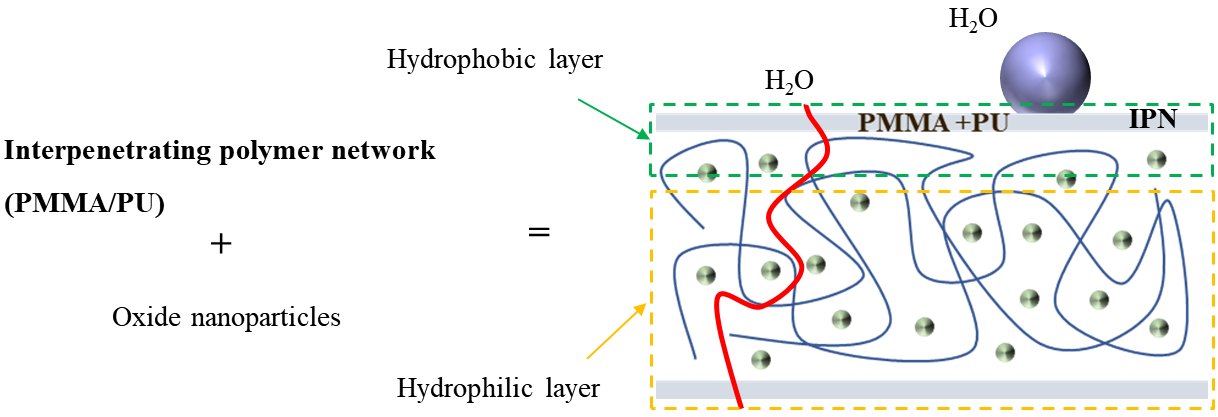

Figure 40 Scematic of the encpasulation for the PSC

4.3.1 Interpenetrating Polymer Network (IPN) with Methacrylate-based Polymer and Polyurethane

Figure 41 shows the FTIR spectrum of PMMA at a wavelength rang of 4000 – 600 cm^{-1}. The spectrum exhibits several functional groups of PMMA such as a-methyl, ester-methyl, and methylene C-H stretching (3100–2800 cm^{-1}) and bending (1500–1350 cm^{-1}) modes. A sharp intense peak at 1743 cm^{-1} appears due to the presence of ester carbonyl group stretching vibration. The absorption peaks from 1161 cm^{-1} to 1270 cm^{-1} are attributed to the C–O–C stretching vibration mode. The band at 1743 cm^{-1} and 984 cm^{-1} corresponds to the acrylate carboxyl group and the methylene rocking mode, respectively. All peaks confirm that MMA monomers are fully converted to PMMA with the aid of the AIBN initiator.[16]

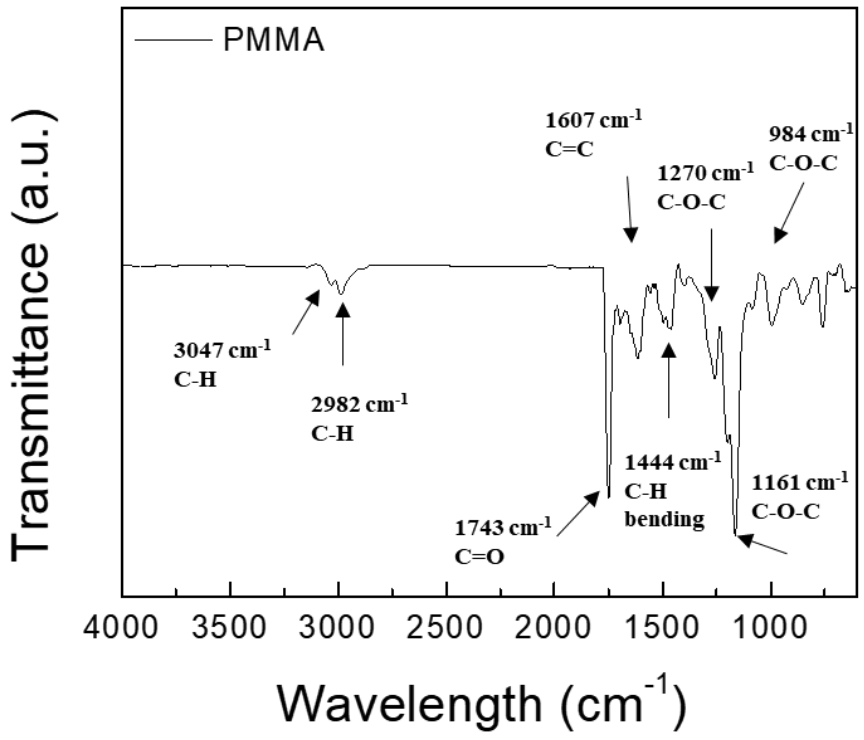

Figure 41 FTIR spectrum of the synthesized PMMA

FT-IR result in Figure 42 reveals that synthesized PU has six major peaks. The band at 3380 cm^{-1} is assigned as the -NH stretching vibration peak. C=O (amide I band) and -NH (amide II band) peaks appear near 1727 cm^{-1} and 1557 cm^{-1}. The bands at 1261 cm^{-1} and 1111 cm^{-1} correspond to the C-O stretching vibration mode, respectively. Isocyanate, which is the functional group (NCO), is not observed at 2240–2275 cm^{-1}, which attests the complete conversion of NCO to PU.[114]

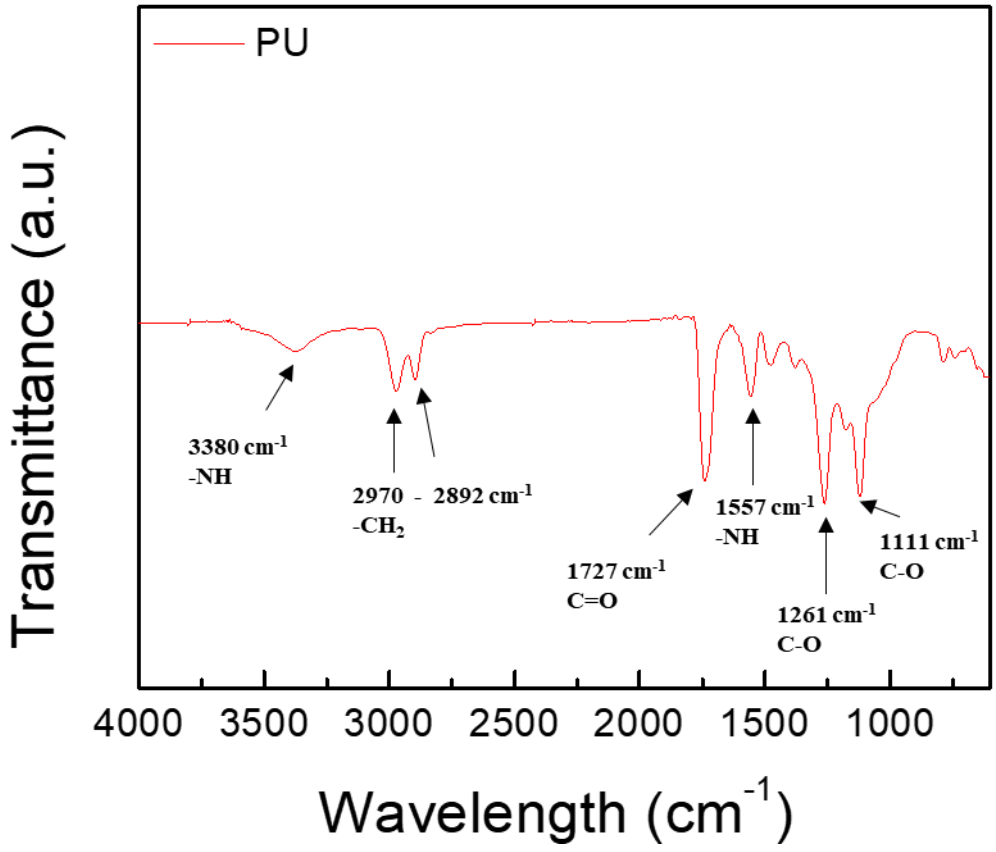

Figure 42 FTIR spectrum of synthersized PU

As shown in Figure 43, all IPNs with the different weight percent ratios (PMMA/PU) exhibit the characteristic absorption peaks in the region of 3600 to 3100 cm^{-1}, which corresponds

to -NH stretching.[115] As the amount of PMMA increases, the absorption peak of a -NH stretching decreases in Figure 43(b). This is because the MMA component, which has C=O groups, forms the hydrogen bonding with -NH group of IPN and decreases the intensity of -NH group. The peak intensity of -NH group at 1557 cm^{-1} concurrently decreases. Addition of PMMA to the IPN structure increases the C=O peak at 1743 cm^{-1}. As shown in Figure 43(c), the peak of the hydrogen bonded with C=O group shifted between 1740 and 1750 cm^{-1} and intensity of the peak increased due to the increased free-hydrogen bonded of C=O group from MMA component. Since the amount of PMMA increased in Figure 43(d), the band intensity at 1161 cm^{-1}, which is related to C-O-C stretching vibration, increased.

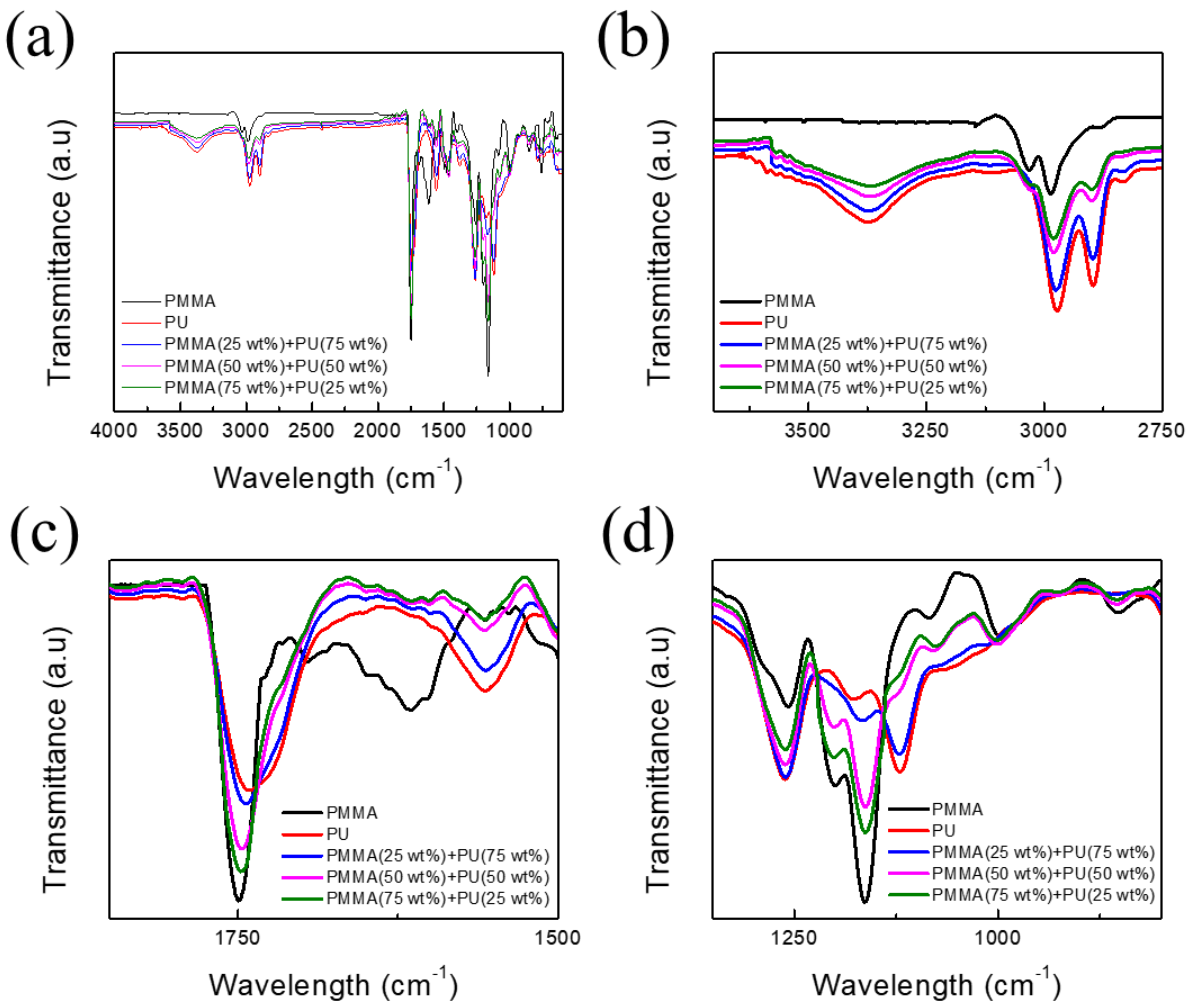

Figure 43 FTIR sprectrum of (a) PMMA-PU IPN and detailed spectrum in the range of (b) 3700 to 2750 cm^{-1}, (c) 1850 to 1500 cm^{-1}, and (d) 1350 to 800 cm^{-1}

The loading-unloading curves of the samples were measured by using nanoindentation in Figure 44. The depth of indentation decreased, indicating that the hardness increased. Concurrently, the curves were shifted to the left, representing that the hardness increased. IPNs have better mechanical resistance due to physical and interpenetrated reaction compared to individual polymer network. As the PMMA content was decreased in IPNs, the hardness was decreased from 132 MPa of PMMA to 23 MPa of PMMA/PU (25/75 wt%) in Table 4. The PU

hardness of 3.4 MPa was observed due to the flexible property of PU. The IPNs can prevent swelling film induced by water due to the formation of hydrated PMMA.[6] Hydrolysis of ester groups in PMMA create extended defects and growth of cracks under humid environment.[6] By creating interpenetrating polymer networks, IPNs suppresses interfacial slip caused by the swelling of PMMA.[110-111]

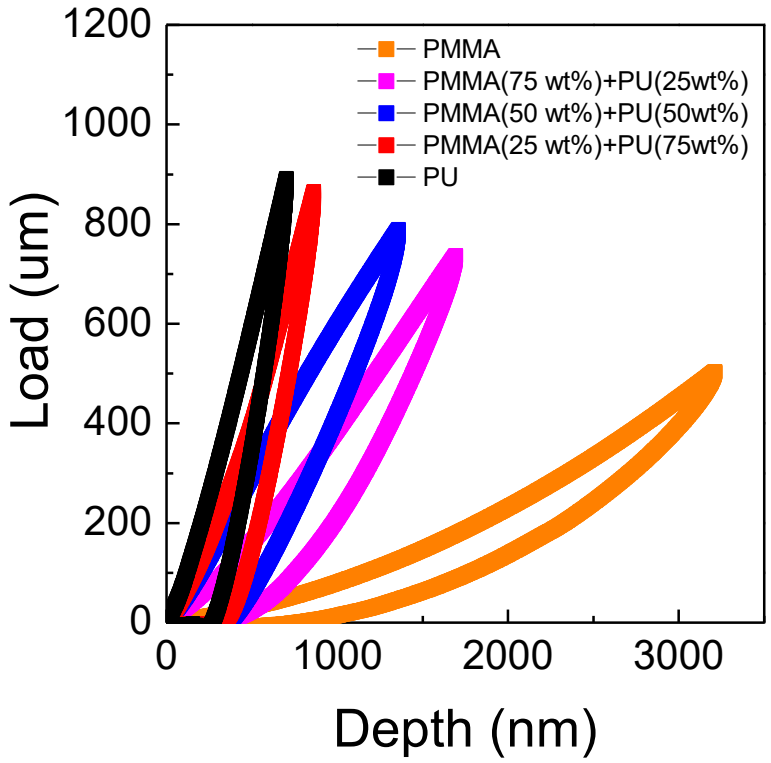

Figure 44 Load-displacement curves of the nanoindentation analysis for PMMA, PU, and all IPNs

Table 4 Hardness of the samples, PMMA, PMMA/PU (75/25 wt%), PMMA/PU (50/50 wt%), PMMA/PU (25/75 wt%), and PU

	Hardness (Mpa)
PMMA	132
PMMA/PU (75/25 wt%)	84
PMMA/PU (50/50 wt%)	45
PMMA/PU (25/75 wt%)	23
PU	4

Water diffusion coefficient of each film in water at 85 ℃ was calculated by an accelerated degradation test in Figure 45 by using the following equation:

$$L = \sqrt{Dt} \tag{4.1}$$

Where L is film thickness, D is diffusion coefficient (cm^2/s), and t is time (sec). The individual layer encapsulated on perovskite/glass substrate was dipped into water at 85 ℃. The degradation of perovskite ($CH_3NH_3PbI_3$) is attributed to the dissociation of the perovskite phase when it exposed to water, which can be expressed by a series of the following chemical equitation previously reported:[6]

$$CH_3NH_3PbI_3(solid) + H_2O \leftrightarrow CH_3NH_3PbI(aqueous) + PbI_2$$

$$CH_3NH_3PbI(aqueous) \leftrightarrow CH_3NH_2(aqueous) + HI(aqueous)$$

$$4HI(aqueous) \leftrightarrow 2I_2(solid) + 2H_2O(liquid)$$

These equations can easily and generally explain that the perovskite (bandgap: ~1.5 eV) phase is decomposed into PbI_2 (bandgap: ~2.3 eV) by observing the change of perovskite color from dark to yellow. The calculated water diffusion coefficient was obtained through the time taken to change the color of the perovskite.

PMMA exhibited the highest water diffusion coefficient due to the swelling behavior caused by hydrolysis of the ester group in PMMA. Due to the water absorption property of thermoplastic PU. The film has also higher water diffusion coefficient. The formation of IPNs can suppress hydrolysis phenomenon because interpenetrated and cross-linked polymers block interfacial slip, decreasing water diffusion in the layer. The IPNs with 50/50 wt % ration of PMMA to PU has the lowest water diffusion coefficient at 85 ℃.

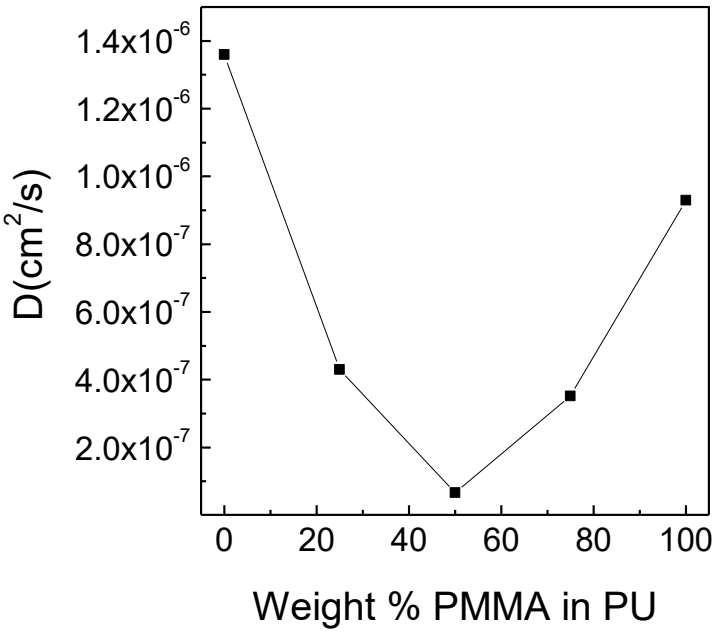

Figure 45 Calculated water diffusion coefficient in PMMA, PU, and IPNs with different weight % ratio (PMMA/PU wt%) at 85 ℃

4.3.2 Nanocomposites by Addition of Nano Particles

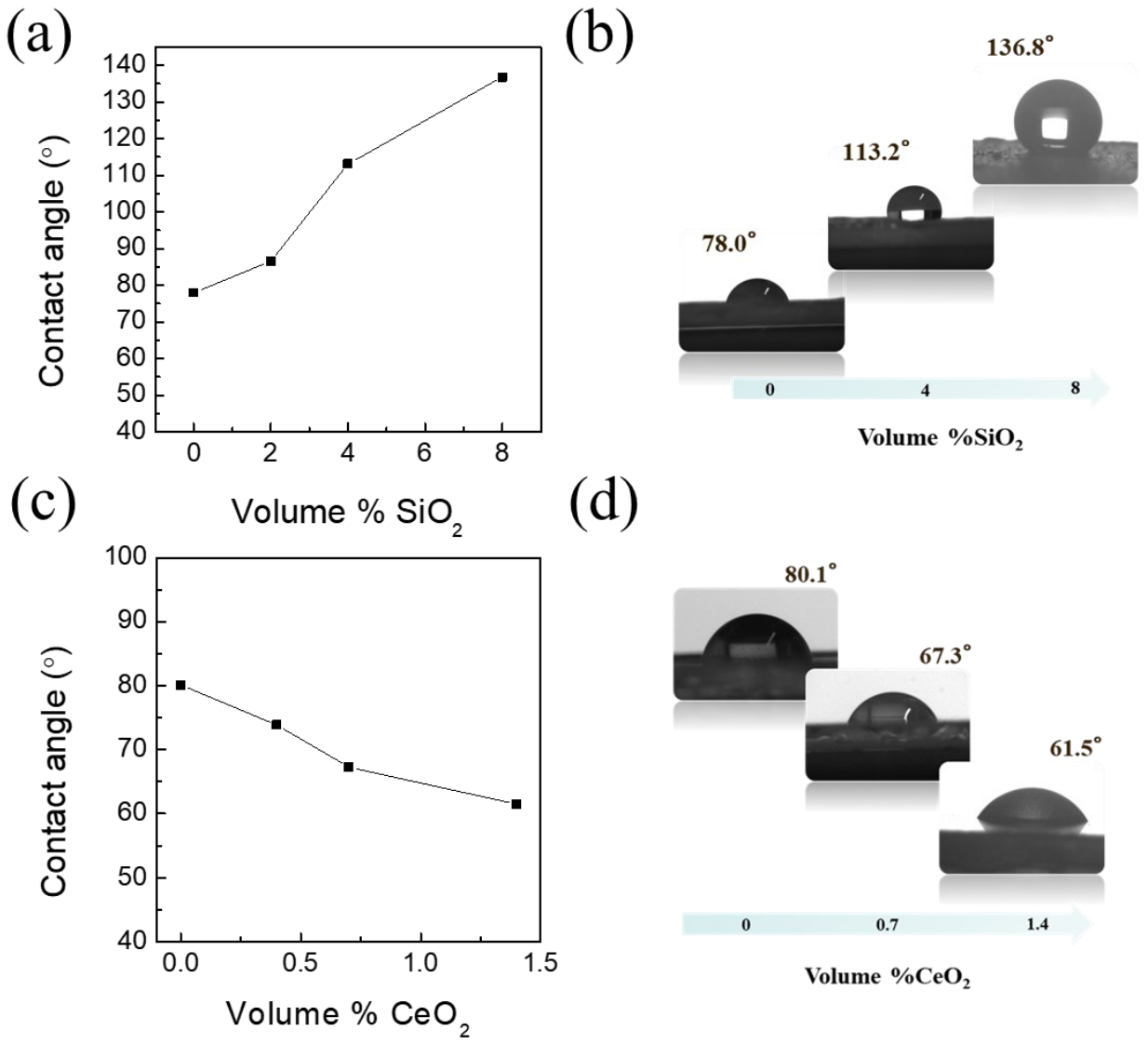

Figure 46 A change of contact angle of PMMA-PU nanocomposite encapsulation layer as function of volume % SiO_2 and CeO_2

Figure 46(a) and (c) shows that the contact angle changes of IPNs (PMMA/PU -50/50 wt %) depending on the different oxide material such as SiO_2 and CeO_2. Uniformly distributed nanoparticles were occupied in free volume between polymer chains, providing low water

permeation of the polymer. In the other hand, common dioxides such as SiO_2 are hydrophilic to form hydrogen bond with ester groups in PMMA which rotate toward the oxide nanoparticles due to van der Waals interactions. As a result, hydrophilicity of PMMA was significantly reduced in Figure 46(a). The contact angle of the film was increased from 78 ° to 136 °. However, as the SiO_2 volume % is increased, the SiO_2 nanoparticles were not uniformly distributed in the polymerization process due to the formation of hydrogen bonding with ester group through van der Waals interactions.[116] This leads to agglomeration of nanoparticles and rough surface in the polymer, causing negative effects on prevention from water penetration. On the other hand, contact angle of the films was decreased from 80.1 ° without CeO_2 nanoparticles to 61.5 ° in Figure 46(c) as an increase of CeO_2 volume in PMMA-PU IPN. Rare-earth oxides such as CeO_2 have a unique electronic structure. The unfilled 4f orbitals are not interacted with the surrounding environment due to shielding effect causing by the full filled $5s^2p^6$ outer shell. This disturbs to form the hydrogen bond next to the surface.[112-113] When hydrophobic CeO_2 nanoparticles were mixed with PMMA, reorientation of polymer occurred that ester groups are exposed to the surface to form hydrogen bond of water molecules, resulting in decrease of contact angle. However, CeO_2 nanoparticles were also well-distributed between polymer chains without agglomeration while they also suppressed to form long chain of polymer due to repellent between nanoparticles and ester group. Uniformly distributed nanoparticles were occupied in free volume between polymer chains, providing low water permeation of the polymer.

4.3.3 Water Penetration Testing

Figure 47(a) shows that considerable time-dependent color change of the perovskite film coated with encapsulation layer in water at 85 ℃ was visually observed as function of volume % of CeO_2 in PMMA/PU (50/50 wt%). In the acceleration degradation test by dipping perovskite film in water at 85 ℃, the color of perovskite film coated with PMMA/PU (50/50 wt%) IPN containing 0.4 vol% and 0.7 vol% of CeO_2 was changed from dark to yellow after 35 min and 42 min respectively. PMMA-PU IPNs/CeO_2 (1.4 vol%) coated on perovskite remained intact for 50 min during the acceleration degradation test in water at 85 ℃. Improved stability of PSC coated with PMMA/PU (50/50 wt%) IPNs/CeO_2 (1.4 vol%) is proved by the light observation spectrum as shown in Figure 47(c), exhibiting no absorbance change of the perovskite film for 50 min at 85 ℃. Water diffusion coefficient of the encapsulation layers was calculated based on the result of perovskite color change after the acceleration degradation test in shown in Figure 47(b). The thickness (110 μm) of the encapsulation layers coated on perovskite film were the same. As the volume % of CeO_2 in PMMA/PU (50/50 wt%) is increased to 1.4 vol %, water diffusion coefficient is decreased from 8.06×10 cm^2/s containing no CeO_2 nanoparticles in PMMA/PU (50/50 wt%) IPNs to 4.03×10 cm^2/s with 1.4 vol% of CeO_2.[117] These results are comparable to the recent results which reported a water sorption characteristic of polymer such as solid epoxy.

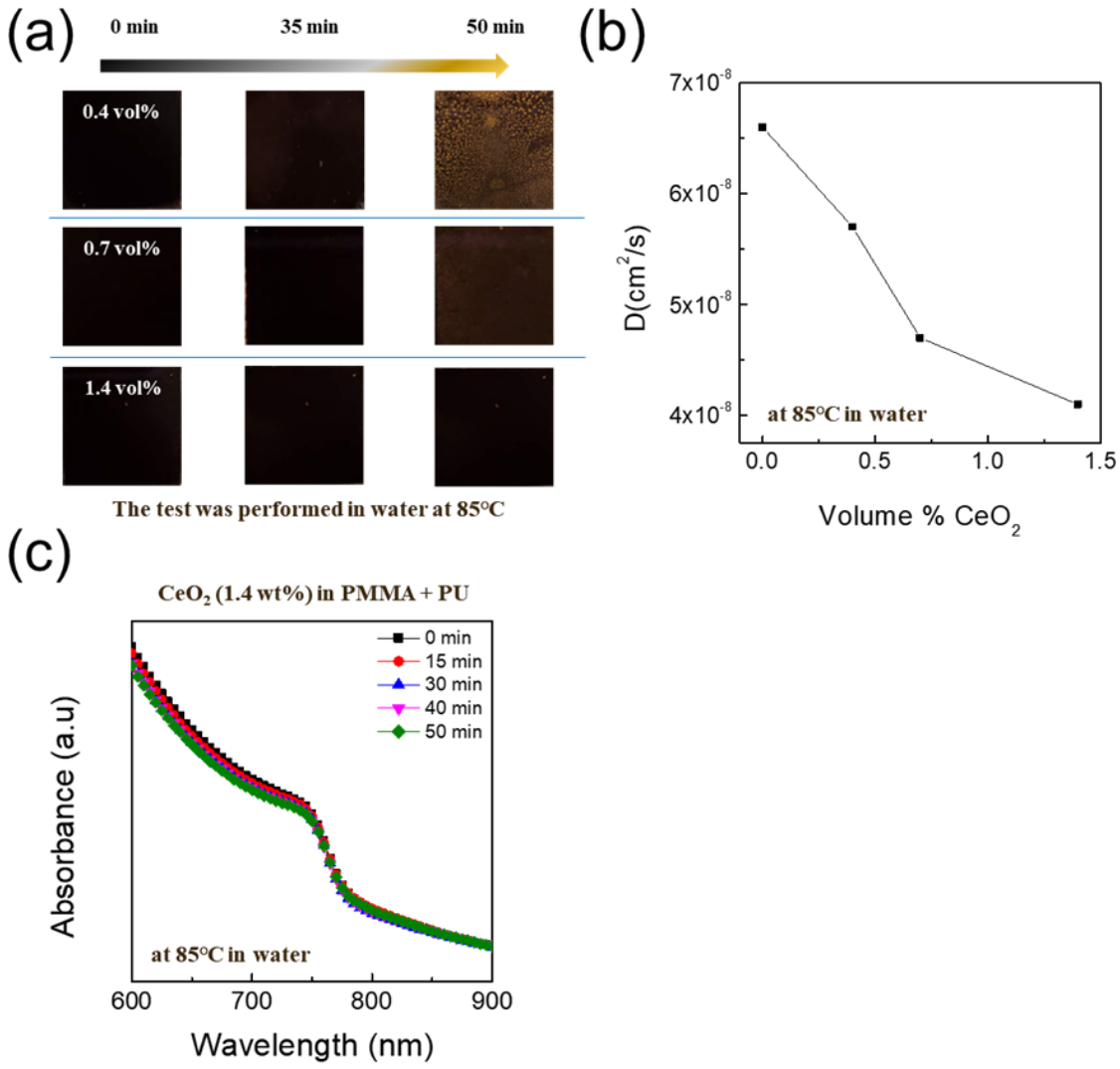

Figure 47 (a) Digital photograph of pristine perovskite film with PMMA/PU (50/50 wt%) IPNs/CeO_2(0.4, 0.7, and 1.4 vol%), as prepared and after immersion in water at 85 °C for 35 and 50 min. (b) water diffusion coefficient calculated in PMMA/PU (50/50 wt%) IPNs/CeO_2(0.4, 0.7, and 1.4 vol%) at 85 °C. (c) Light absorption spectrum of perovskite film with PMMA/PU (50/50 wt%) IPNs/CeO_2(0.4, 0.7, and 1.4 vol%) as function of time after immersion in water 85 °C

4.3.4 Long-Term Stability Test of the Encapsulated PSC

Figure 48(a) exhibited no detrimental effects on photovoltaic performances after coating encapsulation on the PSC. Negligible changes in the photovoltaic parameters of J_{sc}, V_{oc}, and FF were confirmed. Before the encapsulation layers coating, bare PSC had a J_{sc} of 23.5 mA/cm^2, V_{oc} of 0.99 V, FF of 0.67, and PCE of 15.7 %. After the encapsulation layers coating, the photovoltaic parameters of the PSC were a J_{sc} of 23.0 mA/cm^2, V_{oc} of 0.99 V, and FF of 0.68. and PCE of 15.5 %, respectively. The efficiency PSC with the encapsulation remained within 98.7% of the PCE from the bare PSC.

An acceleration test of the PSC coated with the encapsulation layers was conducted at 85/85 ℃/RH condition, showing J-V curves in Figure 48 (b). Time-dependent change of the PCE was recorded in a certain time interval, 48 h, 96 h, 192 h, 382 h, 576 h, 768 h, and 840 h in sequence. At the beginning of the acceleration test at 85/85 ℃/RH, 4 % of the initial current density and 3.4 % of the initial FF were decreased while having the similar voltage of the 192-h aged PSC. This is because $CH_3NH_3PbI_3$ and PbI_2 coexisted in the perovskite layer, causing negative effects on photovoltaic performance such as recombination centers of electron-hole pairs and space charges accumulation by increasing defects. As a result, series resistance of the device was increased due to defects in the perovskite layer, resulting in decrease of FF firstly. Concurrently, less light absorption due to the decomposed perovskite, current density was decreased. After 192 h, more dissociation of perovskite film occurred by infiltrating moisture. Current density and FF were gradually decreased from 24.20 of J_{sc} and 0.62 of FF to 21.40 of J_{sc} and 0.57 of FF until 816 h. As the degradation of the PSC under DH test was accelerated, the amount of light absorbed in the perovskite layer was decreased, lowering current density of the device. This was proved by the time-dependent absorbance spectrum of the PSC coated with the

encapsulation layers in Figure 49. After 816 h, PCE remained 84.0 % of the initial efficiency, showing the improved long-term stability of the PSC coated with the encapsulation layers which have a top PMMA/PU (50/50 wt%) IPN/SiO_2 (8.0 vol%) layer and a bottom PMMA/PU (50/50 wt%) IPN/CeO_2 (1.4 vol%) layer.

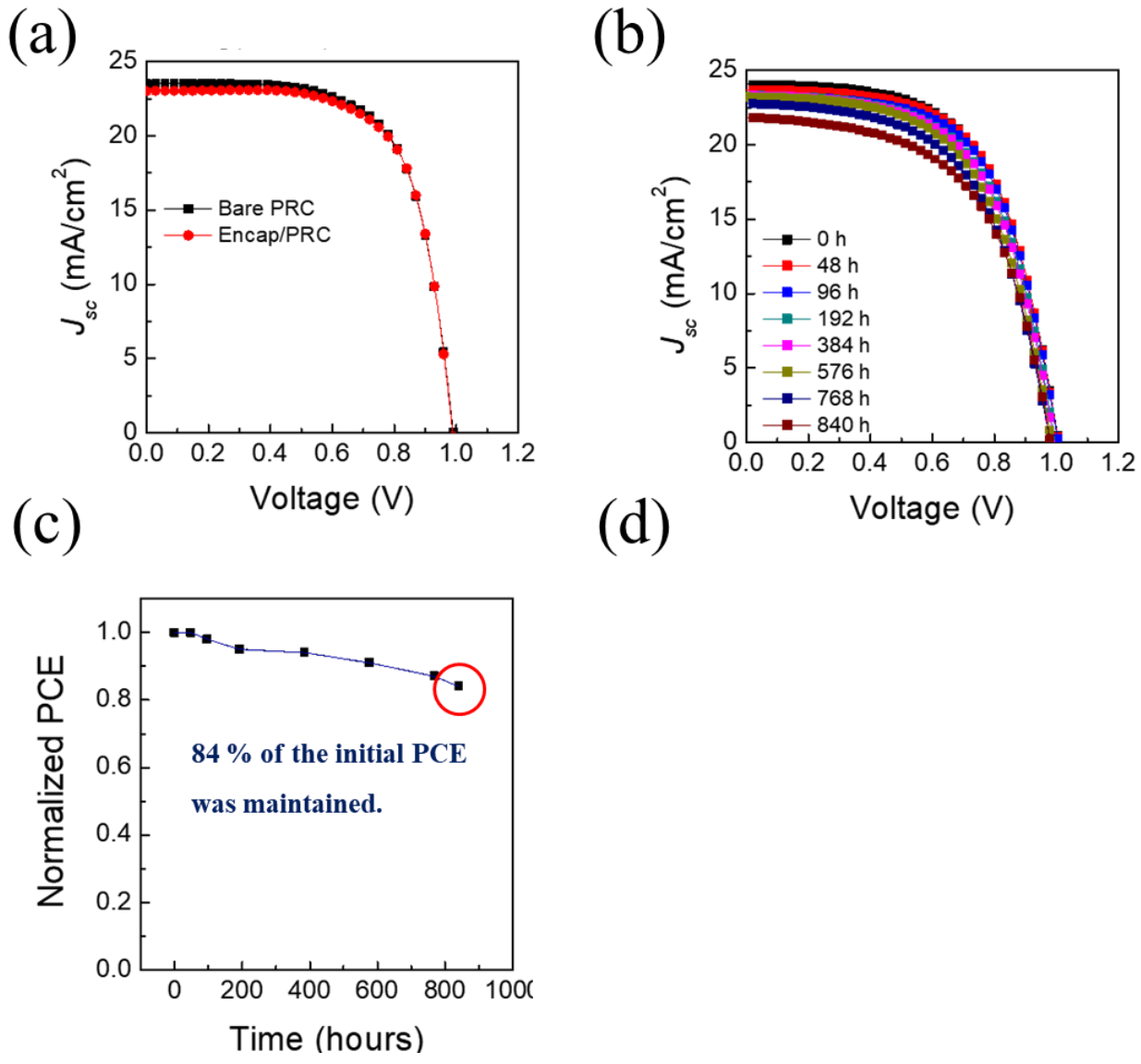

Figure 48 (a) J-V curves of bare PRC and encapsulated PRC with the encapsualtion layers. (b) Changes of J-V curves of encapsulated PSC at 85/85 °C/RH condition. (c) Normalized PCE changes of the encapsulated PSC

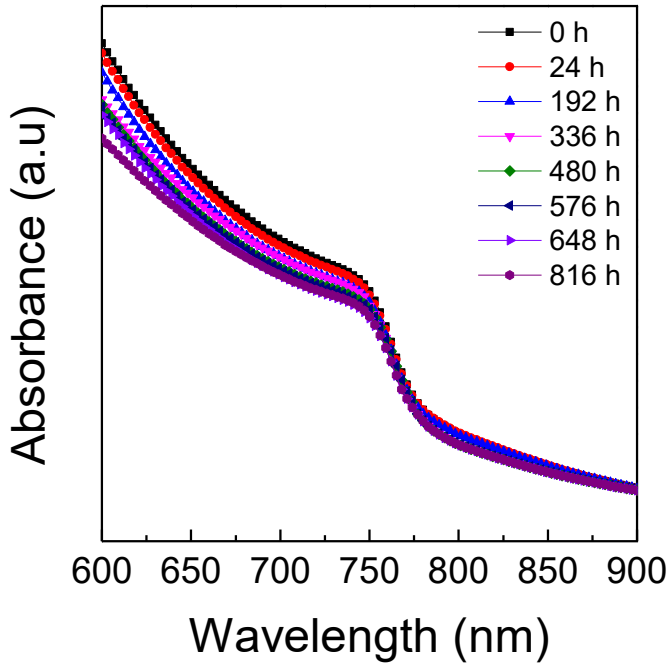

Figure 49 Time-dependent absorbance spectrum of the perovskite film with PMMA-PU/CeO_2(1.4 vol%) at 85/85 ℃/RH

In addition, self-healing effect of PSCs coated with the hydrophilic encapsulation layer was observed. To demonstrate this behavior, the intentionally degraded perovskite film after immersion in water at 85 ℃ was used to have thermal heat-treatment at 100 ℃ for 10 min shown in Figure 50. Before the thermal heat-treatment, the color of aged perovskite film was greyish or white. After heating at 100 ℃ for 10 min, the color of the aged perovskite film returned to dark due to the recovery of the perovskite phase. This is because hydrophilic PMMA/PU (50/50 wt%) IPNs/CeO_2 (1.4 vol%) layer trapped water and CH_3NH_3PbI (aqueous) after decomposition of $CH_3NH_3PbI_3$. The residual components in the encapsulation layer can further delay water penetration into the perovskite layer. During heat treatment at 100 ℃ for 10 min, the trapped

CH_3NH_3PbI was reacted with residual PbI_2 under the encapsulation layer, becoming $CH_3NH_3PbI_3$ again. This was clearly observed in Figure 50(a) by changing the grayish color to dark color. In addition, PCE of the aged PSC coated with the encapsulation layer recovered to 89 % of its initial PCE after thermal annealing, as shown in Figure 50(b). This indicates that self-recovery of perovskite film can be achieved with hydrophilic PMMA/PU (50/50 wt%) IPNs/CeO_2(1.4 vol%) by removing intercalated residual water.

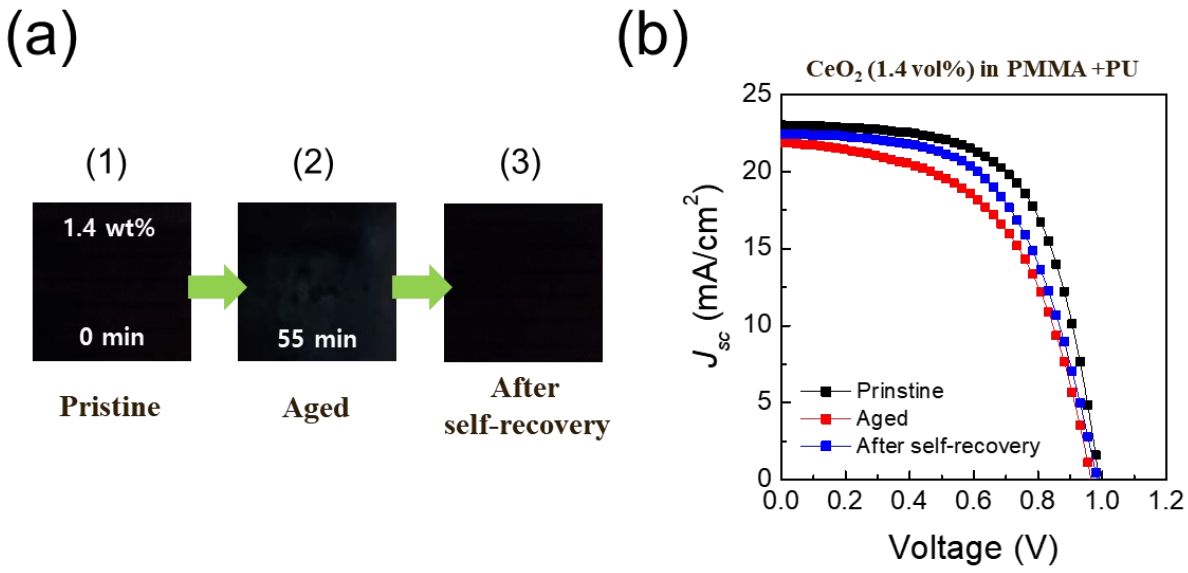

Figure 50 (a) Photographs of the encapsulated Perovskite layer before (1) test and after (2) degradation observed after 55 min in water at 85 ℃ and (3) after thermal heat treatment of the PSC at 100 ℃. (b) J-V curves of the PSCs before and after test and after self-recovery

4.4 Conclusion

IPNs nanocomposite successfully suppressed the accelerated degradation of the inverted PSC. PMMA/PU (50/50 wt%) IPNs exhibited better mechanical resistance to moisture, lowering water permeation rate in the film. This is because the interpenetration network and cross-linked of polymers prevented interfacial slip caused by swelling of the polymers. Moreover, the top hydrophobic PMMA/PU (50/50 wt%) IPNs/SiO_2 encapsulation layer increased contact angle, leading to decrease water molecule attachment on the surface. The diffusion of permeated water molecules was procrastinated, and they were trapped in the bottom hydrophilic PMMA/PU (50/50 wt%) IPNs/CeO_2 encapsulation layer. The PCE of encapsulated PSC maintained 84.0 % of the initial PCE after DH test for 816 h.

5.0 Highly Efficient and UV-Stable Perovskite Solar Cell by UV-Down Conversion

5.1 Background and Motivation

The perovskite ($CH_3NH_3PbI_3$) has a lot of beneficial characteristics, which can make it applicable to photovoltaics due to high absorption coefficient, long diffusion length of photo excited charges, tunable bandgap, and simple fabrication. However, there are major problems that hinder the commercialization of the PSCs. One of the major issues is related to UV light induced degradation of the perovskite. When TiO_2 as ETL is used in a PSC, degradation of the perovskite can be accelerated at the perovskite/TiO_2 interface due to the photocatalytic reaction.[8] To address this problem, several methods such as substitution of TiO_2 with Al_2O_3, addition of Sb_2S_3 interlayer between TiO_2 and perovskite interface, and usage of UV filter have been reported.[118-119]

Recently, UV-down conversion method has gained attention instead of UV filter. This is because the method can provide additional photon energy to the PSC devices, resulting in increase PCE. Moreover, this can solve the parasitic absorption caused by the commonly used transparent conductive oxide layer such as Fluorine-doped tin oxide (FTO), Indium tin oxide (ITO) and Indium zinc oxide (IZO). The power conversion efficiency is still limited due to the parasitic absorption of UV light. Therefore, UV down conversion to visible light can allow to boost PCE of the PSC device and enhance the device stability under UV light.[8]

In this work, commercially available fluorescent phosphors were selected for UV-down conversion. Since the phosphors have 1.6 ~ 1.8 of refractive index, reflection of the incident light in visible wavelength can be caused. This reduces the light absorption of the perovskite,

decreasing PCE of the device. To prevent this, a textured PDMS, which is an anti-reflective coating (ARC), was used and the phosphors were embedded in the ARC film. The film scatters the incident light, reducing light reflection caused by phosphors and surface reflection. As a result, PSC using the phosphors embedded ARC film shows 3.5 % improvement of IPCE in broadband visible spectrum while providing additionally 3.5 % increment of IPCE in UV region. The PCE of 18.49 % was achieved with short-circuit current of 22.54 mA/cm^2, voltage of 1.075 V and FF of 0.77. This method is applicable to the any single junction solar cells and multi-junction solar cells such as perovskite/Si tandem solar cell.

5.2 Experimental Section

5.2.1 Preparation of UV-Down Conversion Film

Commercially available phosphors (La_2O_2S:Tb) were purchased and added into PDMS solution. The well mixed solution with the phosphors was poured over the etched Si wafer (30 mm x 30 mm) and cured at 65 ℃ for 12 h. Finally, the cured PDMS layer was peeled off the Si wafer.

5.2.2 Fabrication of the PSC Device

Partially etched FTO coated glass (NSG TECTM 8.8 Ω/sq) was cleaned with acetone, DI water, and ethanol for 15 min, sequentially. A TiO_2 blocking solution was prepared using 0.15 M titanium diisopropoxide bis-(acetylacetonate) in 1-butanol and was spin-coated onto the FTO substrate at 3000 rpm for 30s after UV ozone treatment of the FTO substrate. The sample was annealed at 120 ℃ for 10 min. Mesoporous-TiO_2 nanoparticles in ethanol (1:5.5 wt%, Sharechem) were spin-coated onto the TiO_2(blocking layer)/FTO substrate at 4000 rpm for 30 s followed by annealing at 500 ℃ for 1 hour. The perovskite ($CH_3NH_3PbI_3$) solution was prepared in the same method as mentioned in chapter 2 and 4. 36 mg of Spiro-OMeTAD [2,2′,7,7′-tetrakis(N,N-di-p-methoxyphenyl-amine)9,9′-spirobifluorene] as HTL solution was dissolved in 500 μL of chlorobenzene. 14.4 μL of 4-tert-butyl pyridine and 8.8 μL of lithium-bis(trifluoro-methanesulfonyl)-imide (Li-TFSI) solution were added into the HTL solution. Li-TFSI solution was prepared by dissolving 180 mg of Li-TFSI in 250 μL of acetonitrile. The HTL solution was

spin-coated onto the of the perovskite at 4000 rpm for 30 s. 80 nm thick Au was deposited on top of HTL by e-beam evaporation.

5.2.3 Characterization

The photovoltaic performance of the devices with a metallic mask (active area 0.14 cm^2) under solar-simulated light (Oriel Sol 3A class AAA, Newport), which was calibrated by using a reference Si solar cell (PVM 95) was measured by an electrochemical workstation (CHI660, CHI Instrument). The incident photo-to-current conversion efficiency and integrated current of the PSCs were measured through quantum efficiency measurements within a spectra range of 280 – 800 nm wavelength in air under light illumination from a 300 W xenon lamp. The optical property was examined using PerkinElmer Lambda 35 UV/vis spectrometer equipped with an integrating sphere. Photoluminescence (PL) measurement was used to define the PL property of the fluorescent phosphors by using spectrofluorometer (QuantaMaster, PTI).

5.3 Results and Discussion

Apart from parasitic absorption of the transparent electrode used in PSCs, reflectance is also an important factor to be considered for high efficiency of PSCs. By using refractive indices of two different materials, reflectivity can be simply calculated as a following equation:

$$R = \left|\frac{n_2 - n_1}{n_2 - n_1}\right|^2 \quad (5.1)$$

For example, since refractive indices of Si and air are 3.5 and 1.0 respectively, the reflection at a front surface of silicon solar cell will be occurred over 30% due to the high refractive index contrast between Si and air. Optical losses caused by the reflected incident light at the front surface coverage decrease the generation of electron-hole pairs, resulting in lowering PCE of the device. It must be minimized in order to improve PCE of the solar cell.

The most common way to decrease the incident light reflection of Si solar cell is surface texturing. By texturing the surface of solar cells, the light path length through the solar cells is increased, promoting enhanced light absorption of the solar cell. This is because a textured surface will change an angle of incident light, resulting in increase of total amount of entered incident light into the solar cells. Recently, flexible textured polydimethylsiloxane (PDMS) has been developed as anti-reflective layer for the solar cells such as PSC, CIGS solar cell, and especially perovskite/silicon tandem solar cells with the flat top solar cell.

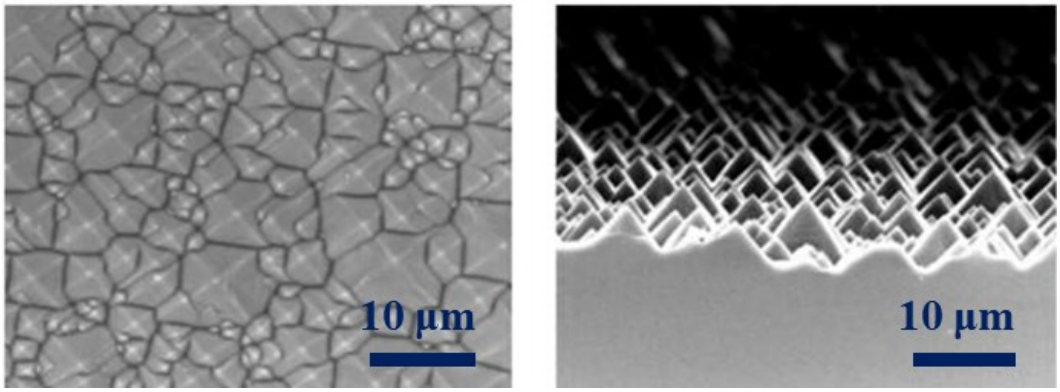

Figure 51 Plan and cross-sectional SEM views of the textured silicon master

To fabricate a textured PDMS as ARC film, pyramidal textured Si wafer was firstly formed by anisotropic KOH wet etching. For mono-crystalline silicon with a (100) surface orientation, the etching rate of (100) planes are faster than that of (111) planes due to higher packing density of (111) planes, creating of pyramidal structure of Si wafer in Figure 51.[120] After that, PDMS was coated on the textured silicon wafer and cured at 65 ℃ overnight. The film was transferred to the glass substrate.

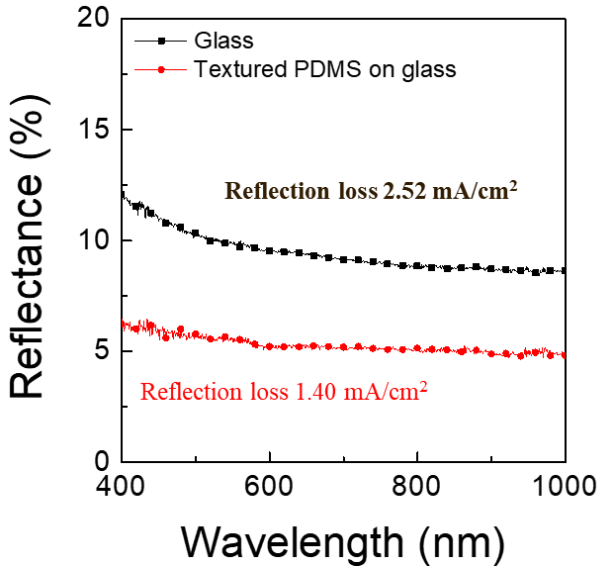

Figure 52 Reflectance of a glass and txtured PDMS on glass

Figure 52 indicates that reflectance of a textured PDMS on glass was decreased from 9.8 % at 550 nm to 5.5 % at 550m. The integrated reflected current density (reflection loss) decreased from 2.52 mA/cm^2 of ARC film to 1.40 mA/cm^2 of ARC_S(0.8). This is because an angle of incident light was changed by the texture surface, reducing reflectance on the front surface. As a result, the total amount of entered incident light to the perovskite layer was increased.

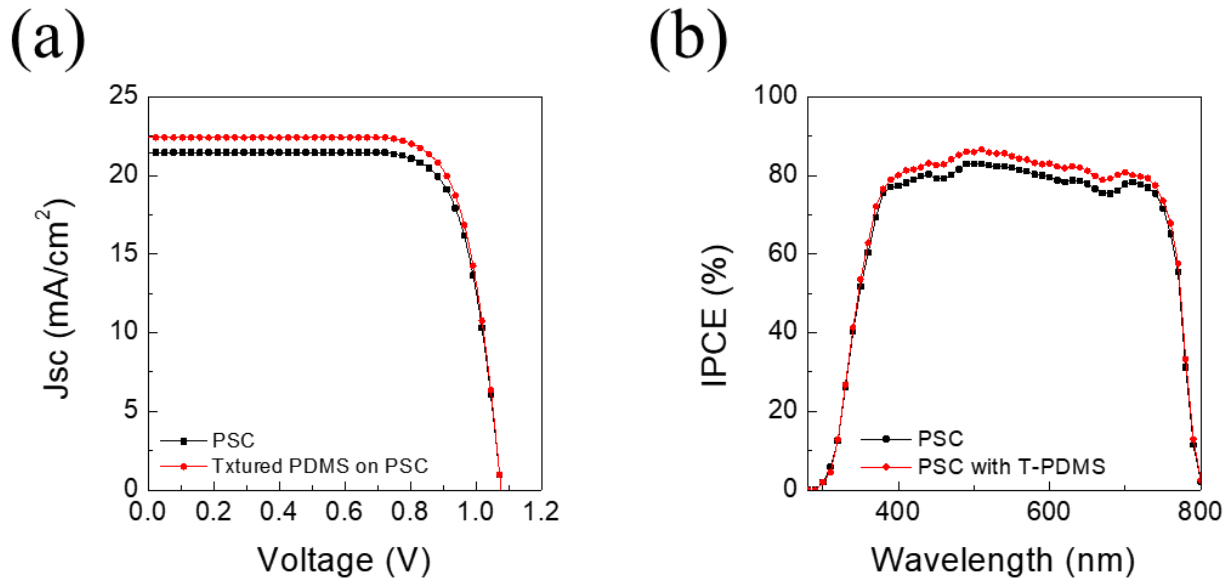

Figure 53 J-V curves and IPCE of the PSC and the PSC with the texutred PDMS

This anti-reflective layer was applied to the PSC structured with FTO/TiO_2/$CH_3NH_3PbI_3$/Spriro/Au. PCE of the device was boosted from 17.61 % without ARC film to 18.39 % with ARC film by increasing current density of 1.03 mA/cm^2 as shown in Figure 53(a). This is because the increased broadband absorption of the solar cell with the textured PDMS film from both reduced front surface reflection and increased light trapping in the solar cell provided by the scattering of the incident light as shown in Figure 53(b). These effects

contributed to the improved EQE and the PCE of the PSC device for all wavelengths. Thus, an anti-reflective layer is a potential technique to increase light absorption of a solar cell and the PCE.

To date, there are four representative UV down-conversion methods, which have been reported to improve PCE of single or multi-junction photovoltaics. Firstly, Yb^{3+}/Ce^{3+} co-doped quantum dots (QDs) $CsPbCl_{1.5}Br_{1.5}$ and Mn^{2+} doped $CsPbCl_3$ QDs exhibited effective UV down conversion to visible light with large Stroke shift. This technique led to improve PCE of Si solar cells. However, $CsPbCl_3$ perovskite based QDs may reduce transmitted incident light toward the light absorber of photovoltaics due to the relatively high refractive index (> 3.0). Secondly, $YVO_4:Bi^{3+}$, Eu^{3+} nanophosphors, Mn^{2+} doped $Cd_xZn_{1-x}S/ZnS$ quantum dots, and $CuGaS_2/ZnS$ nanocrystals, which have high luminescence quantum yield, were coated on the front side of Si solar cells in order to strongly emitted visible light in the active solar cell region by absorbing UV light. As a result, the spectral response of the solar cells in the ultraviolet region was increased. Since QDs can be degraded by oxygen, water, and thermal heating, it has a negative effect on long-term stability of the material. Thirdly, organic UV dye and Tris(β-diketonate) europium(III) Complexes embedded in polymers provide photogeneration by luminescent downshifting to the perovskite solar cell and copper indium gallium selenide (CIGS) solar cell. The polymers improved the stability of the materials but, commercial organic UV dyes, rear earth coordination complexes, and QDs are relatively high-cost and sophisticated technique for UV down conversion. Lastly, $(Ba, Sr)_2SiO_4:Eu^{2+}$ micron sized phosphors, which is cheap, commercially available, and stable, were added into textured PDMS as a UV down-converting film with high luminescence quantum yield.

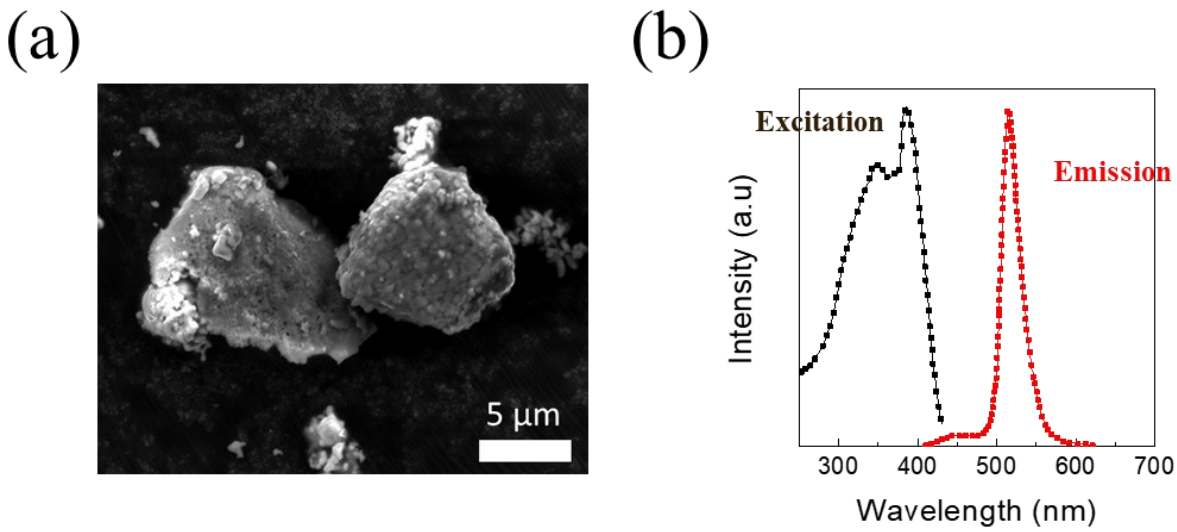

Figure 54 (a) SEM image of phosphors. (b) Excitation (λ_{ex}-380 nm) and Emission (λ_{em}: 518 nm) of phosphors

The fluorescent (green) phosphors (La_2O_2S:Tb) were selected as a luminophore given its commercial availability and was firstly characterized for the material's morphology and optical property. Figure 54(a) shows SEM image of the phosphors which indicate the particles size of 5 – 8 µm in spherical shape. Photoluminescence (PL) excitation (black curve) and PL emission (red curve) spectra of the phosphors are shown in Figure 54(b). The excitation ranges from 280 nm to 420 nm but is peaked at 390 nm, which is short enough for the UV down-converting for perovskite solar cell devices.

Figure 55 shows the real photo images of the textured PDMS, which is incorporated with the green phosphors for down-converting UV light to visible light under ambient light (top) and under UV (365 nm) light (bottom). This strong green light emission under UV light indicates that the phosphors in the film are well distributed. In particular, the absorption spectrum of the phosphors is in the short-wavelength where the perovskite exhibits a minimum incident photon-to-current conversion efficiency. As a result, the phosphors embedded ARC film can additionally generate photons in UV region, resulting in improved current density of the device.

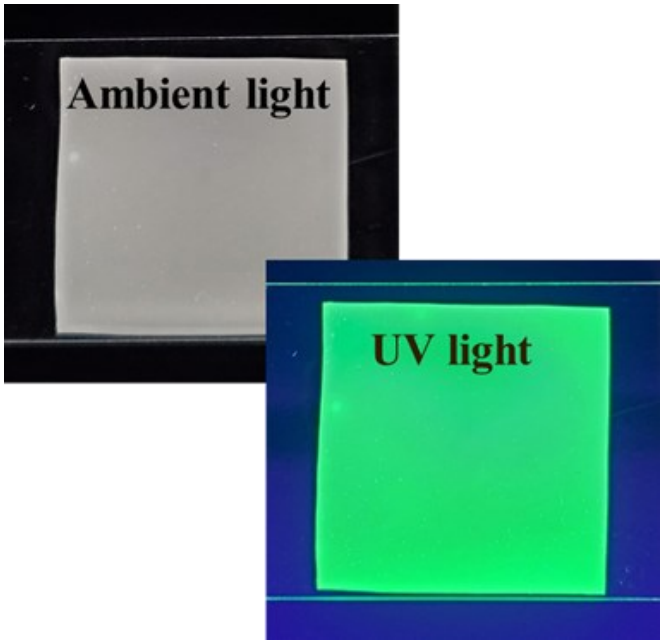

Figure 55 Photos of phosphor-incorporated ARC film under ambient light and UV (365 nm) light

After application of the ARC film with four different volume concentrations of 0.2 vol%, 0.4 vol%, 0.8 vol%, and 1.2 vol% to the PSC, the J-V curves and IPCE of the device were measured as shown in Figure 56 to further investigate an effect of phosphors on device performance.

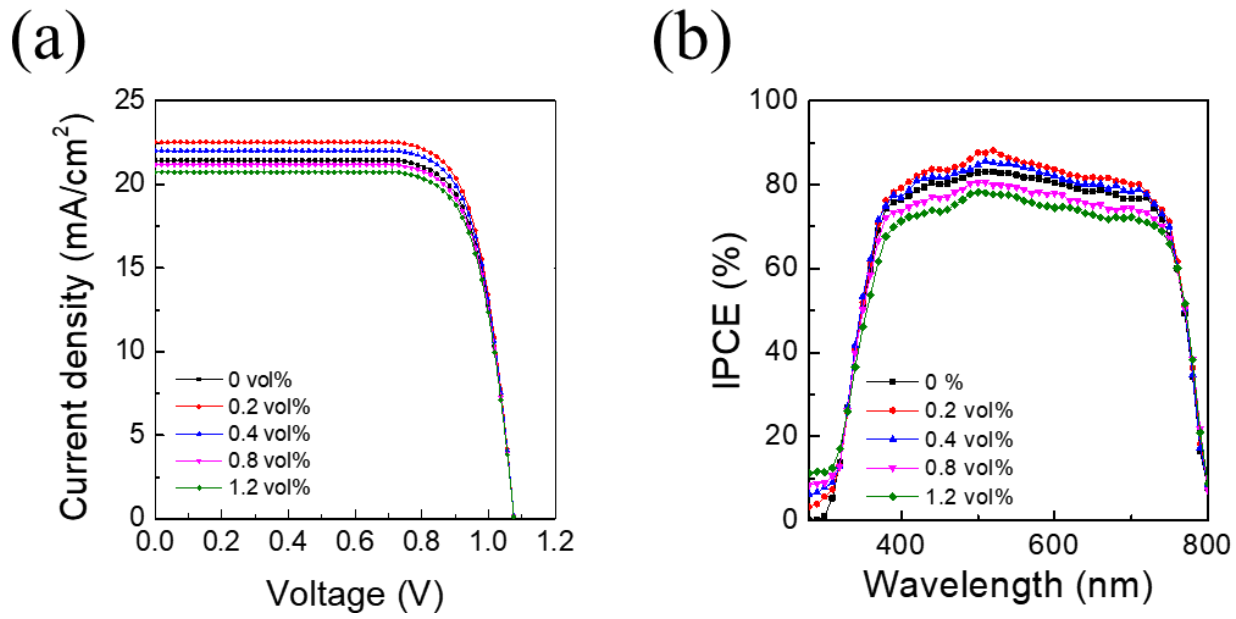

Figure 56 (a) J-V curve, (b) IPCE of the PSC with textured PDMS as a function of volume %(0.2 vol%, 0.4 vol%, 0.8 vol%, and 1.2 vol%) of green phoshors in textured PDMS

Figure 56(a) shows that Jsc of the device with 0.2 % of phosphors embedded in ARC was improved from 21.46 mA/cm^2 to 22.54 mA/cm^2 whereas Voc and fill factor did not change much. 18.47 % of PCE was achieved with Jsc of 22.53 mA/cm^2, Voc of 1.08 V, and FF of 76.31 %. This is because improved Jsc comes from increased IPCE response in the UV region due to the down-conversion effect by the green phosphor in the ARC film in Figure 56(b). As the volume concentration of the green phosphors in the textured PDMS increases, the improvement in IPCE in the UV region is clearly observed in Figure 56(b). In addition, the absorption of the perovskite in broadband visible spectrum was increased due to the scattering effect induced by textured surface of the ARC film.

However, decreased IPCE was observed in the visible range wavelength as the volume concentration of the green phosphors was increased. This is mostly due to the higher reflection caused by the larger particle size and shape of phosphors. Large particle size over (> 5 μm) may

increase the backward scattering of the incident light and light reflection at the surface of the particle in backward direction. In addition, since the phosphors, which have higher refractive index (1.6 ~ 1.8) than that (1.4) of PDMS, gradually increased refractive index of the ARC film. As shown in Figure 57, reflectance of the ARC film with increased volume concentration of phosphors is increased. Higher reflection decreased the incident light absorption of the perovskite, reducing the current density. Although an additional photon energy in UV region was provided to the perovskite, overall PCE of the device was reduced due to higher reflection in visible wavelength.

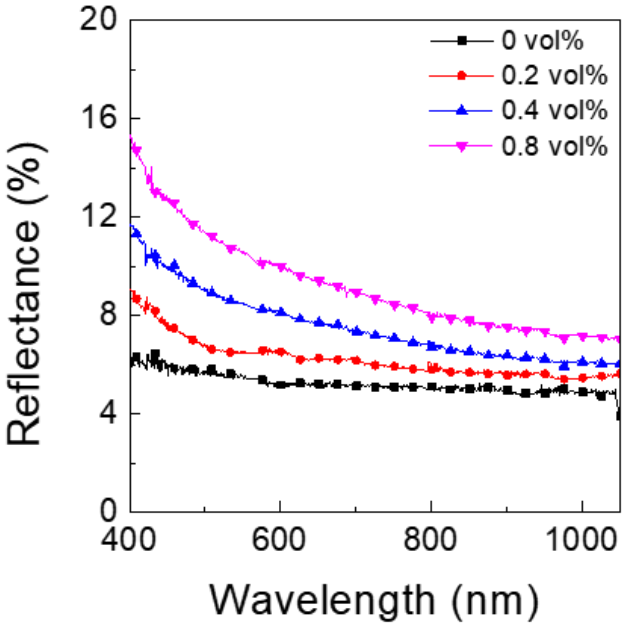

Figure 57 The reflectance of the textured PDMS with different vol% (0.2, 0.4, and 0.8) on a glass substrate

Finally, UV stability of PSCs with the phosphors embedded ARC film was examined. The devices were exposed to UV light (365 nm wavelength) at 15 W/cm^2. Figure 58shows the normalized PCE of PSCs as a function of time. After a 24 h aging test, the PSCs of the film

maintained 93% of the initial PCE and do not show any degradation process of the perovskite layer. To compare the UV light stability, the PSC device without film was deteriorated after 24 hours under UV light due to the photocatalytic reaction at the perovskite/TiO_2 interface. Thus, the ARC film not only provides additional photon energy by UV down conversion method but also improves UV stability.

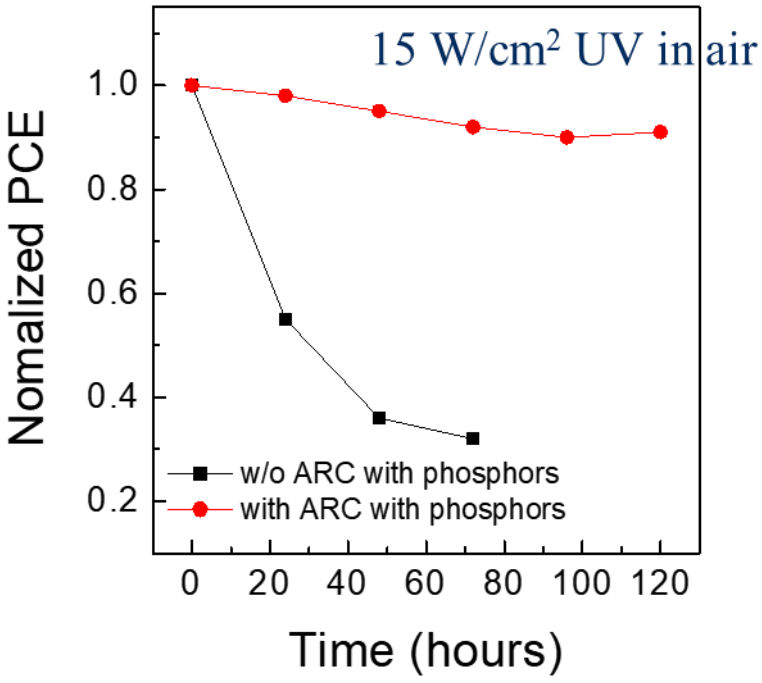

Figure 58 UV stability test of PSCs without and with the phosphors embedded ARC film at 15 W/cm^2 UV in air ambience

5.4 Conclusion

The optical property of the phosphor embedded ARC film was systematically investigated as function of volume % of phosphors. The reflection loss of 1.12 mA/cm^2 was decreased by ARC layer because textured surface scatters the incident light preferentially toward the inside of the solar cell leading to reduced reflection on the font surface. By addition of green phosphors into ARC film, additional photon energy was generated by converting UV light to green light, resulting in higher efficiency of 18.49 % with a short-circuit current of 22.54 mA/cm^2, voltage of 1.07 V, and FF of 76.31 %. This film improved UV stability of the PSC and maintained 91 % of the initial PCE of the device after 100 hours of UV exposure at 15 W/cm^2 in air. Moreover, this method can apply not only single junction solar cell but also multi-junction solar cell such as perovskite/Si tandem solar cell.

6.0 Conclusion, Broader Implications, and Future Work

The aim of the study is to create highly efficient energy conversion perovskite solar cell devices with highly improved stability under harsh environment. The study showed that interface and stability are important factors for efficient and stable perovskite solar devices. Controlled oxidation of Ni for stress-free hole transport layer is increased charge transport without I-V hysteresis. Better performance of PSCs with TiO_2 as ETL can be achieved but different charge transport behavior was observed. To see the perovskite – TiO_2 interface effect on the charge transport behavior under different polarity, ReRAM device, which works under positive bias and negative vias, was fabricated. The interface controls the conductive chain formation and causes the asymmetric bipolar resistive switching. Polymer-oxide nanoparticle composites were used to elongate the lifetime of the perovskite layer under DH test. This passivation delayed water molecule diffusion into the perovskite layer, resulting in exhibiting suppressed degradation process of perovskite in a standardized damp heat aging condition (85/85 ℃/RH condition). In addition, the phosphors embedded in anti-reflective coating (ARC) layer improved the UV stability of PSCs while providing addition photon energy to the PSC.

Broder implications: Oxidation of Ni for stress-free hole transport layer can be applied to the large-scale manufacturing of PSCs with high-quality and uniformity of NiO films on large substrates. By modifying the interface between perovskite and oxide material, charge transport behavior can be improved in order to have efficient PSCs and can be also sued to new application such as ReRAM. A simple and effective passivation method using polymer-oxide composites have benefits for solar cell application. Manufacturing cost for solar cells is very important to be competitive in the solar cell market. This simple encapsulation method based on

polymer is a potential candidate to replace the glass encapsulation while providing less manufacturing cost for solar cell application. In addition, this passivation is an alternate protection method for electrical components, which should be sealed to prevent contact with the explosive atmosphere. Phosphor embedded ARC film can be applied to conventional solar cell devices and emerging photovoltaics. It can provide additional photon energy to the light absorber in solar cell devices by converting harmful UV photons to usable visible light that allows to boost PCE of the devices.

Future work: PSCs have significantly improved in efficiency and addressed few issues such as hysteresis, photocatalytic dissociation, and instability under humid condition for commercialization over the past years. However, the efficiency of the PSCs is limited due to the theoretical limitation of the single-junction solar cell. In addition, Si solar cell has the same issue, which is efficiency limitation (29.43 %) as single-junction solar cell owing to the thermalization loss. Multi-junction is a one way to increase theoretical efficiency. So, higher bandgap cell is required to decrease of thermalization loss on top of Si solar cell as shown in Figure 59. This method increases the efficiency of a solar cell with the split spectrum, which is optimized to each of the spectrum. Perovskite solar cells, which have higher bandgap, 1.5 eV, are a promising candidate as the top-cell on the bottom Si solar cell. Green and blue light will be absorbed by PSC, converting photon energies to electric power in multi-junction structured with the bottom Si solar cell. Figure 59 shows that the rest of incident light, red light, will be converted to free charge carriers by the Si solar cell, resulting in improvement of the PCE with less thermalization loss.

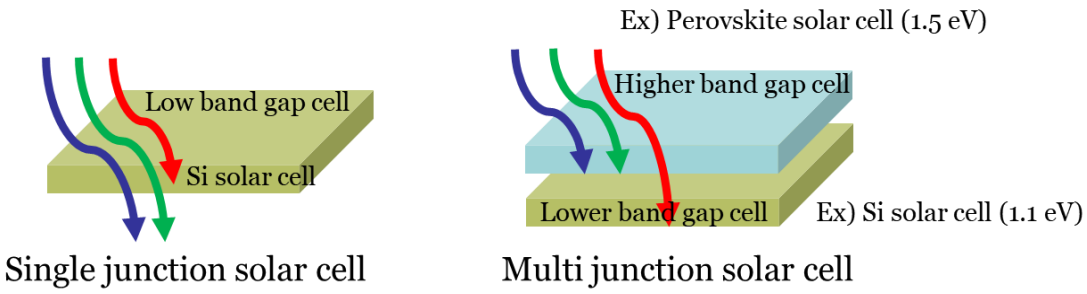

Figure 59 Scheme illustration of solar irrdiance absorption for single and multi-junction solar cell

Bibliography

[1] Perez, R.; Perez, M., A fundamental look at energy reserves for the planet. *The International Energy Agency SHC Programme Solar Update*, **2009**, 50, 2-3.

[2] *McKinsey Energy Insight' Global Energy Perspectives*, **2019**, 17.

[3] Noman, M. A. A.; Abden, M. J.; Islam, M. A., Germanium Telluride Absorber Layer, A proposal for Low Illumination Photovoltaic Application Using AMPS 1D, 2018 International Conference on Computer, Communication, Chemical, Material and Electronic Engineering, 2018, 1-5.

[4] Fulay, P.; Lee, J. -K., Electronic, magnetic, and optical materials. Boca Raton: CRC Press, 2016.

[5] Best Research-cell Efficiency Chart, https://www.nrel.gov/pv/cell-efficiency.html

[6] Green, M. A.; Ho-Baillie, A.; Snaith, H. J., The emergence of perovskite solar cells. *Nature Photonics* **2014,** 8, 506–514.

[7] Yoo, J. S.; Han, G. S.; Lee, S.; Kim, M. C.; Choi, M.; Jung, H. S.; Lee, J. -K. Dual function of a high-contrast hydrophobic-hydrophilic coating for enhanced stability of perovskite solar cells in extremely humid environments, *Nano Research* **2017,** 10, 3885-3895.

[8] Roh, H. -S.; Han, G. S.; Lee, S.; Kim, S.; Choi, S.; Yoon, C. New down-converter for UV-stable perovskite solar cell: Phosphors-in-glass, *Journal of Power Sources* **2018,** 389, 135–139.

[9] Yu, F.; Han, G. S.; Tu, Y. J.; Roh, H. -S.; Lee, J. -K. Electron extraction mechanism in low hysteresis perovskite solar cells using single crystal TiO_2 nanorods, *Solar energy* **2018,** 167, 251-257.

[10] Kwon, U.; Kim, B. G.; Nguyen, D. C.; Park, J. H.; Ha, N. Y.; Kim, S. J.; Ko, S. H.; Lee, S.; Lee, D.; Park, H. J. Solution-processible crystalline NiO nanoparticles for high-performance planar perovskite photovoltaic cells. *Sci. Rep.* **2016,** 6, 30759.

[11] Wang, K. C.; Jeng, J. Y.; Shen, P. S.; Chang, Y. C.; Diau, W. G. G.; Tsai, C. H.; Chao, T. Y.; Hsu, H. C.; Lin, P. Y.; Chen, P. et al. P-type mesoscopic nickel oxide/organometallic perovskite heterojunction solar cells. *Sci. Rep.* **2014,** 4, 4756.

[12] Ming, W.; Chen, S.; Du, M.-H., Chemical instability leads to unusual chemical-potential-independent defect formation and diffusion in perovskite solar cell material $CH_3NH_3PbI_3$. *J. Mater. Chem. A* **2016,** 4, 16975–16981.

[13] Hwang, I.; Jeong, I.; Lee, J.; Ko, M. J.; Yong, K. Enhancing stability of perovskite solar cells to moisture by the facile hydrophobic passivation, *ACS Appl. Mater. Interfaces* **2015,** 7, 17330−17336.

[14] Ma, L.; Guo, D.; Li, M.; Wang, C.; Zhou, Z.; Zhao, X.; Zhang, F.; Ao, Z.; Nie, Z. Temperature-dependent thermal decomposition pathway of organic-inorganic halide perovskite materials, *Chem. Mater.* **2019,** 31, 20, 8515–8522.

[15] Encapsulation Advancements Extend Life of Thin-Film PV, https://www.nrel.gov/docs/fy10osti/47564.pdf

[16] Vijayakumari, G.; Selvakumar, N.; Jeyasubramanian, K.; Mala, R., Investigation on the Electrical Properties of Polymer metal Nanocomposites for Physiological sensing applications, *Physics Procedia,* **2013**, 49, 67 – 78

[17] Balke, S. T.; Hamielec, A. E., Bulk polymerization of methyl methacrylate, *J. Appl. Polym. Sci* **1973,** 17, 905-949.

[18] Lee, S.; Roh, H. -S.; Han, G. S.; Lee, J. -K., Controlled oxidation of Ni for stress-free hole transport large-scale perovskite solar cells. *Nano Research* **2019,** 12, 3089–3094.

[19] Kim, H.-S.; Lee, C.-R.; Im, J.-H.; Lee, K.-B.; Moehl, T.; Marchioro, A.; Moon, S.-J.; Humphry-Baker, R.; Yum, J.-H.; Moser, J. E.; Grätzel, M.; Park, N.-G. Lead iodide perovskite sensitized all-solid-state submicron thin film mesoscopic solar cell with efficiency exceeding 9%. *Sci. Rep*. **2012**, 2, No. 591.

[20] Jeon, N. J.; Noh, J. H.; Kim, Y. C.; Yang, W. S.; Ryu, S.; Seok, S. I. Solvent engineering for high-performance inorganic−organic hybrid perovskite solar cells. *Nat. Mater.* **2014**, 13, 897−903.

[21] Burschka, J.; Pellet, N.; Moon, S.-J.; Humphry-Baker, R.; Gao, P.; Nazeeruddin, M. K.; Grätzel, M. Sequential deposition as a route to high-performance perovskite-sensitized solar cells. *Nature* **2013**, 499, 316−319.

[22] Ahn, N.; Son, D.-Y.; Jang, I.-H.; Kang, S. M.; Choi, M.; Park, N.-G. Highly reproducible perovskite solar cells with average efficiency of 18.3% and best efficiency of 19.7% fabricated via Lewis Base Adduct of lead(II) iodide. *J. Am. Chem. Soc*. **2015**, 137, 8696−8699.

[23] Chen, B.; Yang, M. J.; Priya, S.; Zhu, K. Origin of J−V hysteresis in perovskite solar cells. *J. Phys. Chem. Lett.* **2016,** 7, 905−917.

[24] Han, G. S.; Shim, H.-W.; Lee, S.; Duff, M. L.; Lee, J.-k. Low-temperature modification of ZnO nanoparticles film for electron-transport layers in perovskite solar cells. *ChemSusChem* **2017**. 10. 2425-2430.

[25] Han, G. S.; Yoo, J. S.; Yu, F.; Duff, M. L.; Kang, B. K; Lee, J.-K. Highly stable perovskite solar cells in humid and hot environment. *J. Mater. Chem. A*. **2017**, 5, 14733.

[26] Heo, J. H.; Han, H. J.; Kim, D.; Ahn, A. K.; Im, S. H. Hysteresis-less inverted $CH_3NH_3PbI_3$ planar perovskite hybrid solar cells with 18.1% power conversion efficiency. *Energy Environ. Sci.* **2015**, 8, 1602.

[27] Norrman, K.; Madsen, M. V.; Gevorgyan, S. A.; Krebs, F. C. Degradation patterns in water and oxygen of an inverted polymer solar cell. *J. Am. Chem. Soc*. **2010**. 132, 16883–16892.

[28] Jorgensen, M.; Norrman, K.; Krebs, F. C. Stability/degradation of polymer solar cells. ol. Eng. Mater. Sol. Cells **2008**. 92. 686–714.

[29] Yin, X. T.; Guo, Y. X.; Xie, H. X.; Que, W. X.; Kong, L. B. Nickel oxide as efficient hole transport materials for perovskite solar cells. *Sol. RRL* **2019,** 3, 1900001.

[30] Yin, X. T.; Que, M. D.; Xing, Y. L.; Que, W. X. High efficiency hysteresis-less inverted planar heterojunction perovskite solar cells with a solution derived NiOx hole contact layer. *J. Mater. Chem. A* **2015,** 3, 24495–24503.

[31] Yin, X. W.; Yao, Z. B.; Luo, Q.; Dai, X. Z.; Zhou, Y.; Zhang, Y.; Zhou, Y. Y.; Luo, S. P.; Li, J. B.; Wang, N. et al. High efficiency inverted planar perovskite solar cells with solution-processed NiOx hole contact. *ACS Appl. Mater. Interfaces* **2017,** 9, 2439–2448.

[32] Eperon, G. E.; Burlakov, V. M.; Docampo, P.; Goriely, A.; Snaith, H. J. Morphological Control for High Performance, Solution-processed planar heterojunction perovskite solar cells. *Adv. Funct. Mater*. **2014**, 24, 151–157.

[33] Li, C.; Jiang, Y.' Deng, S.; Tam, A.; Xu, P.; Wong, M.; Kwok, H.-S. Overcoming the limitations of sputtered nickel oxide for high-efficiency and large-area perovskite solar cells. *Adv. Sci*. **2017**, 4, 1700463.

[34] Peng, Y. Y.; Cheng, Y. D.; Wang, C. H.; Zhang, C. J.; Xia, H. Y.; Huang, K. Q.; Tong, S. C.; Hao, X. T.; Yang, J. L. Fully doctor-bladed planar heterojunction perovskite solar cells under ambient condition. *Org. Electron.* **2018,** 58, 153–158.

[35] Wang, T.; Ding, D.; Wang, X.; Zeng, R. R.; Liu, H.; Shen, W. Z. High performance inverted perovskite solar cells with mesoporous NiOx hole transport layer by electrochemical deposition. *ACS Omega* **2018,** 3, 18434−18443.

[36] Seo, S.; Park, I. J.; Kim, M.; Lee, S.; Bae, C.; Jung, H. S.; Park, N.-G.; Kim, J. Y.; Shin, H. An ultra-thin, un-doped NiO hole transporting layer of highly efficient (16.4%) organic–inorganic hybrid perovskite solar cells. *Nanoscale* **2016**, 8, 11403.

[37] Pae, S. R.; Byun, S.; Kim, J.; Kim, M.; Gereige, I.; Shin, B. Improving uniformity and reproducibility of hybrid perovskite solar cells via a low-temperature vacuum deposition process for NiO_x hole transport layers. ACS Appl. Mater. Interfaces 2018, 10, 534−540.

[38] Park, J. H.; Seo, J.; Park, S.; Shin, S. S.; Kim, Y. C.; Jeon, N. J.; Shin, H.-W.; Ahn, T. K.; Noh, J. H.; Yoon, S. C.; Hwang, C. S.; Seok, S. I. Efficient $CH_3NH_3PbI_3$ perovskite solar cells

employing nanostructured p-type NiO electrode formed by a pulse laser deposition. *Adv. Mater*. **2015**, 27, 4013–4019.

[39] Mitra, R. *Structural Intermetallics and Intermetallic Matrix Composites*. CRC Press: Boca Raton, 2015.

[40] Unutulmazsoy, Y.; Merkle, R.; Fischer, D.; Mannhart, J.; Maier, J. The oxidation kinetics of thin nickel films between 250 and 500 °C. *Phys. Chem. Chem. Phys.* **2017,** 19, 9045–9052.

[41] Giovanardi, C.; di Bona, A.; Altieri, S.; Luches, P.; Liberati, M.; Rossi, F.; Valeri, S. Structure and morphology of ultrathin NiO layers on Ag (001). *Thin Solid Films* **2003,** 428, 195–200.

[42] Liu, C.; Huntz, A. M.; Lebrun, J. L. Origin and development of residual stresses in the Ni-NiO system: In-situ studies at high temperature by X-ray diffraction. *Mater. Sci. Eng. A* **1993,** 160, 113–126.

[43] Schade, H.; Smith, Z. E. Mie scattering and rough surfaces. *Appl. Opt.* **1985,** 24, 3221–3226.

[44] González-Alcalde, A. K.; Méndez, E. R.; Terán, E.; Cuppo, F. L. S.; Olivares, C. J. A.; García-Valenzuela, A. Reflection of diffuse light from dielectric one-dimensional rough surfaces. *J. Opt. Soc. Am. A* **2016,** 33, 373–382.

[45] Hutchinson, J. W. Stresses and Failure Modes in Thin films and Multilayers; Technical University of Denmark: Lyngby, 1996.

[46] Nastasi, M.; Höchbauer, T.; Lee, J. K.; Misra, A.; Hirth, J. P. Nucleation and growth of platelets in hydrogen-ion-implanted silicon. *Appl. Phys. Lett.* **2005,** 86, 154102.

[47] Lee, J. K.; Lin, Y.; Jia, Q. X.; Höchbauer, T.; Jung, H. S.; Shao, L.; Misra, A.; Nastasi, M. Role of strain in the blistering of hydrogen-implanted silicon. *Appl. Phys. Lett.* **2006,** 89, 101901.

[48] Jamal, M. S.; Shahahmadi, S. A.; Chelvanathan, P.; Alharbi, H. F.; Karim, M. R.; Dar, M. A.; Luqman, M.; Alharthi, N. H.; Al-Harthi, Y. S.; Aminuzzaman, M. et al. Effects of growth temperature on the photovoltaic properties of RF sputtered undoped NiO thin films. *Results Phys.* **2019,** 14, 102360.

[49] Mahalingam, T.; John, V. S.; Ravi, G.; Sebastian, P. J. Microstructural characterization of electrosynthesized ZnTe thin films. *Cryst Res. Technol.* **2002,** 37, 329–339.

[50] Dabrowski, J.; Müssig, H. J. Silicon Surfaces and Formation of Interfaces: Basic Science in the Industrial World; World Scientific: Singapore, 2000; pp 414–416.

[51] Tosha, K.; Iida, K. Residual Stress and Hardness Distributions Induced by Shot Peening; International Scientific Committee for Shot Peening: Tokyo, Japan, 1990; pp 379–388.

[52] Chen, X.; Vlassak, J. J. Numerical study on the measurement of thin film mechanical properties by means of nanoindentation. *J. Mater. Res.* **2001,** 16, 2974–2982.

[53] Pharr, G. M.; Oliver, W. C.; Brotzen, F. R. On the generality of the relationship among contact stiffness, contact area, and elastic modulus during indentation. *J. Mater. Res.* **1992,** 7, 613–617.

[54] Wang, Z. G. Influences of sample preparation on the indentation size effect & nanoindentation pop-in in nickel. Ph.D. Dissertation, University of Tennessee, Knoxville, 2012.

[55] Fasaki, I.; Koutoulaki, A.; Kompitsas, M.; Charitidis, C. Structural, electrical and mechanical properties of NiO thin films grown by pulsed laser deposition. *Appl. Surf. Sci.* **2010,** 257, 429–433.

[56] De Los Santos Valladares, L.; Ionescu, A.; Holmes, S.; Barnes, C. H. W. Characterization of Ni thin films following thermal oxidation in air. *J. Vac. Sci. Technol. B* **2014,** 32, 051808.

[57] Zhang, J.; Zhang, L.; Dong, Y.; Li, H. Y.; Tan, C. M.; Xia, G.; Tan, C. S. The dependency of TSV keep-out zone (KOZ) on Si crystal direction and liner material. In 2013 IEEE International 3D Systems Integration Conference, San Francisco, CA, USA, 2013.

[58] Lee, S.; Wolfe, S.; Torres, J.; Yun, M.; Lee, J. -K., Asymmetric bipolar resistive switching of halide perovskite film in contact with TiO_2 layer. *ACS Appl. Mater. Interfaces* **2021**, 13, 27209-27216.

[59] Goux, L.; Valov, I., Electrochemical processes and device improvement in conductive bridge RAM cells. *Phys. Status Solidi A* **2016,** 213, 274-288.

[60] Privitera, S.; Bersuker, G.; Lombardo, S.; Bongiorno, C; Gilmer, D.C., Conductive filament structure in HfO_2 resistive switching memory. *Solid-State Electron.* **2015,** 111, 161.

[61] Li, Y.; Long, S.; Liu, Q.; Lv, H.; Liu, M., Resistive switching performance improvement via modulating nanoscale conductive filament, involving the application of two-dimensional layered materials. *small* **2017,** 13, 1604306.

[62] Valov, I.; Kozicki, M. N., Cation-based resistance change memory. *J. Phys. D: Appl. Phys.***2013**, 46, 074005.

[63] Valov, I.; Tsuruoka, T., Effects of moisture and redox reactions in VCM and ECM resistive switching memories. *J. Phys. D: Appl. Phys.***2018**, 51, 413001.

[64] Zhao, L.; Chen, H. -Y.; Wu, S. -C.; Jiang, Z.; Yu, S.; Hou, T. -H.; Wong, H. -S. P.; Nishi, Y. Multi-level control of conductive nano-filament evolution HfO_2 ReRAM by pulse-train operations. *Nanoscale* **2014,** 6, 5698.

[65] Lee, D.; Woo, J.; Park, S.; Cha, E.; Lee, S.; Hwang, H. Dependence of reactive metal layer on resistive switching in a bi-layer structure Ta/HfO_x filament type resistive random access memory. *Appl. Phys. Lett.* **2014,** 104, 083507.

[66] Song, S. J.; Seok, J, Y.; Yoon, J. H.; Kim, K. M.; Kim, G. H.; Lee, M. H.; Hwang, C. S. Real-time identification of the evolution of conducting nano-filament in TiO_2 thin film ReRAM. *Sci. Rep.* **2013,** 3, 3443.

[67] Filip, M. R.; Eperon, G. E.; Snaith, H. J.; Giustino, F., Steric engineering of metal-halide perovskite with tunable optical band gaps. *Nat. Commun* **2014,** 5, 5757.

[68] Lee, M. M.; Teuscher, J.; Miyasaka, T.; Murakami, T. N.; Snaith, H. J. Efficient hybrid solar cells based on meso-superstructured organometal halide perovskites. *Science* **2012,** 338, 643−647.

[69] Kojima, A.; Teshima, K.; Shirai, Y.; Miyasaka, T. Organometal halide perovskite as visible-light sensitizers for photovoltaic cells. *J.Am. Chem. Soc.* **2009,** 131, 6050–6051.

[70] Im, J. -H.; Lee, C. -R., Lee, J. -W.; Park, S. -W.; Park, N. -G., 6.5% efficient perovskite quantum-dot-sensitized solar cell. *Nanoscale,* **2011,** 3, 4088-4093.

[71] Park, N.-G. Perovskite solar cells: an emerging photovoltaic technology. *Mater. Today* **2015,** 18, 2.

[72] Tan, Z.–K.; Moghaddam, R.S.; Lai, M.L.; Docampo, P.; Higler, R.; Deschler, F.; Price, M.; Sadhanala, A.; Pazos, L.M.; Credgington, D.; Hanusch F.; Bein, T.; Snaith, H.J.; Friend, R.H. Bright light-emitting diodes based on organometal halide perovskite. *Nat. Nanotech.* **2014,** 9, 687–692.

[73] Kim, Y.–H.; Cho, H.; Heo, J.H.; Kim, T.-S.; Myoung. N.; Lee, C.-L.; Im, S.H.; Lee, T.-W. Multicolored organic/inorganic hybrid perovskite light-emitting diodes. *Adv. Mater.* **2015,** 27, 1248–1254.

[74] Cho, H.; Jeong, S.-H.; Park, M.-H.; Kim, Y.-H.; Wolf, C.; Lee, C.-L., Heo, J.H.; Sadhanala, A.; Myoung, S.; Yoo, S.; Im, S.H.; Friend, R.H.; Lee, T.-W. Overcoming the electroluminescence efficiency limitation of perovskite light-emitting diodes. *Science* **2015,** 350, 1222–1225.

[75] Senanayak, S. P.; Yang, B.; Thomas, T. H.; Giesbrecht, N.; Huang, W.; Gann, E.; Nair, B.; Goedel, K.; Guha, S.; Moya, X.; McNeill, C. R.; Docampo, P.; Sadhanala, A.; Friend, R. H.; Sirringhaus, H. Understanding charge transport in lead iodide perovskite thin-film field-effect transistors. *Sci. Adv.* **2017,** 3, e1601935.

[76] Lee, Y.; Kwon, J.; Hwang, E.; Ra, C. -H.; Yoo, W. J.; Ahn, J. -H.; Park, J. H.; Cho, J. H. High-performance perovskite-graphene hybrid photodetector. *Adv. Mater.* **2015,** 27, 41–46.

[77] Zhu, H.; Fu, Y.; Meng, F.; Wu, X.; Gong, Z.; Ding, Q.; Gustafsson, M. V.; Trinh, M. T.; Jin, S.; Zhu. X. -Y. Lead halide perovskite nanowire lasers with low lasing thresholds and high quality factors. *Nature materials* **2015,** 15, 636-642.

[78] Yuan, Y.; Huang, J. Ion migration in organometal trihalide perovskite and its impact on photovoltaic efficiency and stability. *Acc. Chem. Res.* **2016,** 49, 286−293.

[79] Hwang, B.; Gu, C.; Lee, D.; Lee, J. -S. Effect of halide-mixing on the switching behaviors of organic-inorganic hybrid perovskite memory. *Sci Rep.* **2017,** 7, 43794.

[80] Sun, Y.; Tai, M.; Song, C.; Wang, Z.; Yin, J.; Li, F.; Wu, H.; Zeng, F.; Lin, H.; Pan, F. Competition between metallic and vacancy defect conductive filaments in a $CH_3NH_3PbI_3$-based memory device. *J. Phys. Chem. C,* **2018,** 122, 6431−6436.

[81] Gu, C.; Lee, J. -S. Flexible hybrid organic-inorganic perovskite memory, *ACS Nano* **2016,** 10, 5413−5418.

[82] Yoo, E.; Lyu, M.; Yun, J. -H.; Kang, C.; Choi, Y.; Wang, L. Bifunctional resistive switching behavior in an organolead halide perovskite based $Ag/CH_3NH_3PbI_{3-x}Cl_x/FTO$ structure. *J. Mater. Chem. C* **2016,** 4, 7824.

[83] Kato, Y.; Ono, L, K.; Lee, M. V.; Wang, S.; Raga, S. R.; Qi, Y., Silver iodide formation in methyl ammonium lead iodide perovskite solar cells with silver top electrode. *Adv. Mater. Interfaces* **2015,** 2, 1500195.

[84] Kim, H. -S.; Jang, I. -H.; Ahn, N.; Choi, M.; Guerrero, A.; Bisquert, J.; Park, N. -G., Control of I-V hysteresis in $CH_3NH_3PbI_3$ perovskite solar cell. *J. Phys. Chem. Lett.* **2015,** 6, 4633−4639.

[85] Wojciechowski, K.; Stranks, S. D.; Abate, A.; Sadoughi, G.; Sadhanala, A.; Kopidakis, N.; Rumbles, G.; Li, C. -Z.; Friend, R. H.; Jen, A. K. -Y.; Snaith, H. J., Heterojunction modification for highly efficient organic-inorganic perovskite solar cells. *ACS Nano* **2014,** 8, 12701-12709.

[86] Cho, A. -N.; Jang, I. -H.; Seo, J. -Y.; Park, N. -G., Dependence of hysteresis on the perovskite film thickness: inverse behavior between TiO_2 and PCBM in a normal planar structure. *J. Mater. Chem. A* **2018,** 6, 18206.

[87] Thamaphat, K.; Limsuwan, P.; Ngotawornchai, B., Phase characterization of TiO_2 powder by XRD and TEM. *Nat. Sci.* **2008,** 42, 357 – 361.

[88] Zardetto, V.; Giacomo, F.D.; Lifka, H.; Verheijen, M.A.; Weijtens, C.H.L.; Black, L.E.; Veenstra, S.; Kessels, W.M.M.; Andriessen, R.; Creatore, M., Surface fluorination of ALD TiO_2 electron transport layer for efficient planar perovskite solar cells. *Adv. Mater. Interfaces* **2018,** 5, 1701456.

[89] Kim, T.W.; Uchida, S.; Kondo, T.; Segawa, H., Optimization of TiO_2 compact layer formed by atomic layer deposition for efficient perovskite solar cells. *Appl. Phys. Lett.* **2019,** 115, 203902.

[90] Kim, I.S.; Haasch, R.T.; Cao, D.H.; Farha, O.K.; Hupp, J.T.; Kanatzidis, M.G.; Martinson, A.B.F., Amorphous TiO_2 compact layers via ALD for planar halide perovskite photovoltaics. *ACS Appl. Mater. Interfaces* **2016,** 8, 24310−24314.

[91] J. J. Yang, D. B. Strukov and D. R. Stewart, Memristive devices for computing. *Nat. Nanotechnol.* **2013,** 8, 13.

[92] Lin, G.; Lin, Y.; Cui, R.; Huang, H.; Guo, X.; Li, C.; Dong. J.; Guo, X.; Sun, B., An organic-inorganic hybrid perovskite logic gate for better computing. *J. Mater. Chem. C* **2015,** 3, 10793.

[93] Choi, J.; Park, S.; Lee, J.; Hong, K.; Kim, D. -H.; Moon, C. W.; Park, G. D.; Suh, J.; Hwang, J.; Kim, S. Y.; Jung, H. S.; Park, N. -G.; Han, S.; Nam, K. T.; Jang, H. W., Organolead halide perovskites for low operating voltage multilevel resistive switching. *Adv. Mater.* **2016,** 28, 6562–6567.

[94] Guan, X.; Hu, W.; Haque, M. A.; Wei, N.; Liu, Z.; Chen, A.; Wu, T., Light-responsive ion-redistribution-induced resistive switching in hybrid perovskite Schottky junctions. *Adv. Funct. Mater.* **2018,** 28, 1704665

[95] Zhang, F.; Ma, W.; Guo, H.; Zhao, Y.; Shan, X.; Jin, K.; Tian, H.; Zhao, Q.; Yu, D.; Lu, X.; Lu, G.; Meng, S., Interfacial oxygen vacancies as a potential cause of hysteresis in perovskite solar cells. *Chem. Mater.* **2016,** 28, 802−812.

[96] Sun, Y.; Fang, X.; Ma, Z.; Xu, L.; Lu, Y.; Yu, Q.; Yuan, N.; Ding, J. Enhanced UV-light stability of organometal halide perovskite solar cells with interface modification and a UV absorption layer. *J. Mater. Chem. C* **2017,** 5, 8682—8687.

[97] Christians, J. A.; Herrera, P. A. M.; Kamat, P. V. Transformation of the excited state and photovoltaic efficiency of $CH_3NH_3PbI_3$ perovskite upon controlled exposure to humidified air. *J. Am. Chem. Soc.* **2015,** 137, 1530–1538.

[98] Meng, L.; You, J.; Yang, Y. Addressing the stability issue of perovskite solar cells for commercial applications. *NATURE COMMUNICATIONS* **2018,** 9, 5265.

[99] Yang, J.; Chen, S.; Xu, J., Zhang, Q.; Liu, H.; Liu, Z.; Yuan, M., A review on improving the quality of perovskite films in perovskite solar cells via the weak forces induced by additives. *Appl. Sci.* **2019,** 9, 4393.

[100] Sun, Y.; Wu, Y.; Fang, X.; Xu, L.; Ma, Z.; Lu, Y.; Zhang, W. -H.; Yu, Q.; Yuan, N.; Ding, J., Long-term stability of organic-inorganic hybrid perovskite solar cells with high efficiency under high humidity conditions. *J. Mater. Chem. A* **2017,** 5, 1374-1379.

[101] Tai, Q.; You, P.; Sang, H.; Liu, Z.; Hu, C.; Chan, H. L. W.; Yan, F., Efficient and stable perovskite solar cells prepared in ambient air irrespective of the humidity. *Nature Communications* **2016,** 7, 11105.

[102] Quan, L. N.; Yuan, M.; Comin, R.; Voznyy, O.; Beauregard, E. M.; Hoogland, S.; Buin, A.; Kirmani, A. R.; Zhao, K.; Amassian, A.; Kim, D. H.; Sargent, E. H., Ligand-stabilized reduced-dimensionality perovskites. *J. Am. Chem. Soc.* **2016,** 138, 8, 2649–2655.

[103] Saliba, M.; Matsui, T.; Domanski, K.; Seo, J. -Y.; Ummadisingu, A.; Zakeeruddin, S. M.; Correa-Baena, J. -P.; Tress, W. R.; Abate, A.; Hagfeldt, A.; Gratzel, M., Incorporation of rubidium cations into perovskite solar cells improves photovoltaic performance. *Science* **2016,** 354, 206-209.

[104] Kempe, M. D.; Dameron, A. A.; Reese, M. O., Evaluation of moisture ingress from the perimeter of photovoltaic modules. *Prog. Photovolt: Res. Appl.* **2014,** 22, 1159–1171.

[105] Fu, Q.; Tang, X.; Huang, B.; Hu, T.; Tan, L.; Chen, L.; Chen, Y., Recent progress on the long-term stability of perovskite solar cells. *Adv. Sci.* **2018,** 5, 1700387.

[106] Shi, L.; Bucknall, M. P.; Young, T. L.; Zhang, M.; Hu, L.; Bing, J.; Lee, D. S.; Kim, J.; Wu, T.; Takamure. N.; Mckenzie, D. R.; Huang, S.; Green M. A.; Ho-Baillie, A. W. Y., Gas chromatography-mass spectrometry analyses of encapsulated stable perovskite solar cells. *Science* **2020,** 368, 1309.

[107] Kim, S. J.; Choi, B.; Kim K. S.; Bae, W. J.; Hong, S. H.; Lee, J. Y.; Hwang, T. -K.; Kim, S. W., The potential role of polymethyl methacrylate as a new packing material for the implantable medical device in the bladder. *Biomed Res. Int.* **2015,** 852456, 8.

[108] Yu, D.; Yang, Y. -Q., Chen, Z.; Tao, Y. Liu, Y. -F., Recent progress on thin-film encapsulation technologies for organic electronic devices. *Opt. Commun.* **2016,** 362, 43-49.

[109] Hwang, I.; Jeong, I.; Lee, J.; Ko, M. J.; Y, K., Enhancing stability of perovskite solar cells to moisture by hydrophobic passivation. *ACS Appl. Mater. Interfaces* **2015,** 7, 17330−17336.

[110] Athawale, V. D.; Kolekar, S. L.; Raut, S. S. Recent developments in polyurethanes and poly(acrylates) interpenetrating polymer networks. *J. Macromol. Sci.* **2003,** 43, 1–26.

[111] Gupta, N.; Srivastava, A. K. Interpenetrating polymer networks: A review on synthesis and properties. *Polym. Int.* **1994,** 35, 109–118.

[112] Tian, Y.; Jiang, L., Intrinsically robust hydrophobicity. *Nature Materials* **2013,** 12, 291–292.

[113] Khan, S., Hydrophobicity of rare-earth oxide ceramics and their application in promoting sustained dropwise condensation and corrosion and fouling mitigation in hydropower systems. Ph.D. Dissertation, Massachusetts Institute of Technology, 2015.

[114] Vakili, E.; Semsarzadeh, M. A.; Ghalei, B.; Khoshbin, M.; Nasiri, H., Characterization and Gas Permeation Properties of Synthesized Polyurethane-Polydimethylsiloxane / Polyamide 12-b-Polytetramethylene Glycol Blend Membranes. *Silicon*, **2016**, 8, 75–88.

[115] Tsai, M. -H.; Huang. S. -L.; Chang, P. -H.; Chen, C. -J. Properties and Pervaporation Separation of Hydroxyl-Terminated Polybutadiene-Based Polyurethane/Poly(methyl methacrylate) Interpenetrating Networks Membranes. *Journal of Applied Polymer Science* **2007,** 4277-4286.

[116] Zhu, A. P.; Shi, Z. H.; Cai, A. Y.; Zhao, F.; Liao, T. Q. Synthesis of core–shell PMMA–SiO_2 nanoparticles with suspension–dispersion–polymerization in an aqueous system and its effect on mechanical properties of PVC. *composite. Polym. Test.* **2008,** 27, 540–547.

[117] Scully, J. R., Electrochemical impedance of organic-coated steel: correlation of impedance parameters with long-term coating deterioration. *J. Electrochem. Soc.* **1989,** 136, 979–990.

[118] Leijtens, T.; Eperon, G. E.; Pathak, S.; Abate, A.; Lee, M. M.; Snaith, H. J. Overcoming ultraviolet light instability of sensitized TiO_2 with meso-superstructured organometal tri-halide perovskite solar cell. *Nature Communications* **2013**, 4, 2885.

[119] Ito, S.; Tanaka, S.; Manabe, K.; Nishino, H. Effects of surface blocking layer of Sb_2S_3 on nanocrystalline TiO_2 for $CH_3NH_3PbI_3$ perovskite solar cells. *J. Phys. Chem. C* **2014**, 118, 16995–17000.

[120] Ju, M.; Balaji, N.; Park, C.; Thanh Nguyer, H. T.; Cui, J.; Oh, D.; Jeon, M.; Kang, J.; Shim, G.; Yi, J., The effect of small pyramid texturing on the enhanced passivation and efficiency of single c-Si solar cells. *RSC Adv.* **2016,** 6, 49831–49838.

[121] Han, G. H.; Lee, S.; Duff, M. L.; Qin, F.; Jiang, M.; Li, G; Lee, J. -K. Multi-functional transparent electrode for reliable flexible perovskite solar cell. *Journal of Power Sources* **2019,** 435, 226768